Université de Neuchâtel
Institut de Microtechnique

Applied Statistical Optics: White-Light Interferometry and Detection of Moving Speckles

Thèse

Présentée à la Faculté des sciences
pour obtenir le grade de docteur ès sciences

par

Urban Schnell

Neuchâtel, Septembre 1997

IMPRIMATUR POUR LA THÈSE

Applied statistical optics: white-light interferometry and detection of moving speckles

de M. Urban Schnell

UNIVERSITÉ DE NEUCHÂTEL

FACULTÉ DES SCIENCES

La Faculté des sciences de l'Université de Neuchâtel sur le rapport des membres du jury,

MM. R. Dändliker (directeur de thèse), F. Pellandini, J. Piot (Logitech SA, Morges), J.C. Dainty (Imperial College, Londres) et J.W. Goodman (Stanford Université USA)

autorise l'impression de la présente thèse.

Neuchâtel, le 22 janvier 1998

Le doyen:

F. Stoeckli

F. Stoeckli

Contents

1 Introduction

Statistical optics is the study of the random properties of optical phenomena. Statistical models are invoked when the physical quantities are not completely specified in advance and cannot be predicted with perfect precision by a deterministic model. Randomness in optical phenomena arises because of (i) unpredictable fluctuations of the light or of the medium through which the light propagates, (ii) scattering of light from rough surfaces, diffused glass or turbulent media, like fluids and gas, which imparts random variations to the optical wave, and (iii) noise in the process of photon detection, which imparts random fluctuations to the detected energy.

The random fluctuations of light waves are characterized by the degree of coherence. Light may be classified as (i) incoherent, (ii) coherent, or, in general, (iii) partially coherent. Incoherent light is random because it is a superposition of emissions from many atoms radiating independently and at different optical frequencies and phases. Examples of incoherent light sources are low-pressure gas discharge lamps, such as neon tubes, and thermal light sources, as light bulbs or the sun. Coherent light is characterized by photons that are all identical and indistinguishable. Thus coherent optical waves have a single optical frequency – high spectral purity – and a perfectly predictable and deterministic phase function. Lasers †, such as solid-state, gas or dye lasers, are examples of coherent light sources.

Modern optics uses coherent light mainly (i) as carrier of information, (ii) when high spectral purity is of interest, or (iii) when high radiance is required. In technical applications, modern optics has experienced deep changes over the last years. For many years, coherent optics has been reserved for laboratory research applications and for industrial high-end products, such as high resolution metrology methods, medical instrumentation, laser manufacturing or optical inspection methods. The limitation was mainly due to the cost and the size of the coherent light sources. Recent progress in semiconductor science and batch technology for microelectronics manufacturing allowed coherent optics to penetrate the low cost, customer product market. Namely cheap, reliable and easy-to-use light sources, such as light emitting diodes (*LED*) or laser diodes (*LD*), and application specific photodetection systems, photodiode arrays (*PDA*) and charge coupled devices (*CCD*), became available for the design and the realization of low cost optical systems. Examples are computer peripheries (optical storage drives, laser printers, pointing devices), compact disc (*CD*) units for audio and video application, *CCD* cameras and digital photography, auto focus systems for photography, laser pointers, infrared (*IR*) remote control systems, optical telecommunications, etc.

† *L*ight *A*mplification by *S*timulated *E*mission of *R*adiation

The work presented here discusses randomness in optical phenomena. The results are used for the design and the experimental investigation of two different types of optical systems. The statistical aspects of these systems are emphasized.

Chapter 2 provides a review of the mathematical concepts to describe statistical optics and presents the specific results that will be used in later chapters. Chapter 3 deals with white-light interferometry. The progress in photodetector array technology over the last years gave rise to a revival of broad band light sources for interferometry in technical applications. Our contribution to this development is a dispersive white-light interferometer for absolute distance measurement in the sub-millimeter range. Spectral analysis of the interferogram allows to compensate the measurement for wavelength sensitive dispersive targets. The validity of the method is experimentally demonstrated. Applications of the interferometer are (i) autofocusing systems, (ii) non-contact profilometry, and (iii) non-destructive thin film characterization systems. Chapter 4 is concerned with scattering of coherent light from rough surfaces. The result is a random spatial distribution of the light intensity, known as laser speckle. Contrary to well known techniques for measuring displacement or velocity of constantly moving objects, the detection of movement at arbitrary low speed, including change of direction, requires a completely different approach of opto-electronic detection and signal processing. We have theoretically and experimentally investigated a laser speckle based technique for non-contact detection of in-plane movement of rough objects which satisfies these requirements. Its application in an optical computer mouse working on arbitrary desk surfaces is discussed. The noise properties of the photodetection system are analyzed. Finally, Chapter 5 compares coherence and speckle theory from the physical and the statistical point of view and concludes with some general considerations about modern optics in technical applications.

2 Statistical Methods in Optics

The statistical aspects of optical systems play a central role in this work. Thus the mathematical methods used to analyze statistical phenomena are first discussed in this chapter. Specific results and the statistical tools which are used in the following are presented. Section 1 summarizes the concept of probability and random variables. Section 2 extends the notion of random variables to the more general concept of random processes. Section 3 finally is concerned with statistics and points out the difference between statistics and probability.

2.1 Probability and Random Variables

Probability theory is a mathematical treatment of the intuitive notion of hazard. It is a rigorous study of phenomena where no deterministic mathematical model can be applied. Experiments with outcomes that cannot be predicted in advance are referred to as random experiments. The collection of all possible outcomes of a random experiment is the set of events {A}.

2.1.1 Random Variables

When a real number u(A) is assigned to every possible event A of a random experiment, a random variable U then consists of both the set of all possible values u(A) together with their associated probabilities. A random variable U is called discrete if the experimental outcomes consist of a set of discrete numbers $\{u_1, u_2, ..., u_n, ...\}$. Any u_n is characterized by the event $U = u_n$ and its probability $p_n = P(U = u_n)$. Thus a discrete random variable U is defined by the mathematical application, known as the probability mass function (*PMF*) or the distribution, which assigns the probability p_n to each number u_n. A random variable U is called continuos if the experimental outcomes can lie anywhere on a continuum of possible values. The probability that the random variable takes a value within the interval [a, b] is calculated through

$$P(a \le U \le b) = \int_a^b du\ pdf_U(u), \qquad (a > -\infty, b < \infty) \tag{2.1}$$

where $pdf_U(u)$ is the probability density function (*PDF*) or the distribution of the random variable. This function entirely describes the probabilistic behaviour of the random variable and satisfies

$$pdf_U(u) \ge 0 \tag{2.2a}$$

$$\int_{-\infty}^{\infty} du\ pdf_U(u) = 1. \tag{2.2b}$$

The distribution of some frequently used random variables are given in § 2.5.

2.1.2 System of random variables

Consider two random experiments with sets of events {A} and {B}, respectively. A numerical value u(A) is assigned to each outcome A of the first experiment and v(B) to each outcome B of the second experiment. The joint random variable UV is defined to be the collection of all possible joint numbers (u,v) together with an associated measure of probability. According to the case of one random variable, the probabilistic behaviour of the joint random variable UV is characterized by the joint probability density function (*jPDF*) $\mathrm{pdf}_{UV}(u,v)$, which satisfies the two-dimensional form of Eq. (2.2). The marginal *PDF* of the random variable U is found from the *jPDF* of the joint random variable UV through

$$\mathrm{pdf}_U(u) = \int_{-\infty}^{\infty} dv\ \mathrm{pdf}_{UV}(u,v). \tag{2.3}$$

The marginal *PDF* of the random variable V is found by interchanging the variables u and v in Eq. (2.3). If the random variables U and V are statistically independent, that is, the probabilistic behaviour of one random variable is not influenced by the other, their *jPDF* is simply given by

$$\mathrm{pdf}_{UV}(u,v) = \mathrm{pdf}_U(u)\ \mathrm{pdf}_V(v). \tag{2.4}$$

2.1.3 Statistical Averages

The probabilistic behaviour of a random variable can be partially characterized and summarized by some numerical values. Let g(u) be a function that for every value u of a random variable U assigns a new real value g(u). The statistical average of g(u) is then defined by

$$E(g(u)) = \int_{-\infty}^{\infty} du\ g(u)\mathrm{pdf}_U(u). \tag{2.5}$$

The simplest statistical average properties of a random variable are its moments, which are obtained from Eq. (2.5) by setting $g(u) = u^k$ to obtain the *k*th moment. Of particular importance are the first moment (for k = 1), known as the mean or the expectation,

$$E(U) = \int_{-\infty}^{\infty} du\ u\ \mathrm{pdf}_U(u), \tag{2.6}$$

and the second moment (for k = 2)

$$E(U^2) = \int_{-\infty}^{\infty} du\ u^2\ \mathrm{pdf}_U(u). \tag{2.7}$$

Often, the fluctuations of a random variable about its expectation are of interest, in which case the central moments, obtained from Eq. (2.5) by setting $g(u) = (u-E(U))^k$ to obtain the kth central moment, play the key role. Of particular importance is the second central moment

$$\sigma_U^2 = \int_{-\infty}^{\infty} du\ (u - E(U))^2\ pdf_U(u), \tag{2.8}$$

known as the variance of the random variable. For practical evaluation of the variance, it can easily be shown that

$$\sigma_U^2 = E\left(U^2\right) - E^2(U). \tag{2.9}$$

The square root σ_U of the variance, known as the standard deviation, is a measure of the dispersion or spread of values assumed by the random variable.

2.1.3.1 Joint moments of random variables

Let U and V be jointly distributed random variables. The joint moments of U and V are then

$$E\left(U^n V^m\right) = \int_{-\infty}^{\infty}\int_{-\infty}^{\infty} du dv\ u^n v^m\ pdf_{UV}(u,v). \tag{2.10}$$

Of practical importance are the correlation between U and V (for $n = m = 1$)

$$C_{UV} = E(UV) = \int_{-\infty}^{\infty}\int_{-\infty}^{\infty} du dv\ uv\ pdf_{UV}(u,v), \tag{2.11}$$

the covariance of U and V

$$Cov_{UV} = E\left([u - E(U)]\cdot[v - E(V)]\right) = C_{UV} - E(U)E(V), \tag{2.12}$$

and the correlation coefficient

$$\mu = \frac{Cov_{UV}}{\sigma_U \sigma_V}. \tag{2.13}$$

The correlation coefficient μ is a direct measure for the similarity of the fluctuations of U and V. If $\mu = 1$, U and V are perfectly correlated and their fluctuations are essentially identical. When $\mu = 0$, U and V are uncorrelated. Two statistically independent random variables are always uncorrelated. The inverse is not true; i.e., lack of correlation does not necessarily imply statistical independence.

2.1.4 Transformation of Random Vnriables

It is of interest to determine the *PDFs* of random variables after they have been subjected to a linear – or non-linear – transformation. Consider two jointly distributed random variables W and Z that are functionally related to two jointly distributed random variables U and V by

$$\begin{aligned} w &= f(u,v) \\ z &= g(u,v) \,. \end{aligned} \tag{2.14}$$

The problem is to find the *jPDF* of WZ, assumed that the *jPDF* of UV is known. Only single valued, one-to-one transformations f(u,v) and g(u,v) in Eq. (2.14) are considered, for which the inverse transformations exist. Then u and v are expressed in terms of w and z by

$$\begin{aligned} u &= F(w,z) \\ v &= G(w,z) \,. \end{aligned} \tag{2.15}$$

The probability that the values u and v lie in an incremental area $\Delta u \Delta v$ equals the probability that w and z lie in the elementary area $\Delta w \Delta z$. Thus for small $\Delta u \Delta v$ and $\Delta w \Delta z$

$$\mathrm{pdf}_{WZ}(w,z)\Delta w \Delta z = \mathrm{pdf}_{UV}(u,v)\Delta u \Delta v \tag{2.16}$$

and

$$\Delta u \Delta v = |J|\, \Delta w \Delta z, \tag{2.17}$$

where |J| is the Jacobian of the inverse transformation, calculated from Eq. (2.15) through

$$|J| = \begin{vmatrix} \dfrac{\partial F}{\partial w} & \dfrac{\partial F}{\partial z} \\ \dfrac{\partial G}{\partial w} & \dfrac{\partial G}{\partial z} \end{vmatrix} , \tag{2.18}$$

where |·| stands for the modulus of the determinant. Substituting Eqs. (2.15) and (2.17) in Eq. (2.16) finally yields

$$\mathrm{pdf}_{WZ}(w,z) = |J|\, \mathrm{pdf}_{UV}(u,v) \,. \qquad u = F(w,z)\ ;\ v = G(w,z) \tag{2.19}$$

2.1.5 Sums of Random Variables, Central Limit Theorem

A basic theorem of enormous importance is the central limit theorem. Consider N independent random variables $U_1, U_2, \ldots, U_N$ with arbitrary *PDF*, expectation $E(U_n)$ and variance $\sigma_n^2 > 0$ ($n = 1, 2, \ldots, N$). Let a new random variable U be defined by the sum

$$U = \frac{1}{\sqrt{N}} \sum_{n=1}^{N} U_n \,. \tag{2.20}$$

Then, under certain conditions that are often met in practice, as the number N of random variables tends to infinity, it can be shown [1–3] that the *PDF* of the random variable U approaches Gaussian distribution

$$\lim_{N\to\infty} \mathrm{pdf}_U(u) = \frac{1}{\sqrt{2\pi}\sigma} \exp\left\{ - \frac{(u - E(U))^2}{2\sigma^2} \right\} , \tag{2.21}$$

with expectation E(U) and variance σ^2 given by

$$E(U) = \frac{1}{\sqrt{N}} \sum_{n=1}^{N} E(U_n) \,,$$

$$\sigma^2 = \frac{1}{N} \sum_{n=1}^{N} \sigma_n^2 \,. \tag{2.22}$$

A plot of the Gaussian distribution in Eq. (2.21) is shown in Fig. 2.1.

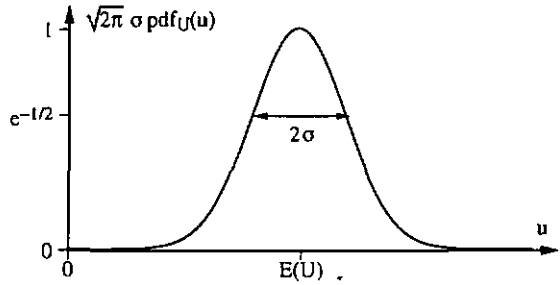

Fig. 2.1 Gaussian probability density function.

2.1.6 Gaussian Random Variables

Many random phenomena in physics result from addition of a large number of independent random events. By virtue of the central limit theorem, Gaussian random variables accordingly play a role of unsurpassed importance in the probabilistic analysis of physical phenomena. Of most importance in the following are two uncorrelated ($\mu = 0$), jointly distributed Gaussian random variables U and V, each having zero expectation E(U) = E(V) = 0 and equal variance σ^2. In this case, their *jPDF* is

$$\mathrm{pdf}_{UV}(u,v) = \frac{1}{2\pi\sigma^2}\exp\left\{-\frac{u^2+v^2}{2\sigma^2}\right\}$$

$$= \frac{1}{\sqrt{2\pi}\sigma}\exp\left\{-\frac{u^2}{2\sigma^2}\right\}\cdot\frac{1}{\sqrt{2\pi}\sigma}\exp\left\{-\frac{v^2}{2\sigma^2}\right\} = \mathrm{pdf}_U(u)\,\mathrm{pdf}_V(v)\,. \qquad (2.23)$$

Equation (2.23) shows that the *jPDF* factors into the product of two marginal *PDFs*. Thus two uncorrelated Gaussian random variables are also statistically independent (§ 2.1.2).

2.1.7 Complex-Valued Random Variables

In the previous sections, the properties of random variables that take on real values have been described. Frequently in the study of optical waves, it is necessary to consider random variables that take on complex values. Underlying the definition of every random variable, there is a set of events {A} and a set of associated probabilities. If a complex number u(A) is assigned to each event A, the set of all possible complex numbers together with their associated probabilities define a complex-valued random variable **U**. To describe the statistical properties of the random variable **U**, it is most convenient to define the joint statistical properties of its real and imaginary parts. Thus if U = R + j·I represents a complex random variable that can take on specific values u = r + j·i, a complete description of U entails specification of the *jPDF* of R and I. Of special interest are jointly circular complex Gaussian random variables, with *jPDF* described by Eq. (2.23). Contours of constant probability are circles in the (r,i) plane explaining the denomination of circular complex Gaussian. According to Eq. (2.23), the real and imaginary parts of circular complex Gaussian random variables are uncorrelated and therefore independent.

2.1.8 Random Phasor Sums

In optics, the most frequent case of complex numbers are phasors, representing amplitude and phase of monochromatic waves. Sums of complex-valued random variables are referred to as random phasor sums. Consider the sum of N complex phasors $\mathbf{u}_n$, the *n*th phasor having random amplitude $u_n / \sqrt{N}$ and phase ϕ_n (n = 1, 2, ..., N), as sketched in Fig. 2.2.

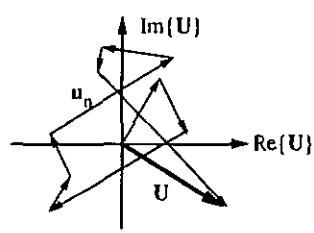

Fig. 2.2 Random phasor sum in the complex plane.

The resultant phasor **U**, with amplitude U and phase ϕ, can be written as

$$\mathbf{U} = U\exp\{j\phi\} = \frac{1}{\sqrt{N}} \sum_{n=1}^{N} u_n e^{j\phi_n} . \qquad U \geq 0 \tag{2.24}$$

For the sake of simplicity of the statistical analysis, the following assumptions, which are generally satisfied in practical problems, about the elementary phasors $\mathbf{u}_n$ are made:

(i) The amplitude $u_n / \sqrt{N}$ and the phase ϕ_n of the nth elementary phasor are statistically independent of each other and of the other N-1 phasors.

(ii) The phases ϕ_n are uniformly distributed in the interval $[-\pi, \pi]$ (§ 2.5).

The real (r) and imaginary (i) parts of the resultant phasor $\mathbf{U} = r + j\cdot i$ are given by

$$r = \mathrm{Re}\left[U\exp\{j\phi\}\right] = \frac{1}{\sqrt{N}} \sum_{n=1}^{N} u_n \cos\phi_n , \tag{2.25a}$$

$$i = \mathrm{Im}\left[U\exp\{j\phi\}\right] = \frac{1}{\sqrt{N}} \sum_{n=1}^{N} u_n \sin\phi_n . \tag{2.25b}$$

By virtue of the central limit theorem, both r and i are approximately Gaussian random variables for large N. To specify their *jPDF*, the quantities E(r), E(i), σ_r^2, σ_i^2, and the correlation coefficient μ must be calculated. It can readily be shown [1] that $E(r) = E(i) = 0$, $\sigma_r^2 = \sigma_i^2 = \sigma^2 = E(U^2)/2$, and $\mu = 0$. Then, at the limit of very large N, the *jPDF* of the real and imaginary parts of the random phasor sum U obeys circular complex Gaussian distribution

$$\mathrm{pdf}(r,i) = \frac{1}{2\pi\sigma^2} \exp\left\{-\frac{r^2 + i^2}{2\sigma^2}\right\} . \tag{2.26}$$

2.1.8.1 Statistics of the Amplitude and the Phase

In many applications, the amplitude U and the phase ϕ of the random phasor sum **U** have more physical appeal than the real (r) and imaginary (i) parts. The change from rectangular (r,i) to polar (U,ϕ) coordinates is a single valued, one-to-one transformation and the results in § 2.1.4 can be used to find the *jPDF* of U and ϕ. The inverse functions of the transformation are $r = U\cos\phi$ and $i = U\sin\phi$, which gives for the Jacobian in Eq. (2.18) $|J| = U$. From Eqs. (2.19) and (2.26) one obtains for the *jPDF* of the amplitude U and the phase ϕ

$$\mathrm{pdf}(U,\phi) = \begin{cases} \dfrac{U}{2\pi\sigma^2} \exp\left\{-\dfrac{U^2}{2\sigma^2}\right\} & U \geq 0,\ -\pi < \phi \leq \pi \\ 0 & \text{otherwise} \end{cases} . \tag{2.27}$$

The marginal *PDF* of U is found by integrating Eq. (2.27) over the phase ϕ. The result is

$$\mathrm{pdf}(U) = \begin{cases} \dfrac{U}{\sigma^2} \exp\left\{-\dfrac{U^2}{2\sigma^2}\right\} & U \geq 0 \\ 0 & \text{otherwise} \end{cases} , \tag{2.28}$$

which is known as the Rayleigh distribution. A plot of this function is shown in Fig. 2.3. Expectation E(U) and variance σ_U^2 are related to the parameter σ^2 in Eq. (2.28) through

$$E(U) = \sqrt{\frac{\pi}{2}}\,\sigma,$$

$$\sigma_U^2 = \left(2 - \frac{\pi}{2}\right)\sigma^2 . \tag{2.29}$$

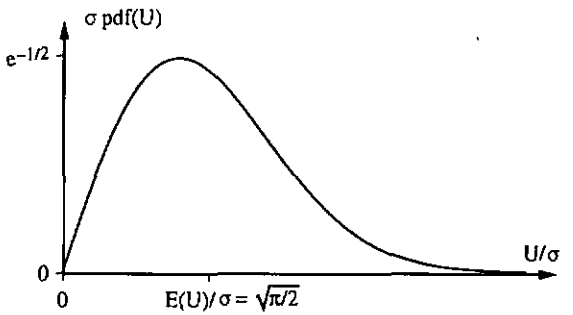

Fig. 2.3 Rayleigh probability density function of the amplitude U.

The marginal *PDF* of the phase ϕ is found by integrating Eq. (2.27) over the amplitude U. It follows that the phase ϕ obeys the uniform distribution in the interval $[-\pi, \pi]$ (§ 2.5). Note that the *jPDF* in Eq. (2.27) is the product of the marginal *PDFs* of U and ϕ. Thus the amplitude U and phase ϕ of the random phasor sum are statistically independent (§ 2.1.2).

2.2 Random Processes

The notion of random processes is a generalization of the concept of random variables, for which the random events are functions rather than numbers. In general, random processes are functions of time or space. Underlying the concept of a random process is still a random experiment, with a set of events {A} and an associated measure of probability. A random process U(t,A) assigns to each elementary event A the real valued function u(t,A) [or u(x,A)] with independent time variable t [or space variable x] (for the sake of simplicity, the following results are expressed in terms of the time variable t, keeping in mind that the space versions are self-evident). U(t,A) has the following interpretations: it is [2]

(i) a family (or an ensemble) of functions U(t,A). In this interpretation, t and A are variable.
(ii) a single time function U(t) (or a sample of the given process). In this interpretation, t is variable and A is fixed.
(iii) a random variable U(A) equal to the state of the process at time t. In this interpretation, t is fixed and A is variable.
(iv) a number U, if t and A are fixed.

The most general description of a random process is a complete enumeration of all sample functions composing the random process, together with a specification of their probabilities. This complete description is seldom possible nor desirable. The most useful description consists of the first-order *PDF* $\mathrm{pdf}_U(u;t)$, which is calculated for a fixed time t, and the second-order *PDF* $\mathrm{pdf}_U(u_1,u_2;t_1,t_2)$, which is calculated at time t_1 and t_2. The notation U(t) will be used to represent a random process omitting its dependence on A.

2.2.1 Stationarity and Ergodicity

A random process is called strict-sense stationary if its probabilistic properties are invariant to a shift of the time origin, meaning that the processes U(t) and $U(t+\tau)$ have the same statistical properties for any τ. In particular, the first-order *PDF* of a strict-sense stationary random process U(t) is independent of t and hence can be written as $\mathrm{pdf}_U(u)$. Similarly, the second-order *PDF* depends only on the time delay $\tau = t_2 - t_1$ and can be written as $\mathrm{pdf}_U(u_1,u_2;\tau)$. A random process is called wide-sense stationary if it satisfies the more restrictive conditions

$$E(u(t)) = E(u) \tag{2.30}$$

and

$$E(u(t_1)u(t_2)) = E\big(u(t+\tau)u(t)\big)\,. \tag{2.31}$$

The most severe restriction on random processes is ergodicity. A random process is ergodic if any time and ensemble averages are equal and interchangeable. Thus if g(u) is the quantity to be averaged, the time average

$$E(g) = \lim_{T\to\infty} \frac{1}{T} \int_{-T/2}^{T/2} dt\, g(u(t)) \tag{2.32}$$

equals the ensemble average

$$E(g) = \int_{-\infty}^{\infty} du\, g(u)\, \mathrm{pdf}_U(u)\,. \tag{2.33}$$

Only ergodic random processes which satisfy the conditions in Eqs. (2.30) to (2.33) are considered in the following.

2.2.2 Spectral Analysis of Random Processes [1]

There are two different classes of time functions u(t). If u(t) has the property

$$\int_{-\infty}^{\infty} dt\, |u|^2 < \infty, \tag{2.34}$$

it is Fourier transformable and the Fourier transform

$$\hat{u}(v) = \int_{-\infty}^{\infty} dt\, u(t)\, e^{-j2\pi vt} \tag{2.35}$$

always exists. If u(t) does not satisfy Eq. (2.34) but satisfies

$$\lim_{T\to\infty} \frac{1}{T} \int_{-T/2}^{T/2} dt\, u^2(t) < \infty\,, \tag{2.36}$$

it is said to have finite average power. In any case, the distribution of energy or power over frequency is of interest. Since the sample function u(t) of the random process U(t) is unknown in advance, the quantity to be concerned with is the expected distribution of energy or power, known as the energy (*ESD*) and power (*PSD*) spectral density, respectively. If u(t) is Fourier transformable [Eq. (2.34)], the *ESD* of the random process U(t) is defined by

$$\mathcal{E}_U(v) = E\left(|\hat{u}(v)|^2\right)\,. \tag{2.37}$$

If u(t) has finite average power, according to Eq. (2.34), the Fourier integral in Eq. (2.35) does not exist. However, the truncated function

$$u_T(t) = \begin{cases} u(t) & -\frac{T}{2} \le t \le \frac{T}{2} \\ 0 & \text{otherwise} \end{cases} \tag{2.38}$$

does have a Fourier transform $\hat{u}_T(v)$, and the *PSD* of u(t) is defined by

$$\mathcal{P}_U(v) = \lim_{T\to\infty} \frac{1}{T} E\left(|\hat{u}_T(v)|^2\right)\,. \tag{2.39}$$

Energy and power spectral densities are real, positive and even functions of v and satisfy

$$\int_{-\infty}^{\infty} dv\, \mathcal{E}_U(v) = \int_{-\infty}^{\infty} dt\, E\left(u^2(t)\right) \tag{2.40a}$$

$$\int_{-\infty}^{\infty} dv\, \mathcal{P}_U(v) = E\left(u^2\right)\,. \tag{2.40b}$$

2.2.3 Linearly Filtered Random Process [1]

Let the random process V(t) consist of sample functions which result from passing all sample functions of the random process U(t) through a linear filter with impulse response s(t) and transfer function $\hat{s}(\nu)$. Then V(t) is called a linearly filtered random process. The *ESD* (for a Fourier transformable random process U(t)) or the *PSD* (for a finite average power random process U(t)) of V(t) is then given by

$$\mathcal{G}_V(\nu) = |\hat{s}(\nu)|^2 \, \mathcal{G}_U(\nu) \tag{2.41a}$$

or

$$\mathcal{G}_V(\nu) = |\hat{s}(\nu)|^2 \, \mathcal{G}_U(\nu) \, , \tag{2.41b}$$

respectively. Thus the *ESD* (*PSD*) of the output random process V(t) is simply the squared modulus of the transfer function of the linear filter $|\hat{s}(\nu)|^2$ times the *ESD* (*PSD*) of the input random process.

2.2.4 Wiener-Khinchin Theorem and Autocorrelation Function

The autocorrelation function of an ergodic random process is

$$C_U(\tau) = E\big(u(t+\tau)u(t)\big)$$

$$= \lim_{T\to\infty} \frac{1}{T} \int_{-T/2}^{T/2} dt \; u(t+\tau)u(t) \, . \tag{2.42}$$

It is an even function of the time delay τ and satisfies $C_U(0) = E(u^2)$. A major practical importance of the autocorrelation function lies in its relationship to the power spectral density: for a random process that is at least wide-sense stationary, the autocorrelation function and the power spectral density form a Fourier transform pair, namely

$$\mathcal{G}_U(\nu) = \int_{-\infty}^{\infty} d\tau \; C_U(\tau) \, e^{-j2\pi\nu\tau}$$

$$C_U(\tau) = \int_{-\infty}^{\infty} d\nu \; \mathcal{G}_U(\nu) \, e^{j2\pi\nu\tau} \, . \tag{2.43}$$

This very special relationship is known as the Wiener-Khinchin theorem.

2.2.5 Analytic Signals, Envelope and Phase

It is common practice to represent a real-valued signal by a complex-valued signal, whose real part equals the original signal. Provided that only linear operations are performed on the complex signal, the original signal can be determined at any time by taking the real part of the complex signal. The main reason for preferring a complex representation is to simplify the algebra when the signal passes through linear systems. Consider a monochromatic, real-valued signal u(t) at frequency ν_0

$$u(t) = U\cos(2\pi\nu_0 t + \phi)\,, \tag{2.44}$$

where U and ϕ stand for the amplitude and phase, respectively. The complex representation of the signal is then

$$\mathbf{u}(t) = \mathbf{U}\exp\{j2\pi\nu_0 t\}\,, \tag{2.45}$$

where $\mathbf{U} = U\exp\{j\phi\}$ is the complex-valued phasor representing the amplitude and phase of u(t). The Fourier transform of u(t) in Eq. (2.44) is

$$\hat{u}(\nu) = \mathbf{U}\exp\{j\phi\nu/\nu_0\}\,\frac{1}{2}\left[\delta(\nu+\nu_0) + \delta(\nu-\nu_0)\right]\,, \tag{2.46}$$

as shown in Fig. 2.4a), whereas the Fourier transform of the complex-valued representation $\mathbf{u}(t)$ in Eq. (2.45) is

$$\hat{\mathbf{u}}(\nu) = \mathbf{U}\,\delta(\nu-\nu_0)\,, \tag{2.47}$$

as shown in Fig. 2.4b).

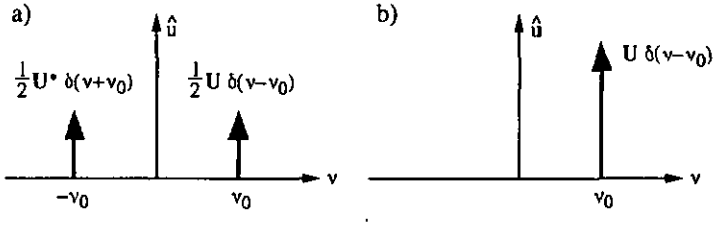

Fig. 2.4 Fourier transform of a) a monochromatic real-valued signal and b) the unilateral form of its complex representation.

Equation (2.47) is the unilateral form of Eq. (2.46) and satisfies

$$\hat{\mathbf{u}}(\nu) = 2\varepsilon(\nu)\,\hat{u}(\nu)\,, \qquad \nu \geq 0 \tag{2.48}$$

where $2\varepsilon(\nu) = 1 + \mathrm{sgn}(\nu)$. By analogy, any real-valued signal – deterministic or random – can be represented by a complex-valued signal whose real part equals the original signal.

2.2.5.1 Analytic Signal

An analytic signal u(t) is a complex function of time (or space) whose Fourier transform $\hat{u}(\nu)$ is the unilateral form $\hat{u}^+(\nu)$ of the Fourier transform $\hat{u}(\nu)$ of its real part u(t), namely

$$u(t) = u(t) + j\cdot\mathcal{H}(u(t)) \tag{2.49}$$

with

$$\hat{u}(\nu) = \hat{u}^+(\nu) = 2\varepsilon(\nu)\,\hat{u}(\nu)\,. \tag{2.50}$$

$\mathcal{H}(\cdot)$ in Eq. (2.49) stands for the Hilbert transform of $(\cdot)$, which is defined by

$$\mathcal{H}(u(t)) = \frac{1}{\pi t} \otimes u(t) = \frac{1}{\pi}\int_{-\infty}^{\infty} d\tau\, \frac{u(\tau)}{t-\tau}\,, \tag{2.51}$$

where $\otimes$ denotes the convolution integral indicating that the Hilbert transform is equivalent to a linear filter with impulse response $s(t) = (\pi t)^{-1}$ and transfer function $\hat{s}(\nu) = -j\cdot\mathrm{sgn}(\nu)$. The Hilbert transform is a pure $\pm\pi/2$ phase shifter $[|\hat{s}(\nu)| \equiv 1,\ \arg(\hat{s}(\nu)) = -\mathrm{sgn}(\nu)\cdot\pi/2]$ so that the Hilbert transform $\mathcal{H}(u(t))$ is the quadrature signal of u(t).

2.2.5.2 The Analytic Signal as a Complex-Valued Random Process

If u(t) is the sample function of a random process U(t), the analytic signal representation u(t) may be regarded as the sample function of a complex-valued random process U(t). Let $C_U(\tau)$ and $\mathcal{G}_U(\nu)$ represent the autocorrelation function and the *PSD* of the real-valued random process U(t). It can be shown [1] that the autocorrelation function and the *PSD* of the analytic signal representation are given by

$$C_U(\tau) = 2C_U(\tau) + j\cdot 2\mathcal{H}(C_U(\tau)) \tag{2.52}$$

and

$$\mathcal{G}_U(\nu) = \mathcal{G}^+_U(\nu) = \begin{cases} 4\mathcal{G}_U(\nu) & \nu > 0 \\ 0 & \nu < 0 \end{cases}\,, \tag{2.53}$$

respectively. Thus the autocorrelation function of an analytic signal has a unilateral Fourier transform and is itself an analytic signal.

Similarly, the cross-correlation function of two jointly analytic signals u(t) and v(t), defined by $C_{UV}(\tau) = E\big(u(t+\tau)v^*(t)\big)$, is given by

$$C_{UV}(\tau) = 2C_{UV}(\tau) + j\cdot 2\mathcal{H}(C_{UV}(\tau))\,, \tag{2.54}$$

where $C_{UV}(\tau)$ is the cross-correlation function of the real-valued random processes U(t) and V(t).

2.2.5.3 Envelope and Phase

The analytic signal in Eq. (2.49) can be written in polar coordinates by

$$\mathbf{u}(t) = r(t)\exp\{j\phi(t)\}, \tag{2.55}$$

where $r(t) = \sqrt{u^2 + (\mathcal{H}(u))^2}$ is the module and $\phi(t) = \tan^{-1}[\mathcal{H}(u)/u]$ is the argument of u(t) (the time dependence of u(t) has been omitted to simplify the notation). Thus a model of the instantaneous amplitude (or envelope) and phase of u(t) can be defined by the module r(t) and the argument $\phi(t)$ of the analytic signal $\mathbf{u}(t)$, respectively. As an example, a narrow-band ($\Delta\nu << \nu_0$) random signal u(t) and its calculated envelope r(t) are shown in Fig. 2.5.

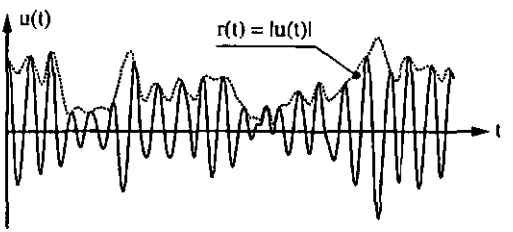

Fig. 2.5 Narrow-band random signal u(t) and the calculated envelope r(t).

2.3 Statistics

Probability theory is a mathematical description developed as an abstract model and its conclusions are deductions. All parameters of a probabilistic model are assumed to be fully defined and known. Thus probability problems have unique and precise solutions. In practical situations, this is rarely the case and statistical methods need to be invoked. Statistics suggests probabilistic models of physical systems and investigates their validity and quality by means of experimental tests. The goal is to gain insight into the behaviour of physical systems and to facilitate better predictions and decisions regarding these systems.

2.3.1 Statistical Methods

There are two fundamental classes of statistical methods [2,4]. Given a postulated probabilistic model of a physical system, which depends on some parameters, and a set of experimental data.

(i) Statistical estimation establishes the best values of the parameters of the probabilistic model using the set of experimental data.

(ii) Statistical testing qualifies a hypothesis on the parameters or on the probabilistic model itself using the set of experimental data. The result of the test is used either to accept or to reject the hypothesis.

Only statistical estimation is used in later chapters.

Suppose performance of an experiment N times and that the random variable U is the characteristic of interest of the possible outcomes. The random variable defined on the *n*th performance of the experiment is denoted by U_n. The set of random variables $\{U_1, U_2, ..., U_N\}$ is called a sample of size N of the random variable U whose probabilistic behaviour is specified by the probabilistic model. The word statistic is used to describe any function of some random variables $T = T(U_1, U_2, ...)$. The argument of the statistic may either be experimental values, which are obtained by the performance of (real) experiments with the physical system, or values obtained by the performance of (hypothetical) experiments with the postulated model. The statistic T is called estimator of the parameter P of the probabilistic model if the observed value of T estimates the value of P. A good estimator has the property to be unbiased, meaning that E(T) = P. The quality of an estimator T is also characterized by its variance σ_T^2; the smaller the variance the better the quality of the estimator.

2.3.2 Frequently used Statistics

2.3.2.1 Sample Mean

A fundamental statistic of the sample $\{U_1, U_2, ..., U_N\}$ is the sample mean $\bar{U}$, which is an estimator of the expectation E(U). It is usually defined by [4]

$$\bar{U} = \frac{1}{N} \sum_{n=1}^{N} U_n \,. \tag{2.56}$$

Mean and variance of $\bar{U}$ are $E(\bar{U}) = E(U)$ and $\sigma_{\bar{U}}^2 = \sigma_U^2 / N$, respectively. Thus the sample mean defined by Eq. (2.56) is an unbiased estimator of the expectation E(U) whose quality increases with the sample size N.

2.3.2.2 Sample Variance

Another fundamental statistic of the sample $\{U_1, U_2, ..., U_N\}$ is the sample variance S^2, which is an estimator of the variance σ_U^2. It is most frequently defined by [4]

$$S^2 = \frac{1}{N-1} \sum_{n=1}^{N} (U_n - \bar{U})^2 \,. \tag{2.57}$$

It can readily be shown that the sample variance in Eq. (2.57) is an unbiased estimator of the variance.

2.3.2.3 Modeling of Data

The progress in digital computer technology over the last years made available powerful numerical tools for statistical purposes. Modeling of data is a method that can be used to estimate simultaneously the parameters of a probabilistic model from the sample $\{U_1, U_2, ..., U_N\}$. The basic approach of data modeling is usually to design a figure-of-merit function that measures the agreement between the data and the model with a particular choice of values of the parameters. The figure-of-merit function is conventionally arranged so that small values represent close agreement [5]. The parameters of the model are then adjusted to achieve a minimum in the figure-of-merit function, yielding best-fit parameters.

Data modeling is used in later chapters to determine numerically the parameters of a *PDF* from a sample $\{U_1, U_2, ..., U_N\}$. First, the elements U_n of the sample are distributed in K equally spaced classes. A good choice [6] of the number of classes is $K \cong \sqrt{N}$. The number of elements within a class is called the frequency. When N grows without bound, the histogram (frequency vs. classes) approaches the *PDF* of the random variable U. For bounded N, data modeling can be used to fit the model of the *PDF* to the histogram yielding best-fit estimates of the probabilistic parameters.

2.4 Referenees

[1] J. W. Goodman, *Statistical Optics* (J. Wiley & Sons, New York, 1985), pp. 7-115.

[2] A. W. Drake, *Fundamentals of applied probability theory* (McGraw-Hill, New York, 1967), pp. 203-276.

[3] A. Papoulis, *Probability, Random Variables, and Stochastic Processes* (McGraw-Hill, New York, 1991), pp. 3-344.

[4] A. Ruegg, *Probabilités et statistique*, Méthodes mathématiques pour l'ingénieur, Vol. IV, (Presses Polytechniques Romandes, Lausanne, 1989).

[5] W. Press, B. Flannery, S. Teukolsky, W. Vetterling, *Numerical Recipes in Pascal*, (Cambridge University Press, Cambridge, 1989), pp. 547–598.

[6] P.-A. Paratte, Ph. Robert, Systèmes de mesure, Traité d'Electricité Vol. XVII, (Presses Polytechniques Romandes, Lausanne, 1986), pp. 41-81.

2.5 Some Distributions, their Means and Variances [2,4]

• *Poisson PMF* for $u_0 = 0, 1, 2, \ldots$

$$\text{pmf}_U(u_0) = \frac{\lambda^{u_0}}{u_0!} e^{-\lambda} \qquad \lambda > 0$$

$$E(U) = \lambda \qquad \sigma_U^2 = \lambda$$

• *Uniform PDF* for $a < u < b$

$$\text{pdf}_U(u) = \frac{1}{b - a} \qquad -\infty < b < a < \infty$$

$$E(U) = (a + b) / 2 \qquad \sigma_U^2 = (b - a)^2 / 12$$

• *Gaussian (normal) PDF* for $-\infty < u < \infty$

$$\text{pdf}_U(u) = \frac{1}{\sigma_U \sqrt{2\pi}} \exp\left\{ - \frac{(u - E(U))^2}{2\sigma_U^2} \right\}$$

$$-\infty < E(U) < \infty \qquad \sigma_U > 0$$

• *Rayleigh PDF* for $u \geq 0$

$$\text{pdf}_U(u) = \frac{u}{\sigma^2} \exp\left\{ - \frac{u^2}{2\sigma^2} \right\} \qquad \sigma > 0$$

$$E(U) = \sqrt{\pi/2}\, \sigma \qquad \sigma_U^2 = (2 - \pi/2)\, \sigma^2$$

• *Negative Exponential PDF* for $u \geq 0$

$$\text{pdf}_U(u) = \lambda e^{-\lambda u} \qquad \lambda > 0$$

$$E(U) = 1 / \lambda \qquad \sigma_U^2 = 1 / \lambda^2$$

• *Gamma PDF* for $u \geq 0$

$$\text{pdf}_U(u) = \frac{u^a e^{-u/b}}{\Gamma(a+1) b^{a+1}} \qquad a > -1, \quad b > 0$$

$$E(U) = (a+1)b \qquad \sigma_U^2 = (a+1)b^2$$

3 White-Light Interferometry

White-light sources in optical interferometry have experienced a revival during the last years. The main reasons are the progress in photodetector array technology and the availability of digital computers to process large amounts of data obtained from interferometers.

When monochromatic light of wavelength λ is used, optical path differences (OPDs) larger than λ can be measured by incremental counting the interference fringes while the OPD is scanned [1]. Absolute measurements, which do not require scanning of the OPD to be measured, are possible using either multiple wavelength [2,3] or white-light sources. The broad spectrum of white-light sources further allows spectral analysis of the measurements. Interesting interferometric techniques using white-light sources have been developed, e.g., coherence scanning microscopy [4,5], temporally or spatially scanned white-light interferometry [6], low coherence reflectometry [7], Fourier transform spectroscopy [8], or dispersive white-light interferometry [9]. The main drawback of white-light sources is their low coherent optical power (radiance).

In terms of Chapter 1, an optical wave may be qualified as a random process. In practical applications, a partial description of the random properties by some statistical averages is sufficient for predicting the outcomes of an experiment. Section 1 is concerned with the definitions of these statistical averages, mainly the optical intensity and the mutual coherence function, and with the criteria by which light is classified as incoherent, coherent, or in general, partially coherent. Temporal and spatial coherence are discussed, and the relationship between the temporal coherence and the spectrum of light is established. Section 2 investigates the coherence of two waves and their ability to interfere. Emphasis is laid on the temporal coherence. The results are used in Section 3 to investigate a dispersive white-light interferometer for absolute distance measurement, using a diffractive element to increase the temporal coherence of the light source and a linear photodetector array to scan the interference signal. The interferometer measures distances in the millimeter range without using mechanically moving parts. The channelled spectrum further allows to compensate the measurement for wavelength sensitive dispersive targets, such as dielectric multilayer systems. Section 4 concludes this chapter on white-light interferometry.

3.1 Statistical Properties of Random Light

In this section, the statistical averages commonly used to describe random light are defined: the optical intensity and the mutual coherence function. The coherence of an optical wave can be separated in two contributions, the temporal and the spatial coherence. Temporal coherence qualifies the ability of a light beam to interfere with a time delayed (but not spatially shifted)

replica of itself. Spatial coherence qualifies the ability of a light beam to interfere with a spatially shifted (but not time delayed) replica of itself.

3.1.1 Optical Intensity

An arbitrary optical wave can be described by the complex-valued wavefunction $U(\mathbf{x},t)$. For example, $U(\mathbf{x},t)$ may take the form $U_0(\mathbf{x})\exp\{j2\pi\nu t\}$ for monochromatic light of optical frequency ν. The optical intensity $I(\mathbf{x},t)$ is the statistical average

$$I(\mathbf{x},t) = E\left(|U(\mathbf{x},t)|^2\right) \tag{3.1}$$

of the instantaneous intensity $|U(\mathbf{x},t)|^2$. The intensity may be time independent or may be a function of time. The former case applies when the optical wave is stationary; that is, the instantaneous intensity fluctuates randomly with time, but its average in Eq. (3.1) is constant. Only stationary optical waves are considered in the following. The intensity can then be determined by time averaging the instantaneous intensity over a long time interval

$$I(\mathbf{x}) = \lim_{T\to\infty} \frac{1}{T} \int_{-T/2}^{T/2} dt\, |U(\mathbf{x},t)|^2 . \tag{3.2}$$

It is important to state that commonly used photodetection systems inherently perform the time averaging in Eq. (3.2), because optical frequencies (typically $\nu \cong 5\cdot 10^{14}$ Hz) exceed the spectral bandwidth of the detection systems (typically $B < 10^9$ Hz) by orders of magnitudes.

3.1.2 Mutual Coherence Function

The spatial and temporal fluctuations of random light are described by the cross-correlation function of $U(\mathbf{x},t)$ at pairs of positions $\mathbf{x}_1$ and $\mathbf{x}_2$ at a time delay τ later, known as the mutual coherence function

$$C(\mathbf{x}_1,\mathbf{x}_2,\tau) = E\left(U(\mathbf{x}_1,t+\tau)U^*(\mathbf{x}_2,t)\right). \tag{3.3}$$

When $\tau = 0$ and the two points coincide so that $\mathbf{x}_1 = \mathbf{x}_2 = \mathbf{x}$, the mutual coherence function equals the intensity in Eq. (3.1) [$I = C(\mathbf{x},\mathbf{x},0)$]. Thus the mutual coherence function carries information about both the intensity and the degree of correlation (coherence) of light. It is convenient to define the complex degree of coherence by

$$\mu(\mathbf{x}_1,\mathbf{x}_2,\tau) = \frac{C(\mathbf{x}_1,\mathbf{x}_2,\tau)}{\sqrt{I(\mathbf{x}_1)I(\mathbf{x}_2)}} , \tag{3.4}$$

which is independent of the intensity. The dependence of μ on time and positions describes the temporal and spatial coherence of light.

3.1.2.1 Temporal Coherence and Spectrum

Consider the fluctuations of stationary light as a function of time when the two points coincide so that $x_1 = x_2 = x$. The stationary random process $U(x,t)$ then has constant intensity $I = E(|U(t)|^2)$ (the x dependence has been omitted to simplify the notation). The random fluctuations of $U(t)$ are characterized by a time interval within which the process is correlated, but uncorrelated when examined over longer time scales. A quantitative measure of this temporal behaviour is established by the temporal coherence function

$$C(\tau) = E\big(U(t+\tau)U^*(t)\big)\,, \tag{3.5}$$

which is the position independent form of the mutual coherence function in Eq. (3.3). Its normalized form

$$\mu(\tau) = \frac{C(\tau)}{C(0)} = \frac{E\big(U(t+\tau)U^*(t)\big)}{I} \tag{3.6}$$

is known as the complex degree of coherence. Its absolute value $|\mu(\tau)|$ is bounded by zero and unity. Usually, $|\mu(\tau)|$ drops from its largest value $|\mu(0)| = 1$ as τ increases and the fluctuations become uncorrelated (incoherent) for sufficiently large τ. If $|\mu(\tau)|$ decreases monotonically with time delay τ, the fluctuations are correlated for $\tau < \tau_c$, but uncorrelated for $\tau >> \tau_c$, where τ_c is the coherence time of the light. The coherence time τ_c is the width of $|\mu(\tau)|$ and is usually defined by the power equivalent width

$$\tau_c = \int_{-\infty}^{\infty} d\tau\, |\mu(\tau)|^2\,. \tag{3.7}$$

Light for which the coherence time τ_c is much longer than the differences of the time delays encountered in an optical system is considered to be completely coherent. Thus, light is coherent if the optical path differences encountered are smaller than the coherence length

$$l_c = nc\tau_c\,, \tag{3.8}$$

where c is the speed of light and n is the refraction index of the medium through which the light propagates (for the sake of simplicity, it is assumed that $n = 1$ in the following). By virtue of the Wiener-Khinchin theorem, the temporal coherence function $C(\tau)$ in Eq. (3.5) and the

unilateral power spectral density $\mathcal{G}^+(\nu)$ of the analytic signal representation of light are related through the Fourier transform (§ 2.2.5)

$$C(\tau) = \int_0^\infty d\nu\ \mathcal{G}^+(\nu)\ e^{j2\pi\nu\tau}\ . \tag{3.9}$$

The spectrum of light is often confined to a narrow band $\Delta\nu$ centered about a center frequency ν_0. Because of the Fourier-transform relation between $\mathcal{G}^+(\nu)$ and $C(\tau)$, the bandwidth $\Delta\nu$ is inversely related to the coherence time τ_c, as illustrated in Fig. 3.1. The coherence time of a light wave can be increased by using an optical filter to reduce the bandwidth $\Delta\nu$. This method of increasing the coherence time of a broad band light source will be used in Section 3.

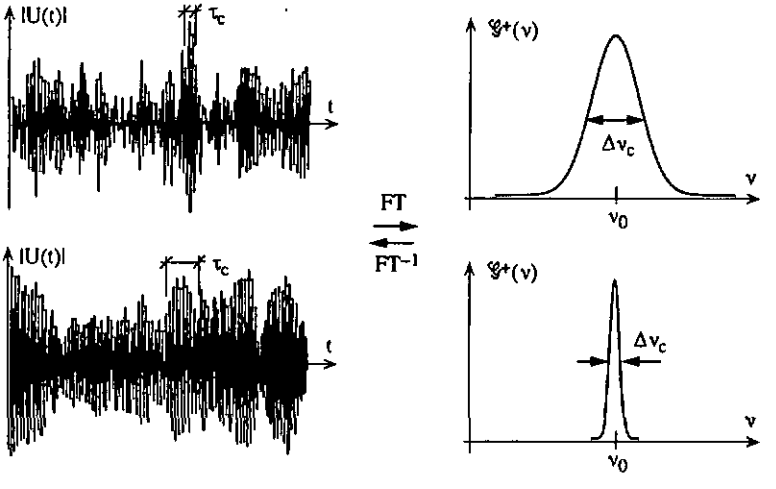

Fig. 3.1 Coherence time τ_c and spectral width $\Delta\nu_c$ are inversely proportional. FT: Fourier transform, FT^{-1}: inverse Fourier transform.

The spectral width $\Delta\nu_c = 1/\tau_c$ is calculated from the power spectral density $\mathcal{G}^+$ through [10]

$$\Delta\nu_c = \frac{\left[\int_0^\infty d\nu\ \mathcal{G}^+(\nu)\right]^2}{\int_0^\infty d\nu\ \left[\mathcal{G}^+(\nu)\right]^2} = \frac{1}{\tau_c}\ . \tag{3.10}$$

Typical values of the coherence time τ_c [coherence length l_c] are 3 fs [800 nm] for filtered sunlight (λ_0 = 600 nm, $\Delta\lambda$ = 400 nm), 45 fs [20 μm] for *LEDs* (λ_0 = 1 μm, $\Delta\lambda$ = 50 nm),

1 ns [30 cm] for filtered gas discharge lamps (e.g. Hg^{198} green line $\lambda_0 = 546$ nm), or 30 ns [10 m] for GaAlAs laser diodes ($\lambda_0 = 780$ nm).

3.1.2.2 Spatial Coherence

The spatial correlation of light is described by the mutual coherence function in Eq. (3.3) for a fixed time delay τ. The normalized mutual coherence function for $\tau = 0$,

$$\mu(\mathbf{x}_1,\mathbf{x}_2) = \frac{C(\mathbf{x}_1,\mathbf{x}_2)}{\sqrt{I(\mathbf{x}_1)I(\mathbf{x}_2)}} , \tag{3.11}$$

is known as the normalized mutual intensity. When the optical path difference encountered in an optical system is much shorter than the coherence length l_c [Eq. (3.8)], the light may be considered temporally coherent and the mutual intensity $\mu(\mathbf{x}_1,\mathbf{x}_2)$ in Eq. (3.11) completely describes the spatial coherence. Again, $|\mu(\mathbf{x}_1,\mathbf{x}_2)|$ is bounded by zero and unity, and it is regarded as a measure of the degree of spatial coherence. The spatial coherence of light in the vicinity of a given position $\mathbf{x}_1$ is unity when $\mathbf{x}_2 = \mathbf{x}_1$ and drops as the distance $|\mathbf{x}_1-\mathbf{x}_2|$ increases. The coherence area S_c is defined by the power equivalent width of $|\mu(\mathbf{x}_1,\mathbf{x}_2)|$ and is calculated through

$$S_c = \int_{-\infty}^{\infty} d^2\mathbf{x}_2 \, |\mu(\mathbf{x}_1,\mathbf{x}_2)|^2 , \tag{3.12}$$

where spatial stationarity of μ has been assumed so that S_c is position independent. If S_c is larger than the size of the aperture through which light is transmitted, so that $|\mu(\mathbf{x}_1,\mathbf{x}_2)| \equiv 1$ at all points of interest, the light is considered to be spatially coherent. Similarly, if S_c is smaller than the resolution of the optical system, i.e., $|\mu(\mathbf{x}_1,\mathbf{x}_2)| = 0$ for practically all $\mathbf{x}_1 \neq \mathbf{x}_2$, the light is spatially incoherent.

To conclude this section, it is stated that complete (temporal or spatial) coherence and incoherence are only idealizations representing the two limits to partial coherence.

3.2 Interference of Partially Coherent Light

When two – or more – optical waves are present simultaneously at the same point of space, the total wavefunction is the sum of the individual wavefunctions. This basic principle of superposition follows from the linearity of the wave equation [10]. For monochromatic waves of the same optical wavelength, the superposition principle must be applied to the complex amplitudes $U(\mathbf{x},t)$, and the intensity of the superposed waves is not necessarily the sum of the intensities of the waves. The difference is attributed to interference, which depends on the phase relationship between the waves. The statistical properties of two partially coherent waves

U_1 and U_2 are described by the degree to which their fluctuations are correlated. At a given position x and time t, the intensities of the two waves are $I_1 = E(|U_1|^2)$ and $I_2 = E(|U_2|^2)$, whereas their cross-correlation is described by the statistical average $C_{12} = E(U_1U_2^*)$ and its normalized form

$$\mu_{12} = \frac{E(U_1U_2^*)}{\sqrt{I_1I_2}} . \tag{3.13}$$

When the two waves are superposed, the intensity I of their sum is

$$I = E\left(|U_1 + U_2|^2\right) = E\left(|U_1|^2\right) + E\left(|U_2|^2\right) + E\left(U_1U_2^*\right) + E\left(U_1^*U_2\right)$$

$$= I_1 + I_2 + 2\sqrt{I_1I_2}\,\mathrm{Re}\{\mu_{12}\} . \tag{3.14}$$

The third term on the right-hand side of Eq. (3.14) represents the optical interference. It is useful to write the interference term in Eq. (3.14) as

$$I = I_1 + I_2 + 2\sqrt{I_1I_2}\,|\mu_{12}|\cos\varphi , \tag{3.15}$$

where $\varphi = \arg\{\mu_{12}\}$ is the phase of μ_{12}. For two completely correlated waves [$\mu_{12} = \exp(j\varphi)$], Eq. (3.15) reduces to $I = I_1 + I_2 + 2\sqrt{I_1I_2}\cos\varphi$. For two completely uncorrelated waves [$\mu_{12} = 0$], there is no interference and Eq. (3.15) becomes $I = I_1 + I_2$. The strength of the interference is measured by the visibility

$$\mathcal{V} = \frac{I_{max} - I_{min}}{I_{max} + I_{min}} , \tag{3.16}$$

also known as the modulation depth or the contrast of the interference pattern. I_{max} and I_{min} are the maximum and the minimum values that the intensity I takes when φ is varied. Since $-1 \le \cos\varphi \le 1$, Eq. (3.15) yields

$$\mathcal{V} = \frac{2\sqrt{I_1I_2}}{I_1 + I_2}\,|\mu_{12}| . \tag{3.17}$$

In the frequently encountered case where $I_1 = I_2$, the visibility reduces to $\mathcal{V} = |\mu_{12}|$.

3.2.1 Interference and Temporal Coherence

The interference function in Eq. (3.14) can be used to investigate the influence of the temporal coherence between two light waves on their ability to interfere. Consider a partially coherent wave $U_0(t)$ with intensity I_0 and complex degree of temporal coherence $\mu(\tau)$ [Eq. (3.6)].

Addition of $U_0(t)$ and a time delayed replica $U_0(t + \tau)$ can be achieved by using an interferometer first introduced by Michelson [1], as sketched in Fig. 3.2. The interferometer is formed by a beamsplitter *BS* and two plane mirrors M_1 and M_2. The collimated light wave $U_0(t)$ is divided by the beamsplitter into two waves $U_1(t) = a_1 U_0(t)$ and $U_2(t) = a_2 U_0(t)$, where a_1 and a_2 are real numbers satisfying $a_1^2 + a_2^2 \leq 1$, and $a_1 > 0$, $a_2 > 0$. The waves $U_1(t)$ and $U_2(t)$ are reflected by the mirrors M_1 and M_2, respectively, and return to the beamsplitter where they are recombined.

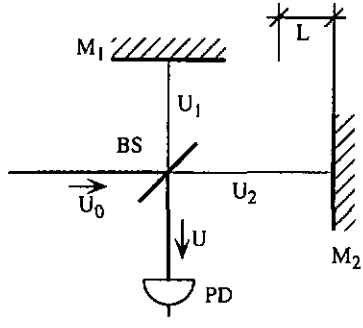

Fig. 3.2 Michelson interferometer.

The difference L between the two arms of the interferometer gives rise to a time delay

$$\tau = \frac{2L}{c} . \tag{3.18}$$

Due to the fast variations of optical waves which are beyond the temporal resolution of commonly used photodetection systems (§ 3.1.1), the photodetector *PD* performs temporal averaging of the optical wave $U = U_1 + U_2$ (or statistical averaging, since the random process U is assumed to be ergodic). The response of the photodetector is therefore governed by the intensity I of the optical wave U [Eqs. (3.1) and (3.2)]. Taking account of the relative time delay τ of the wave U_2 with respect to U_1, the intensity detected by the photodetector can be written as

$$I(\tau) = E\left(|U_1(t)+U_2(t+\tau)|^2\right) . \tag{3.19}$$

Expansion of Eq. (3.19) yields the interference function in Eq. (3.14), with $\mu_{12} = \mu(\tau)$. Introducing $I_1 = a_1^2 I$ and $I_2 = a_2^2 I$, one obtains

$$I(\tau) = I_0 \left(a_1^2 + a_2^2\right)\left[1 + \frac{2a_1a_2}{a_1^2 + a_2^2} \mathrm{Re}\{\mu(\tau)\}\right] . \tag{3.20}$$

In the case of a symmetric beamsplitter without loss ($a_1^2 + a_2^2 = 1$, $a_1 = a_2$), the interference function becomes

$$I(\tau) = I_0 \left[1 + \mathrm{Re}\{\mu(\tau)\}\right] . \tag{3.21}$$

As an example, consider a partially coherent plane wave with complex degree of temporal coherence $\mu(\tau) = |\mu(\tau)| \exp[j2\pi\nu_0\tau]$. Substituting into Eq. (3.21), one obtains $I(\tau)/I_0 = [1+|\mu(\tau)| \cos(2\pi\nu_0\tau)]$, as shown in Fig. 3.3. The relation between I and τ is commonly known as the interferogram. The visibility $\mathcal{V}(\tau)$ of the interferogram has a peak value of unity for $\tau = 0$ and vanishes for $\tau >> \tau_c$, i.e., when the optical path difference 2L is much larger than the coherence length l_c. Interference occurs when the optical path difference is smaller than l_c.

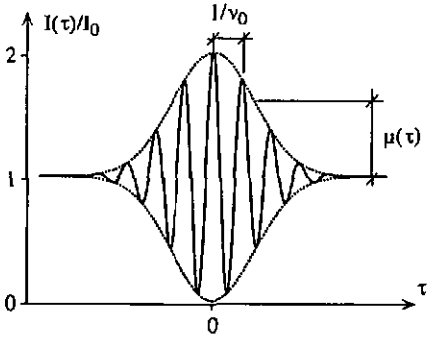

Fig. 3.3 Interferogram of partially coherent light.

It is physically appealing to write Eq. (3.21) in terms of the unilateral power spectral density $\mathcal{G}^+$ of the optical wave. Using the Fourier transform relation between $\mathcal{G}^+$ and C in Eq. (3.9), substituting into Eq. (3.21), and noting that $\mathcal{G}^+(\nu)$ is real and $C(\tau) = I_0\mu(\tau)$, one obtains

$$I(\tau) = \int_0^\infty d\nu\, \mathcal{G}^+(\nu) + \mathrm{Re}\left(\int_0^\infty d\nu\, \mathcal{G}^+(\nu)\, e^{j2\pi\nu\tau} \right)$$

$$= \int_0^\infty d\nu\, \mathcal{G}^+(\nu)\, [1 + \cos(2\pi\nu\tau)] , \tag{3.22}$$

where $I_0 = \int_0^\infty d\nu\, \mathcal{G}^+(\nu)$ has been used.

Equation (3.22) can be interpreted as a weighted (incoherent) superposition of interferograms produced by each of the monochromatic components of the wave. Each component ν produces an interferogram with amplitude $\mathcal{G}^+(\nu)$, period $1/\nu$ and unit visibility $\mathcal{V}$, but the visibility of the composite interferogram reduces for increasing τ as a result of the different periods.

3.2.1.1 Experimental results

The Fourier relationship between power spectral density and temporal coherence function of light [Eq. (3.9)] has been experimentally investigated. The light source was a light emitting diode (*LED* ABB 1A225) working at $\lambda_0 \cong 910$ nm with a spectral bandwidth of approximately $\Delta\lambda_{1/2} = 60$ nm. The coherence length is then $l_c = c\tau_c = \lambda_0^2/\pi\Delta\lambda_{1/2} \cong 4.4$ µm, where a Lorentzian spectrum [10] has been assumed. The spectrum of the light source has been experimentally determined with the help of a monochromator. Figure 3.4 shows a plot of the measured power spectrum $\mathcal{G}^+$ versus the wavelength λ. The weak modulation of the spectrum (spectral period $\Delta\lambda_f \cong 7.6$ nm) is due to Fabry-Perot resonances, similar to those observed in laser diodes which emit light as longitudinal modes of the Fabry-Perot cavity [12]. The spectral separation $\Delta\nu_f$ between the spectral lines, known as the free spectral range [13], is related to the length of the Fabry-Perot cavity d and the index of refraction n of the light emitting medium through $\Delta\nu_f = c/2nd$. Introducing for n = 3.5 (GaAs) and $\Delta\nu_f = c\Delta\lambda_f/\lambda_0^2 \cong 2.88$ THz, one obtains for the length of the cavity approximately d = 15 µm.

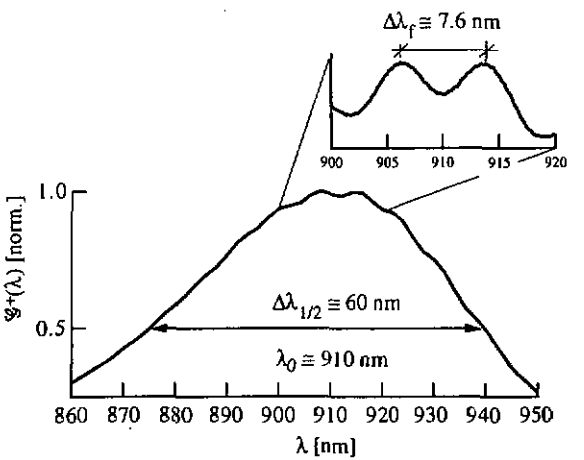

Fig. 3.4 Measured power spectrum of LED ABB 1A225.

The *LED* has then been used in the Michelson interferometer in Fig. 3.2. The mirror M_2 of the interferometer was mounted on a piezo translator (*PZT*) to scan a temporal white-light interferogram [6], which has been detected by the photodetector *PD*. Figure 3.5 shows a plot of the measured intensity I versus the mirror displacement L. The spatial period of the interferogram $\Delta x_p = 455$ nm is half the center wavelength λ_0 of the emitted light. The observed coherence length $l_c \cong 4.6$ µm is in good agreement with the value calculated from the spectral data ($l_c \cong 4.4$ µm). The reappearance of coherence in the interferogram about the mirror displacement $\Delta x_f \cong \pm 52$ µm (Fig. 3.5) results from the periodic modulation of the power spectrum $\mathcal{G}^+$ (Fig. 3.4). The Fourier transform relation between $\mathcal{G}^+$ and C [Eq. (3.9)]

relates Δx_f and the modulation period $\Delta\lambda_f$ through $\Delta x_f = \lambda_0^2/2\Delta\lambda_f$. Introducing for $\lambda_0 = 910$ nm and for $\Delta\lambda_f = 7.6$ nm, one obtains $\Delta x_f = 54$ µm, which is in good agreement with the observed value in the interferogram ($\Delta x_f \cong 52$ µm [Fig. 3.4]).

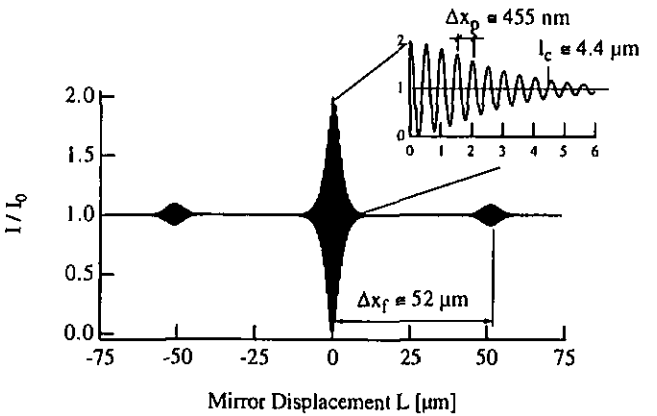

Fig. 3.5 Interferogram of LED ABB 1A225.

The results show that the spectral content of light can be analyzed by Fourier transforming its interference function. This technique is widely used and commonly known as Fourier-transform spectroscopy [8].

3.3 Applications of White-Light Interferometry

3.3.1 Temporally Scanned White-Light Interferometry

Coherence scanning microscopy [4,5] is used for surface topography inspection, profilometry and high resolution imaging. The basic setup of the method is the white-light Michelson interferometer in Fig. 3.2. The object under test is placed in the sensing arm of the interferometer and imaged on a CCD camera at the output of the interferometer. The intensity detected by each pixel of the camera is a function of the degree of coherence $|\mu|$ [Eq. (3.20)] between corresponding points in the object and reference planes. Three-dimensional, topographical images are obtained by monitoring the degree of coherence $|\mu|$ when the optical path difference is scanned by moving the reference mirror along the optical axis.

Displacement sensors based on white-light interferometry are used either directly for measuring and positioning or indirectly for determining other measurements which can be encoded in displacements. A receiver interferometer of the Michelson type, mounted in series with the sensing interferometer, is scanned either temporally or spatially [6]. The intensity detected at the

output of the receiver interferometer is a function of the complex degree of coherence |μ| which is maximum when the optical path differences in the sensing and the receiving interferometers are equal. Monitoring of the degree of coherence |μ| versus the optical path difference in the receiver interferometer yields the displacement measurement. The technique, also known as optical low coherence reflectometry, found various applications in optical fiber sensors [14], optical waveguide testing [15], and non-invasive biomedical investigations [7].

3.3.2 Dispersive White-Light Interferometry

In § 3.1, it has been shown that coherence time τ_c and spectral bandwidth $\Delta\nu$ of light are inversely related [Eq. (3.10)] and that interference only occurs for optical path differences smaller than the coherence length $l_c = c\tau_c$. In this section, a technique for interferometric measurements of optical path differences larger than the *natural* coherence length of the light source is investigated. A dispersive element is used at the output of the interferometer to spatially decompose the spectrum of a white-light source. It results a smaller bandwidth and a longer coherence time of the channelled spectral components. A linear photodiode array then scans the spectral fringe pattern.

For the phase evaluation, we used the method described in Paper I *Absolute distance measurement with synchronously sampled white-light channelled spectrum interferometry*: The local phase of the interference signal is obtained from synchronized sampling with four samples per fringe period. The absolute distance is calculated from the slope of the measured phases against wavelength. The minimum distance is limited by the spectral width of the light source and the maximum distance by the spectral resolution of the dispersive element. Using an *LED* source ($\Delta\lambda \equiv 80$ nm) and a simple diffraction grating (14'000 lines), the range of operation is from 8 μm to 1.9 mm. Experimental results showed an accuracy of better than 2 nm for a distance of 125 μm and better than 12 nm for any position within 50 μm and 150 μm. The absence of any mechanical movement, minimum hardware requirement, and simple data processing algorithm are appealing features in applications as (i) fast distance control systems, (ii) absolute distance measurement devices and (iii) non-contact profilometry.

The use of the interferometer has then been extended to compensate effects of wavelength sensitive dispersive targets, as described in Paper II *Dispersive white-light interferometry for absolute distance measurement with dielectric multilayer systems on the target*: The phase of the reflected wave changes as a function of wavelength and causes errors in the interferometric distance measurement. Spectral analysis of the white-light interferogram allows to measure these effects *in situ*, and the correct mechanical distance can be determined. The method is based on numerical fitting the model of the phase function, which depends on the parameters of the wavelength sensitive target, to the measured phase values. The effects of dielectric multilayer systems on the target have been experimentally investigated for one and two layers

(photoresist on SiO_2 upon Si). The results showed that the thicknesses of these layers can also be determined with an accuracy of the order of 10 nm. The method presented can be readily integrated into distance control systems, such as autofocusing in holographic lithography for microelectronics manufacturing [16], and profilometers based on white-light interferometry.

3.4 Conclusions

The optical intensity and the mutual coherence function are statistical averages commonly used to characterize the random properties of light. The coherence of light can be separated into two contributions: the temporal and the spatial coherence. The relationship between the temporal coherence and the spectrum of light has been experimentally investigated. A dispersive white-light interferometer to measure absolute distances in the millimeter range without mechanically moving parts has been demonstrated. Spectral analysis of the interference signal further allows to compensate the measurement for dispersive targets. Efficient implementations of the interferometer are possible due to the availability of photodetector arrays and digital computers for the data processing. The absence of any mechanical movement, minimum hardware requirement, short data acquisition time, and simple data processing algorithm make the method particularly suited for fast on-line measurement systems in industrial environment.

3.5 References

[1] P. Hariharan, *Optical Interferometry*, Academic Press, Australia, 1985, pp. 151-153.

[2] C. Polhemus, *Two-wavelength interferometry*, Appl. Opt. **12**, 2071 (1973).

[3] Y.-Y Cheng, J. C. Wyant, *Multiple-wavelength phase-shifting interferometry*, Appl. Opt. **24**, 804-807 (1985).

[4] M. Davidson, K. Kaufman, I. Mazor, F. Cohen, *An application of interference microscopy to integrated circuit inspection and metrology*, Proc. Soc. Photo-Opt. Instrum. Eng. **775**, 233-247 (1987).

[5] B. S. Lee, T. C. Strand, *Profilometry with a coherence scanning microscope*, Appl. Opt. 29, 3784-3788 (1990).

[6] A. Koch, R. Ulrich, *Fiber-optic displacement sensor with 0.02 μm resolution by white-light interferometry*, *Sensors and Actuators* A **25-27**, 201-207 (1991).

[7] X. Clivaz, F. Marquis-Weible, R.P. Salathé, R.P. Novàk, H.H. Gilgen, *High-resolution reflectometry in biological tissues*, Opt. Lett. **17**, 4-6 (1992).

[8] P. Hariharan, *Optical Interferometry*, Academic Press, Australia, 1985, pp. 181-193.

[9] J. Schwider, L. Zhou, *Dispersive interferometric profilometer*, Opt. Lett. **19**, 995-997 (1994).

[10] B. E. A Saleh, M. C. Teich, *Fundamentals of Photonics*, J. Wiley & Sons, New York, 1991, pp. 157-192, 342-383.

[11] A. A. Michelson, Phil. Mag. [5] **31**, 338 (1891); **34**, 280 (1892).

[12] S. M. Sze, *Semiconductor Devices*, J. Wiley & Sons, New York, 1985, pp. 252-300.

[13] A. Yariv, *Optical Electronics*, 4th. Ed., Saunders College Publishing, Philadelphia, 1991, pp. 110-147.

[14] D. Inaudi, A. Elamari, L. Pflug, N. Gisin, J. Breguet, S. Vurpillot, *Low-coherence deformation sensors for the monitoring of civil-engineering structures*, *Sensors and Actuators* A **44**, 125-130 (1994).

[15] B. L. Danielson, C. D. Whittenberg, *Guided-wave reflectometry with micrometer resolution*, Appl. Opt. **26**, 2836-2842 (1987).

[16] F. Clube, S. Gray, D. Struchen, J.-C. Tisserand, *Holographic Mask Aligner*, Opt. Eng. 32, 2403-2409 (1993).

4 Detection of Moving Speckles

When a coherent light source such as a laser illuminates a diffusing object, the scattered light takes a granular, random spatial distribution, as illustrated in Fig. 4.1. The unordered and chaotic structure of the granularity is not related to the macroscopic properties of the object under illumination, but depends on the microscopic structure – the roughness – of the object. This physical phenomenon is commonly known as laser speckles [1,2].

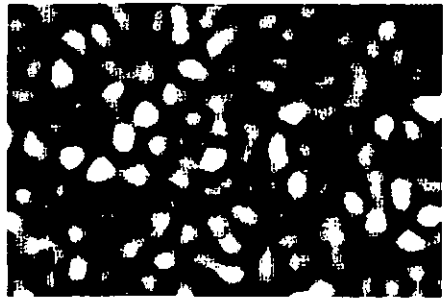

Fig. 4.1 Speckle pattern formed by scattered light from a diffusing object under coherent illumination.

In the beginning, laser speckles were regarded only as annoying spatial noise reducing the resolution of optical systems and falsifying the detection of optical intensities. In the following, it was soon realized that laser speckles are carrying random spatial information on the shape and position of diffusing objects. As a result, speckle phenomenon quickly found a large number of applications, as speckle pattern photography [3,4], speckle pattern correlation interferometry [5,6], and electronic speckle pattern interferometry [7-9]. Detection of dynamic speckles, caused by movement of the diffusing object under illumination, led to many applications to measure displacement and velocity of moving objects [10-13].

In terms of Chapter 2, a speckle pattern may be regarded as a random process in space. Section 1 is concerned with the statistical properties of speckle patterns. First and second order statistics of the intensity and the phase are reviewed. Sums of speckle patterns are also considered. The statistical properties of the complex Fourier transform of the speckle pattern intensity are investigated in detail. Section 2 discusses the impact of speckles on the spatial resolution of optical systems and the accuracy of the intensity measurements. Section 3 deals with detection of moving speckles, caused by in-plane movement of diffusing objects. A speckle pattern based detector, which measures linear displacements and the direction without ambiguity and at arbitrarily low speed, is presented. The statistical properties of the measurement signal are investigated in detail. The application of the method in an optical

computer mouse is discussed in Section 4. The mouse works on arbitrary desk surfaces without any mechanically moving parts. Section 5 deals with noise in photodetection, which imparts random fluctuations to the detected signal. As an example, the results are used for the design of the optical computer mouse. Section 6 finally concludes this chapter on detection of moving speckles.

4.1 Statistical Properties of Speckle Patterns

The physical origin of the speckle phenomenon (Fig. 4.1) is the roughness of most surfaces on the scale of optical wavelengths. When coherent light is reflected from a surface, the optical wave resulting in any moderately distant point results from coherent addition of a multitude of superposed wavelets, each arising from a different microscopic element of the surface under illumination. According to Fig. 4.2a), the distance travelled by the wavelets may differ by many wavelengths if the surface is truly rough. Interference of the randomly dephased wavelets then results in the granular speckle pattern. With reference to Fig. 4.2b), diffraction must be invoked to explain speckle phenomenon in imaging systems. The intensity at a given point in the image plane results from the coherent addition of contributions from many independent surface areas in the object plane. To obtain speckles, it is necessary only that the diffraction limited point spread function of the imaging system is broad compared with the microscopic surface variations, so that a multitude of randomly dephased contributions add at each point in the image plane.

Thus speckles are formed by scattered light from microscopically rough surfaces under coherent illumination and appear either in free-space propagation or in imaging systems.

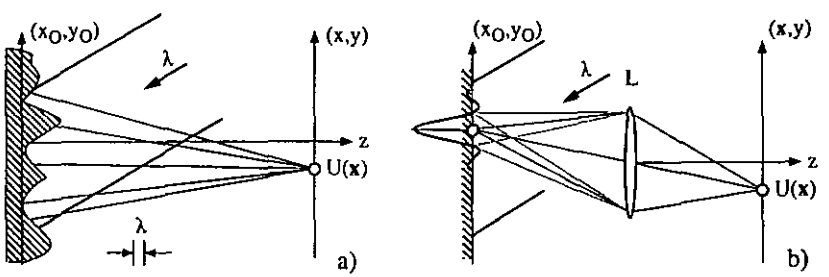

Fig. 4.2 Physical origin of speckle phenomenon in a) free space propagation and b) imaging systems.

4.1.1 First-Order Statistics of Speckle Patterns

4.1.1.1 Linearly Polarized Speckle Patterns

The first-order statistics of linearly polarized speckle patterns are investigated in this section. With reference to Fig. 4.2a), the complex-valued phasor of the optical wave $U(x)$, with amplitude $|U(x)|$ and phase $\phi(x)$, is represented as the sum of many elementary phasors u_n ($n = 1, 2, \ldots, N$)

$$U(x) = |U(x)|\exp\{j\phi(x)\} = \frac{1}{\sqrt{N}}\sum_{n=1}^{N}|u_n(x)|\exp\{j\phi_n(x)\}\ , \tag{4.1}$$

where $|u_n|/\sqrt{N}$ and ϕ_n are the amplitude and phase of the nth elementary phasor, respectively. In order to investigate the statistical properties of the phasor U, the intensity $I = |U|^2$ and phase ϕ of the optical wave, the following assumptions are made:

(i) The amplitude $|u_n|/\sqrt{N}$ and the phase ϕ_n of the nth elementary phasor u_n are statistically independent of each other and of the other N–1 phasors.

(ii) The phases ϕ_n are uniformly distributed in the interval $[-\pi,\pi]$. This assumption is fulfilled if the surface roughness ρ is large compared with the optical wavelength.

According to § 2.1.8 for large N, the joint *PDF* of the real (r) and imaginary (i) parts of the optical wave in Eq. (4.1) [$U(x) = r(x) + j\cdot i(x)$] obeys circular complex Gaussian distribution

$$\mathrm{pdf}(r,i) = \frac{1}{2\pi\sigma^2}\exp\left\{-\frac{r^2 + i^2}{2\sigma^2}\right\}\ , \tag{4.2}$$

with $\sigma^2 = E(|U|^2)/2$. The joint *PDF* of the intensity I and the phase ϕ [$\mathrm{pdf}(I,\phi)$] is obtained by change of variables $I = r^2 + i^2$ and $\phi = \tan^{-1}(i/r)$ in Eq. (4.2). Integration over the corresponding variables yields (§ 2.1.2) the marginal *PDF* of the intensity I

$$\mathrm{pdf}(I) = \begin{cases} \dfrac{1}{2\sigma^2}\exp\left\{-\dfrac{I}{2\sigma^2}\right\} & I \geq 0 \\ 0 & \text{otherwise} \end{cases}\ , \tag{4.3}$$

and the phase ϕ

$$\mathrm{pdf}(\phi) = \begin{cases} \dfrac{1}{2\pi} & -\pi < \phi \leq \pi \\ 0 & \text{otherwise} \end{cases}\ . \tag{4.4}$$

Note that pdf(I,ϕ) = pdf(I)pdf(ϕ) indicating that intensity and phase of speckle patterns are statistically independent.

From Eq. (4.3), the expectation and the second order moment of the intensity are $E(I) = 2\sigma^2$ and $E(I^2) = 2E^2(I)$, respectively. The variance of the intensity is therefore $\sigma_I^2 = E(I^2)-E^2(I) = E^2(I)$. If the contrast Γ of the speckle pattern intensity is defined as the ratio between the standard deviation σ_I and the expectation E(I), it follows that the contrast of a linearly polarized speckle pattern is $\Gamma = \sigma_I/E(I) = 1$.

4.1.1.2 Fist-order Statistics of Sums of Speckle Patterns

In many practical situations, the intensity results from a sum of two – or more – polarized speckle patterns. If the light fields are coherent, the amplitudes add and the first-order statistics of the speckle pattern intensity do not change [1]. If the light fields are incoherent, e.g., when the rough surface depolarizes the scattered light or when the illuminating beam contains several optical wavelengths, the intensities add and the first-order statistics change.

Consider incoherent superposition of M linearly polarized speckle patterns which are statistically independent, with intensities I_m (m = 1, 2, ..., M) and identical expectations $E(I_m)$. The total intensity is then

$$I = \sum_{m=1}^{M} I_m \ . \tag{4.5}$$

Its expectation E(I) is the sum of the expectations of the individual speckle pattern intensities

$$E(I) = \sum_{m=1}^{M} E(I_m) = M\ E(I_m) \ . \tag{4.6}$$

The second order moment is calculated through

$$E(I^2) = E\left(\left[\sum_{m=1}^{M} I_m \right]^2 \right) = E\left(\sum_{m=n} I_m{}^2 \right) + E\left(\sum_{m \neq n} I_m I_n \right)$$

$$= M\,E(I_m{}^2) + M(M-1)E(I_m)E(I_n) \ . \tag{4.7}$$

Introducing $E(I_m{}^2) = 2E^2(I_m)$ in Eq. (4.7) and using the result in Eq. (4.6), one obtains

$$E(I^2) = (M^2 + M)\ E^2(I_m) = \frac{M+1}{M}\ E^2(I) \ . \tag{4.8}$$

The variance $\sigma_I^2 = E(I^2)-E^2(I)$ of the total intensity I in Eq. (4.5) is then

$$\sigma_I^2 = \frac{1}{M} E^2(I) , \tag{4.9}$$

and the speckle contrast $\Gamma_M = \sigma_I / E(I) = 1 / \sqrt{M}$.

It can be shown [14] that the approximate *PDF* of the total intensity I in Eq. (4.5) is

$$pdf(I) = \left(\frac{M}{E(I)}\right)^M \frac{I^{M-1}}{\Gamma(M)} \exp\left\{- M \frac{I}{E(I)}\right\} , \tag{4.10}$$

where $\Gamma(\cdot)$ is the gamma function of $(\cdot)$. Figure 4.3 shows a plot of the *PDF* in Eq. (4.10) for different values of M. Note that for M = 1, Eq. (4.10) is identical with the negative exponential distribution in Eq. (4.3), and at the limit for $M \to \infty$, Eq. (4.10) approaches a Dirac delta function $\delta(I-E(I))$, in which case the standard deviation σ_I and thus the speckle contrast Γ_∞ approach zero.

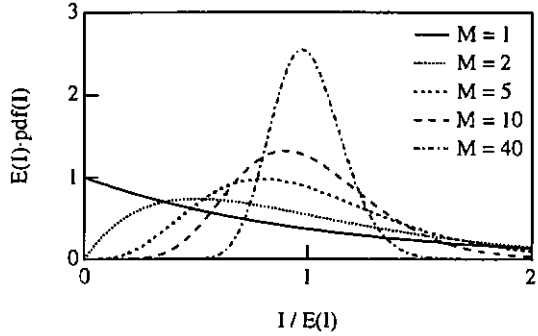

Fig. 4.3 Probability density function of the intensity for different numbers M of incoherently superposed speckle patterns.

4.1.2 Second-Order Statistics of Speckle Patterns

In the previous section, the first-order statistics of speckle patterns have been investigated to describe the probabilistic behaviour in a single point. The second-order statistics are discussed in this section to describe the probabilistic behaviour of the spatial structure of speckle patterns. Namely the autocorrelation function, from which the average speckle size is calculated, and the power spectral density are of interest.

4.1.2.1 Free Space Propagation

Consider the free space propagation geometry in Fig. 4.2a). A coherent light wave U_O of optical wavelength λ is incident on the rough surface. The field reflected from the surface is written as $U(x_O) = U_O(x_O)\rho(x_O)$, where $p(x_O) = |p(x_O)|\exp\{j\psi(x_O)\}$ describes the surface

roughness. The complex field $U(x)$ in the observation point x is obtained from $U(x_O)$ by the Fresnel-Kirchhoff [15] integral

$$U(x) = \frac{\exp\{jkz\}}{j\lambda z} \int_{-\infty}^{\infty} d^2x_O \, U_O(x_O)\rho(x_O) \exp\left\{ \frac{jk}{2z}(x-x_O)^2 \right\}, \tag{4.11}$$

where $k = 2\pi/\lambda$ is the wave vector.

To calculate the autocorrelation function C_U of the complex field U, the following assumptions about the statistical properties of the surface roughness ρ are made:

(i) The phase ψ is uniformly distributed in the interval $[-\pi,\pi]$, so that $E(\rho) = E(|\rho|)E(\psi) \equiv 0$.
(ii) The correlation length l_ρ of the surface roughness is smaller than the optical wavelength λ ($l_\rho < \lambda$), so that [16]

$$E\big(\rho(x_1)\rho^*(x_2)\big) = \frac{\lambda^2}{\pi}\delta(x_1-x_2). \tag{4.12}$$

Introducing Eq. (4.11) in $C_U(x_1,x_2) = E\big(U(x_1)U^*(x_2)\big)$, followed by an interchange of orders of integration and averaging yields

$$C_U(x_1,x_2) = \frac{1}{\pi z^2} \exp\left\{ \frac{jk}{2z}\left(x_1^2-x_2^2\right) \right\} \hat{I}_O\big(\Delta x/\lambda z\big), \tag{4.13}$$

where $I_O = |U_O(x_O)|^2$ is the intensity distribution of the illuminating wave, $\hat{I}_O = FT\{I_O\}$ and $\Delta x = x_1-x_2$. It is convenient to define the normalized correlation factor

$$\mu(x_1,x_2) = \frac{E\big(U(x_1)U^*(x_2)\big)}{E\big(|U(x)|^2\big)} \tag{4.14}$$

and the real-valued degree of correlation

$$|\mu(\Delta x)| = \frac{\left|\hat{I}_O(\Delta x/\lambda z)\right|}{\left|\hat{I}_O(0)\right|}. \tag{4.15}$$

The autocorrelation of the speckle pattern intensity I can be calculated through

$$C_I(x_1,x_2) = E\big(U(x_1)U^*(x_1)U(x_2)U^*(x_2)\big)$$

$$= E\big(U(x_1)U^*(x_1)\big)E\big(U(x_2)U^*(x_2)\big) + E\big(U(x_1)U^*(x_2)\big)E\big(U^*(x_1)U(x_2)\big). \tag{4.16}$$

Introducing Eqs. (4.14) and (4.15) into Eq. (4.16) finally yields

$$C_I(\Delta x) = E^2(I)\left(1 + |\mu(\Delta x)|^2\right). \tag{4.17}$$

The result shows that the autocorrelation of the speckle pattern intensity in free space propagation geometry is given by the Fourier transform of the intensity distribution of the illumination spot.

The average area A_s of a speckle is commonly defined by the power equivalent surface of the autocorrelation function

$$A_s = \int_{-\infty}^{\infty} d^2x\, |\mu(x)|^2 = (\lambda z)^2 \frac{\int_{-\infty}^{\infty} d^2x\, |I_O(x)|^2}{\left[\int_{-\infty}^{\infty} d^2x\, I_O(x)\right]^2}, \tag{4.18}$$

where Parseval's theorem [17] has been used to obtain the third expression in Eq. (4.18).

The power spectral density $\Psi(\mathbf{p})$ of the speckle pattern intensity I is calculated by Fourier transforming the autocorrelation function $C_I(x)$ in Eq. (4.17), according to the Wiener-Khinchin theorem (§ 2.2.4). The result is

$$\Psi(\mathbf{p}) = E^2(I)\left\{\delta(\mathbf{p}) + \frac{\int_{-\infty}^{\infty} d^2x\, |I_O(x)|^2\, |I(x-\lambda z p)|^2}{\left[\int_{-\infty}^{\infty} d^2x\, |I_O(x)|^2\right]^2}\right\}, \tag{4.19}$$

where $\mathbf{p}$ and $\mathbf{x}$ are conjugate Fourier coordinate vectors. Thus the power spectral density consists of a Dirac delta function at zero spatial frequency and a component extended over spatial frequencies given by the normalized autocorrelation function of the intensity distribution of the illumination spot.

4.1.2.2 Imaging Geometry

With reference to Fig. 4.2b), consider imaging of a diffusing object under coherent illumination. The scattered light wave $U(x_O) = U_O(x_O)p(x_O)$ is imaged by the lens L. The light wave $U(x)$ in the image plane is then

$$U(x) = \int_{-\infty}^{\infty} d^2x_O\, U_O(x_O)\rho(x_O)\, h(x - m x_O), \tag{4.20}$$

where h(x) is the diffraction limited point spread function of the imaging system

$$h(x) = \frac{1}{\sqrt{A_p}\lambda d_l} \int_{-\infty}^{\infty} d^2x_P \; P(x_P) \exp\left\{-j \frac{2\pi}{\lambda d_l} x_P \; x\right\} . \tag{4.21}$$

A_P is the aperture surface of the pupil of the imaging lens, d_l is the distance between the lens L (with focal length f) and the image plane, $m = (d_l/f)-1$ is the magnification factor of the imaging system, $P(x_P)$ is the complex-valued pupil function and x_P is the spatial coordinate vector in the pupil plane.

The average intensity $E(I(x)) = E\left(U(x)U^*(x)\right)$ in the image plane is calculated using Eq. (4.20), followed by an interchange of orders of integration and averaging. The result is

$$E(I(x)) = \int_{-\infty}^{\infty} d^2x_O \; |U_O(x_O)|^2 \; |h(x-mx_O)|^2 . \tag{4.22}$$

The autocorrelation function $C_U(x_1,x_2) = E\left(U(x_1)U^*(x_2)\right)$ of the light wave $U(x)$ in the image plane is calculated using Eq. (4.20), followed by an interchange of orders of integration and averaging. Assuming that the intensity distribution $|U_O(x_O)|^2$ of the illumination wave varies slowly within the resolution spot of the imaging system, the result in Eq. (4.12) can be used and the autocorrelation function becomes

$$C_U(x_1,x_2) \cong |U_O(x_O)|^2 \int_{-\infty}^{\infty} d^2x_O \; h(x_1-x_O)h^*(x_2-x_O) = E(I(x)) \; \mu(x_1-x_2) , \tag{4.23}$$

where

$$\mu(x) = \frac{1}{A_p} \int_{-\infty}^{\infty} d^2x_P \; |P(x_P)|^2 \exp\left\{-j \frac{2\pi}{\lambda d_l} x_P \; x\right\} \tag{4.24}$$

is the normalized autocorrelation function of the point spread function h in Eq. (4.21). Finally, as in the case of free space propagation (§ 4.1.2.1), the autocorrelation of the intensity in the image plane can be written as

$$C_I(\Delta x) = E^2(I) \left(1 + |\mu(\Delta x)|^2\right) . \tag{4.25}$$

Similarly, in accordance with Eq. (4.19), the power spectral density of the speckle pattern intensity I in the image plane is

$$\mathcal{G}(\mathbf{p}) = E^2(I)\left\{ \delta(\mathbf{p}) + \frac{\int_{-\infty}^{\infty} d^2x_P\, |P(x_P)|^2\, |P(x_P - \lambda z \mathbf{p})|^2}{\left[\int_{-\infty}^{\infty} d^2x_P\, |P(x_P)|^2\right]^2} \right\}. \tag{4.26}$$

$\mathcal{G}(\mathbf{p})$ consists of a Dirac delta function at zero spatial frequency and a component extended over spatial frequencies given by the normalized autocorrelation function of the intensity transmittance $|P|^2$ of the lens pupil.

As an example, consider the frequently encountered case of a circular lens aperture of diameter D. The autocorrelation function of the intensity I in Eq. (4.25) is then

$$C_I(r) = E^2(I)\left(1 + \left| 2\,\frac{J_1(\pi r)}{\pi r} \right|^2 \right), \tag{4.27}$$

where $r = |\Delta x|\cdot D/\lambda d_I$ and $J_1(\cdot)$ is the Bessel function of the first kind and order 1 of $(\cdot)$. A plot of the autocorrelation function in Eq. (4.27) is shown in Fig. 4.4a). Fourier transforming Eq. (4.27) yields the power spectral density [1,2]

$$\mathcal{G}(\mathbf{p}) = E^2(I)\left\{ \delta(\mathbf{p}) + \frac{8}{\rho_m^{\,2}\,\pi^2}\left(\cos^{-1}\!\left(\frac{|\mathbf{p}|}{\rho_m}\right) - \frac{|\mathbf{p}|}{\rho_m}\sqrt{1 - \left(\frac{|\mathbf{p}|}{\rho_m}\right)^2} \right) \right\}, \tag{4.28}$$

where $\rho_m = D/\lambda d_I$ is the cut-off spatial frequency. A plot of $\mathcal{G}(\mathbf{p})$ is shown in Fig. 4.4b).

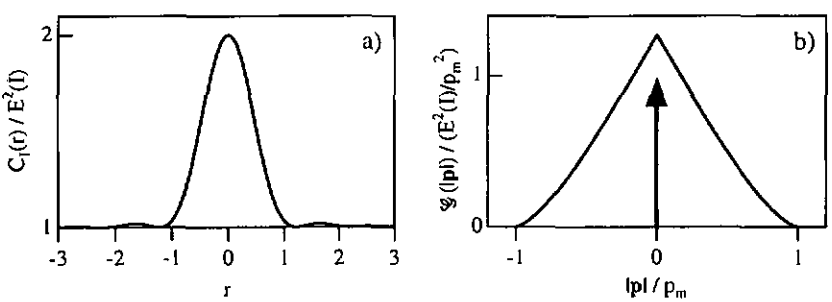

Fig. 4.4 a) Autocorrelation function and b) power spectral density of the speckle pattern intensity in the image plane.

The average surface A_S of a speckle is calculated from Eq. (4.18). The result is $A_S A_P = (\lambda d_I)^2$, where $A_P = \pi D^2/4$ is the aperture surface of the lens pupil, from which the average speckle diameter Δx_S is calculated as

$$\Delta x_s = \frac{4}{\pi}\frac{\lambda d_I}{D}. \tag{4.29}$$

To close this section, it can be shown [1] that the joint *PDF* of the phase ϕ of speckle patterns is

$$\mathrm{pdf}(\phi_1,\phi_2) = \frac{1-|\mu|^2}{2\pi(1-\beta^2)^{3/2}}\left[\beta\,\sin^{-1}\beta + \frac{\pi}{2}\beta + \sqrt{1-\beta^2}\right], \tag{4.30}$$

where $\beta = |\mu|\cos(\phi_2-\phi_1)$ and μ is the correlation factor [Eqs. (4.14) and (4.24)]. Both ϕ_1 and ϕ_2 must be in the interval $[-\pi,\pi]$. Figure 4.5 shows a plot of $\mathrm{pdf}(\phi_1,\phi_2)$ vs. $\Delta\phi = \phi_2-\phi_1$.

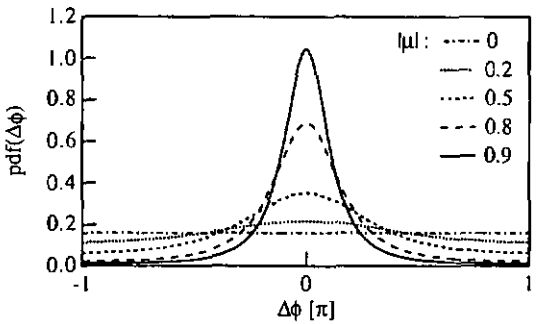

Fig. 4.5 Joint PDF of the phase ϕ of the speckle pattern intensity.

4.1.3 Statistical Properties of the Fourier Transform of Speckle Patterns

The statistical properties of the Fourier transform of the speckle pattern intensity I in the image plane in Fig. 4.2b) is investigated in this section. Using Eq. (4.20), the intensity $I = U(x)U^*(x)$ in the image plane can be described by the two-dimensional convolution integral

$$I(x) = \int_{-\infty}^{\infty} d^2x_O' d^2x_O''\; p(x_O')p^*(x_O'')h(x-x_O')h^*(x-x_O''), \tag{4.31}$$

where x_O' and x_O'' are spatial coordinate vectors in the object plane (The complex-valued phasor U_O of the illuminating beam [Eq. (4.20)] has been omitted in Eq. (4.31) for the sake of simplicity). In general, the Fourier transform of a random process, as the speckle pattern intensity I in Eq. (4.31), does *not* exist [18]. Nevertheless, the statistical properties of the Fourier transform of the speckle pattern intensity

$$\hat{I}(p) = |\hat{I}(p)|\exp\{j\varphi(p)\} = \int_{-\infty}^{\infty} d^2x\; I(x)\exp\{-j2\pi px\} \tag{4.32}$$

can be investigated. $|\hat{I}|$ and φ are the amplitude and phase of the complex Fourier transform $\hat{I}$ at spatial frequency coordinate $\mathbf{p}$. It can be shown (Paper **III**, Appendix A) that for any spatial frequency $\mathbf{p}$ the amplitude $|\hat{I}|$ in Eq. (4.32) is Rayleigh distributed, namely

$$\mathrm{pdf}(|\hat{I}(\mathbf{p})|) = \begin{cases} \dfrac{|\hat{I}(\mathbf{p})|}{\kappa^2(\mathbf{p})} \exp\left\{-\dfrac{|\hat{I}(\mathbf{p})|^2}{2\kappa^2(\mathbf{p})}\right\} & |\hat{I}(\mathbf{p})| \geq 0 \\ 0 & \text{otherwise} \end{cases} , \tag{4.33}$$

and that the phase φ obeys the uniform distribution

$$\mathrm{pdf}(\varphi) = \begin{cases} \dfrac{1}{2\pi} & -\pi \leq \varphi < \pi \\ 0 & \text{otherwise} \end{cases} . \tag{4.34}$$

The parameter κ of the Rayleigh distribution in Eq. (4.33) is a function of the spatial frequency $\mathbf{p}$ and depends on the autocorrelation function $C_{\hat{h}}$ of the Fourier transform $\hat{h}$ of the point spread function h of the imaging system [Eq. (4.21)] through $\kappa(\mathbf{p}) = |C_{\hat{h}}(\mathbf{p})| \cdot \sigma$, where $2\sigma^2 = E(I)$. Mean η and variance χ^2 of the amplitude $|\hat{I}|$ are then given by [19]

$$\eta(\mathbf{p}) = \sqrt{\frac{\pi}{2}}\, |C_{\hat{h}}(\mathbf{p})|\, \sigma \tag{4.35}$$

and

$$\chi^2(\mathbf{p}) = \left(2 - \frac{\pi}{2}\right) |C_{\hat{h}}(\mathbf{p})|^2\, \sigma^2 . \tag{4.36}$$

The autocorrelation function $C_{\hat{I}}$ of the Fourier transform $\hat{I}$ of the speckle pattern intensity I is calculated through

$$C_{\hat{I}}(\Delta\mathbf{p}) = E\left(\hat{I}(\mathbf{p})\, \hat{I}^*(\mathbf{p}-\Delta\mathbf{p})\right) . \tag{4.37}$$

It can be shown (see Paper **III**, Appendix B) that Eq. (4.37) becomes

$$C_{\hat{I}}(\Delta\mathbf{p}) = C_{\hat{h}}(\mathbf{p})\, C_{\hat{h}}(\Delta\mathbf{p}-\mathbf{p})\, \delta(\mathbf{p})\, \delta(\Delta\mathbf{p}-\mathbf{p}) + C_{|\hat{h}|}{}^2(\mathbf{p})\, \delta(\Delta\mathbf{p}) . \tag{4.38}$$

The Dirac δ-functions in Eq. (4.38) show that different spatial frequency components of the Fourier transform of the speckle pattern intensity are uncorrelated; i.e. $C_{\hat{I}}(\Delta\mathbf{p}) \equiv 0, \forall\, \Delta\mathbf{p} \neq 0$.

In conclusion, it is stated that the amplitude $|\hat{I}|$ of the complex Fourier transform $\hat{I}$ of speckle pattern intensity I is Rayleigh distributed and the phase φ is uniformly distributed, independent

of the spatial frequency coordinate $\mathbf{p}$, and that the Fourier transform components $\hat{I}$ for different $\mathbf{p}$ are uncorrelated.

4.2 Detection of Speckle Patterns and Speckled Images

In the experimental measurement of speckle patterns, the aperture of the photodetector is necessarily of finite size. It results a spatial integration of the speckle pattern which changes the statistics of the measured intensity. A similar effect occurs if the speckle pattern is blurred, e.g., if the speckle pattern moves during the measurement. It can be shown [1,2] that the first-order statistics of integrated (or blurred) speckle patterns equal the statistics of sums of speckle patterns, developed in § 4.1.1.2, where the parameter M is related to the number of correlation cells (number of speckles) M_S within the aperture of the photodetector (or within the integration time of photodetection in the case of blurred speckles) through $M = M_S + 1$.
The influence of speckle noise on the accuracy of intensity measurements can be characterized by the relative average variation $\sigma_I^2 / E^2(I)$ of the detected intensity, which depends on the ratio of the photodetector aperture and the speckle size. The resulting noise is given in a good approximation by [16]

$$\frac{\sigma_I^2}{E^2(I)} = \frac{1}{1+M_S} . \tag{4.39}$$

The number M_S of speckles within the photodetector aperture of area A_D can be calculated using Eq. (4.18). In the case of imaging geometry and for $M_S >> 1$, one obtains (§ 4.1.2.2)

$$M_S = \frac{A_D}{A_S} \cong \frac{A_D A_P}{(\lambda d_I)^2} . \tag{4.40}$$

If A_D is smaller than the speckle area A_S, one gets $M_S \cong 0$ and Eq. (4.39) yields the speckle contrast $\Gamma = 1$ (§ 4.1.1). Equations (4.39) and (4.40) show that accurate intensity measurements in the coherent image of a diffusely scattering object can only be obtained at reduced spatial resolution, well below the diffraction limit of the imaging systems.

4.3 Detection of Moving Speckles

The dynamic behaviour of speckle patterns, caused by in-plane motion of diffusing objects, has been used in the past in many applications to measure displacement and velocity of moving objects. The relation between the speckle pattern variation and the object movement has been investigated in detail [20,21]. Consider illumination of the diffusing object with a Gaussian laser beam with spot diameter 2w and wavefront curvature radius R, as shown in Fig. 4.6. In the

case of free space propagation [Fig. 4.6a)], the displacement vectors $\mathbf{d}_O$ of the diffusing object and $\mathbf{d}$ of the speckle pattern are related through [21]

$$\mathbf{d} = \mathbf{d}_O\left(\frac{z}{R} + 1\right), \tag{4.41}$$

where z is the distance from the object to the observation plane. Equation (4.41) shows that $\mathbf{d}$ is increased as the observation plane is separated from the plane $z = -R$ where boiling speckles exist. Boiling speckles statistically change their shape when the diffusing object moves, but there is no appreciable displacement of their position ($\mathbf{d} = \mathbf{0}$). In addition, the translation direction of the speckle pattern is changed in front of and behind the plane $z = -R$. In the special case of collimated illumination ($R \to \infty$), Eq. (4.41) reduces to $\mathbf{d} = \mathbf{d}_O$.

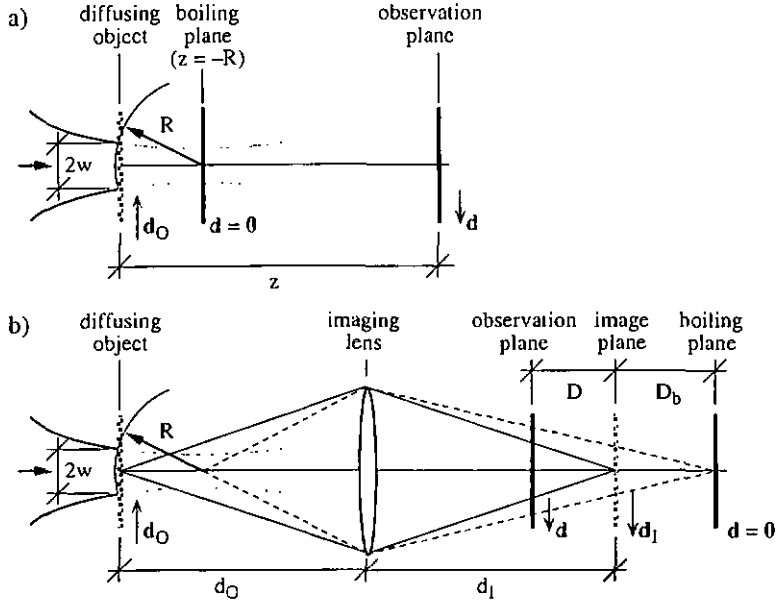

Fig. 4.6 Dynamic speckles in a) free space and b) imaging geometry for illumination of the diffusing object with a converging Gaussian laser beam.

In the case of imaging geometry [Fig. 4.6b)], it can be shown [21] that the displacement vector $\mathbf{d}$ of the speckle pattern in the image space is given by

$$\mathbf{d} = \mathbf{d}_O\, m\left(\frac{D}{D_b} - 1\right), \tag{4.42}$$

where $m = d_I/d_O$ is the magnification factor of the imaging system and, with reference to Fig. 4.6b), D and $D_b = -Rf^2/(d_O-f)(d_O-f+R)$ are the distances from the image plane to the observation and the boiling plane, respectively. Again, the translation direction of the speckle pattern is changed in front of and behind the boiling plane where $d = 0$. When the image equation $[1/f=1/d_O+1/d_I]$ is satisfied, one gets $D = 0$ and Eq. (4.42) reduces to

$$d_I = -m\, d_O\,. \tag{4.43}$$

Equation (4.43) shows that the speckle pattern movement in the image plane of the diffusing object is independent of the illumination.

It is important to note that in both geometries (free space and imaging) dynamic speckles follow boiling or translation motion depending on the conditions of illumination and observation (except in the image plane of the diffusing object). However, at arbitrary observation planes a mixed speckle motion of boiling and translation appears.

Several techniques for detection of movement using speckle patterns have been reported in the past. The methods are based on first-order statistics measurement of speckle pattern intensity variation [10], zero-crossing measurement for the intensity fluctuation of spatially integrated speckle patterns [11], spatial filtering of speckle patterns [12], or speckle pattern correlation measurement [13]. The proposed methods measure constant velocities of diffusing objects and do not detect the direction of the movement. The correlation between sequentially recorded speckle patterns can be used to estimate the movement (and its direction) of the object. This technique suffers from intensive calculation for the two-dimensional correlation estimation.

4.3.1 Detection of Movement with Spatial Filtering of Speckle Patterns

A method for detection of in-plane displacement of diffusing objects, based on spatial filtering of translating speckle patterns, has been published (Paper **III**) and is further discussed in this section. The basic setup is shown in Fig. 4.7. The collimated coherent light beam at optical wavelength λ illuminates the diffusing object moving in a plane perpendicular to the optical axis. Lens L images the object in the image plane at distance d_I. The aperture of the lens is limited by a diaphragm with diameter D. A linearly polarized speckle pattern is obtained with the help of the polarizer P. The proposed photodetector geometry for spatial filtering of the speckle pattern is shown in Fig. 4.8. Two interlaced comb photodetector arrays s_1 and s_2 are connected differentially. Each array has N fingers of width w and length l_y. The finger spacing is Λ and the overall detector length is $l_x = N\Lambda$. By optical matching the speckle size Δx_s [Eq. (4.29)] and the spatial period Λ of the comb photodetector arrays [$\Delta x_s = 2\Lambda/\pi$ (Paper **III**)], the output signal i versus displacement x is zero-offset, quasi sinusoidal with spatial period Λ.

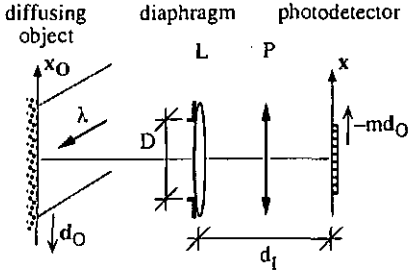

Fig. 4.7 Optical setup for detection of in-plane movement of a diffusing object with speckle pattern.

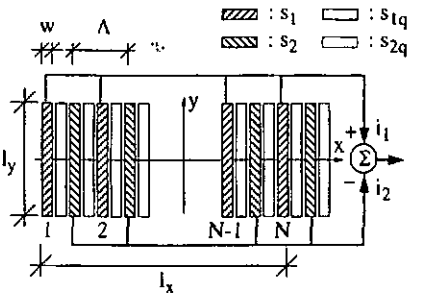

Fig. 4.8 Comb photodetector array for spatial filtering of the speckle pattern.

A typical output signal i versus displacement x is shown in Fig. 4.9. Movements at arbitrary low speed can be measured by zero-crossing detection of this signal. The direction of the movement can be determined with the help of the quadrature signal i_q, which is produced by a second interlaced pair of differentially connected comb photodetector arrays s_{1q} and s_{2q}, shifted by $\Delta x = \Lambda/4$ with respect to s_1 and s_2 (Fig. 4.8). The signal i in Fig. 4.9 can be described by

$$i(x) = u(x)\cos\left(2\pi/\Lambda \cdot x + \phi(x)\right), \tag{4.44}$$

where u(x) and φ(x) are the statistical amplitude and phase, respectively.

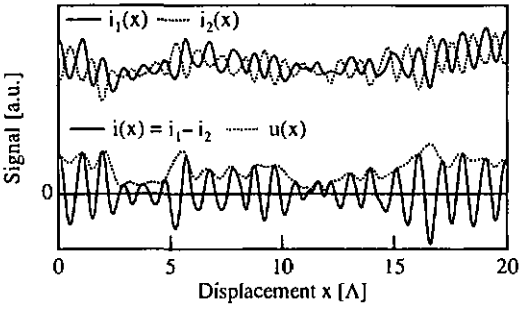

Fig. 4.9 Typical signals $i_1(x)$ and $i_2(x)$ in phase opposition for N = 5 fingers. The zero-offset, quasi sinusoidal output signal i(x) is calculated through $i = i_1 - i_2$. The amplitude u(x) is the envelope function of the output signal i(x).

4.3.1.1 First-Order Statistics of the Output signal

An important first-order statistical property of the output signal i in Eq. (4.44) is the *PDF* of the amplitude u. It can be used to calculate the probability of signal fading, that is, the

probability that the amplitude u is smaller than the minimum value u_{lim} for which zero-crossing can be reliably detected. It can be shown (Paper III) that the amplitude u is Rayleigh distributed, namely

$$\text{pdf}(u) = \begin{cases} \frac{u}{\tau^2} \exp\left\{-\frac{u^2}{2\tau^2}\right\} & u \geq 0 \\ 0 & \text{otherwise} \end{cases} \quad , \tag{4.45}$$

independent of the number N and the length l_y of the fingers of the comb photodetector arrays, i.e., independent of the number of speckles covered by the detector. Mean E(u) and variance σ_u^2 of the amplitude are related to the parameter τ in Eq. (4.45) through $E(u) = \sqrt{\pi/2}\cdot\tau$ and $\sigma_u^2 = (2-\pi/2)\cdot\tau^2$.

This result has been experimentally demonstrated for the experimental setup in Fig. 4.7 (Paper III). The histograms of the amplitude u of the output signal i, obtained from 32'000 measured samples for N = 3, 5, 11 and 25 fingers, are shown in Fig. 4.10. The best fitting [22] Rayleigh distributions, according to Eq. (4.45), are also shown in Fig. 4.10 by solid lines. The mean value E(u) of the amplitude u is proportional to $\sqrt{N}$ and $\sqrt{l_y}$, whereas the ratio $\sigma_u/E(u)$ between the standard deviation σ_u and E(u) is invariant with respect to N and l_y.

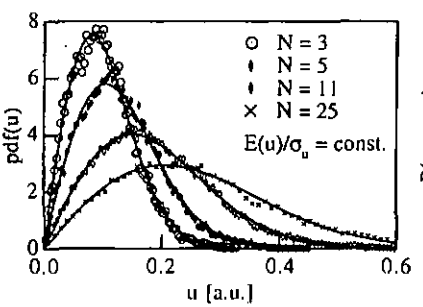

Fig. 4.10 Histogram of the amplitude u of the output signal i, obtained from 32'000 measured samples for N = 3, 5, 11 and 25 fingers. The best fitting Rayleigh distributions are shown as solid lines.

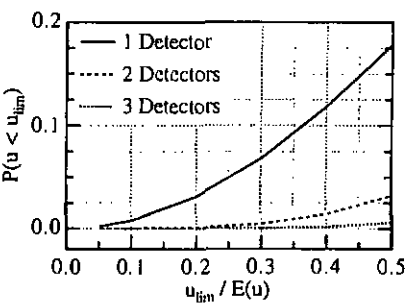

Fig. 4.11 Probability of signal fading versus threshold value u_{lim} of the amplitude u of the output signal in the case of 1, 2 and 3 independent detectors.

The Rayleigh distribution of the amplitude u implies that signal fading cannot be excluded, because the probability for amplitudes smaller than any arbitrary low amplitude u_{lim} gets never zero. Figure 4.11 shows the probability of signal fading $P(u<u_{lim})$ versus the relative threshold $u_{lim}/E(U)$. Using two or more independent detectors increase the reliability, as shown in Fig. 4.11.

4.3.1.2 Second-Order Statistics of the Output Signal

Important second order statistical properties of the output signal i in Eq. (4.44) are the autocorrelation function and the *PDF* of the phase difference $\Delta\phi$ for a displacement Δx. The latter can be used to characterize the accuracy of the measurement and to calculate the probability of an erroneous detection of reversed movement, when the quadrature signal i_q is used to determine the direction of the movement. It can be shown (Paper III) that the autocorrelation function is

$$C_i(\Delta x) = \mu(\Delta x)\cos(2\pi p_0 \Delta x), \tag{4.46}$$

where we have introduced the (normalized) correlation factor

$$\mu(\Delta x) = \begin{cases} 1 - \dfrac{|\Delta x|}{l_x} & |\Delta x| \le l_x \\ 0 & \text{otherwise} \end{cases}, \tag{4.47}$$

which is defined by the envelope of the autocorrelation function in Eq. (4.46). The correlation length l_c of output signal i is defined by the condition $\mu(l_c) = 0$. Using Eq. (4.47), this condition gives for the correlation length $l_c = l_x$.

The joint *PDF* of the phase ϕ of the speckle pattern intensity I in Eq. (4.30) can be adopted to describe the *PDF* of the phase difference $\Delta\phi$ for a displacement Δx of the output signal i. The result is

$$\mathrm{pdf}(\Delta\phi) = \frac{1-\mu^2}{2\pi(1-\beta^2)^{3/2}}\left[\beta \sin^{-1}\beta + \frac{\pi}{2}\beta + \sqrt{1-\beta^2}\right], \tag{4.48}$$

where $\beta = \mu\cos(\Delta\phi - \Delta\bar{\phi})$ and μ is the correlation factor given by Eq. (4.47). For the *PDF* in Eq. (4.48) to be valid, the phase difference $\Delta\phi$ must be in the interval $\Delta\bar{\phi} \pm \pi$, where $\Delta\bar{\phi} = 2\pi/\Lambda \cdot \Delta x$ is the expected phase difference for a displacement Δx. As the correlation factor μ increases, the *PDF* becomes more and more concentrated about $\Delta\bar{\phi}$, indicating that the output signal becomes more and more accurate.

With reference to Fig. 4.12, the probability P_ε that the phase error of consecutive zero-crossings for the displacement $\Delta x = \Lambda/2$ of the output signal i is smaller than ε ($\varepsilon < \pi$) can be calculated by integrating Eq. (4.48) over the interval $\Delta\phi = \Delta\bar{\phi} \pm \varepsilon$, with the correlation factor $\mu = 1 - 1/2N$ [Eq. (4.47)] and the expected phase difference $\Delta\bar{\phi} = \pi$. The result shows that the phase accuracy of the measurement is determined by the number of fingers N of the comb photodetector arrays. The probability to find the next zero crossing within the confidence interval ε are shown in Fig. 4.13 for N = 3, 5, 11, and 25. When the quadrature signal i_q is used to determine the direction of the movement, the phase difference error of the output signal i for the displacement $\Delta x = \Lambda/4$ must be smaller than $|\varepsilon| \le \pi/2$ in order to avoid erroneous

detection of reversed movement. Thus the reliability R_d of the detected direction can be calculated by integrating Eq. (4.48) over the interval $\Delta\phi = \Delta\bar{\phi} \pm \pi/2$, with the correlation factor $\mu = 1-1/4N$ [Eq. (4.47)] and the expected phase difference $\Delta\bar{\phi} = \pi/2$. For N = 3, 5, 11, and 25 fingers, the values of the reliability are R_d = 0.958, 0.975, 0.989, 0.995 and 0.997, respectively. Note that the results of the above considerations are valid under the assumption that no signal fading occurs.

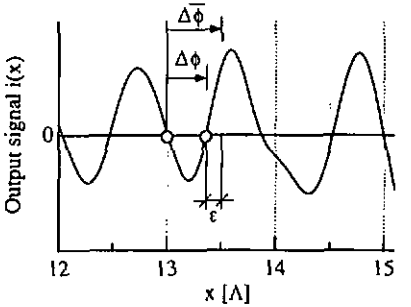

Fig. 4.12 Phase accuracy of output signal i, characterized by the error ε of consecutive zero-crossings.

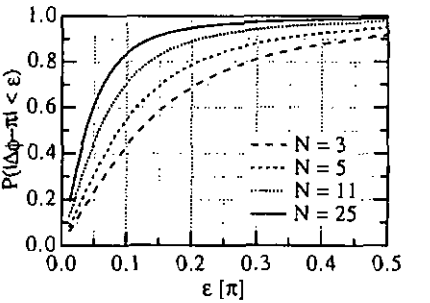

Fig. 4.13 Probability of zero-crossing within the confidence interval ε.

The second order statistical properties of output signal i have been experimentally investigated. Figure 4.14 shows the histogram of phase difference $\Delta\phi$ for a displacement $\Delta x = \Lambda/4$ and $\Delta x = \Lambda/2$, obtained from 32'000 measured samples for N = 5 fingers. The expected phase differences are $\Delta\bar{\phi} = \pi/2$ and $\Delta\bar{\phi} = \pi$, respectively. The theoretical values of the correlation factor μ, obtained from Eq. (4.47), are $\mu(\Lambda/4) = 0.95$ and $\mu(\Lambda/2) = 0.90$. The best fitting [22] *PDFs* from Eq. (4.48) are also shown in Fig. 4.14. The values of the fit parameter are $\mu_{fit}(\Delta x \approx \Lambda/4) = 0.94$ and $\mu_{fit}(\Delta x \approx \Lambda/2) = 0.82$. The autocorrelation function C_i of the measured output signal i for N = 5 fingers is shown in Fig. 4.15 as solid line. The correlation factor μ_m, which is the envelope function of C_i, is represented by the dotted line. For comparison, the theoretical correlation factor μ from Eq. (4.47) is plotted as dashed line. The difference between the theoretical and the experimental correlation factors μ and μ_m in Fig. 4.15 is due to spatial frequency noise in the power spectrum of the measured output signal i. The histogram of the phase difference $\Delta\phi$ of the output signal i for various displacements Δx have been calculated from 32'000 measured samples. The *PDF* in Eq. (4.48) has then been fitted to the histograms. The values of the fit parameter μ_{fit} are indicated in Fig. 4.15 by dots. Note the good agreement between the values μ_{fit} and the measured correlation factor μ_m.

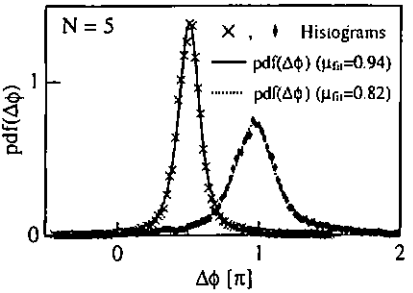

Fig. 4.14 Histogram of the phase difference $\Delta\phi$ for displacement $\Delta x = \Lambda/4$ and $\Lambda/2$ of the output signal i for N=5. The best fitting PDFs are shown as solid and dotted lines.

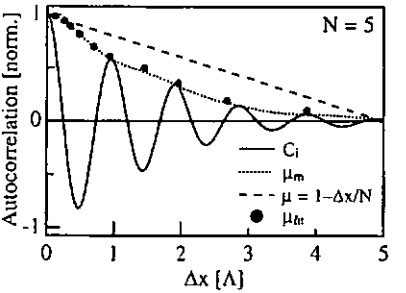

Fig. 4.15 Autocorrelation function C_i and correlation factor μ_m of the measured output signal i. The theoretical correlation factor μ is shown as dashed line. Fitting the PDF to the histograms of the phase difference $\Delta\phi$ yields the values μ_{fit} indicated by dots.

An ideally band pass filtered signal, whose spatial frequency band extends from p_{min} to p_{max}, has an average number of zeros per spatial coordinate unit given by [23]

$$n_{zc} = 2\left(\frac{1}{3} \frac{p_{max}^3 - p_{min}^3}{p_{max} - p_{min}} \right)^{1/2} . \tag{4.49}$$

It has been shown (Paper **III**) that a minimum number of fingers $N_{min} = 3$ is required to avoid overlapping of adjacent spectral bands in the transfer function of the spatial filter (comb photodetector array) and that the power equivalent width of the spectral bands is $\delta p_x = 1/N\Lambda$. Introducing $p_{max} = p_0 + \delta p_x/2$ and $p_{min} = p_0 - \delta p_x/2$ in Eq. (4.49), where $p_0 = 1/\Lambda$ is the carrier spatial frequency, the average number of zero-crossings n_{zc} per spatial period Λ of the output signal i is related to the number of fingers N through

$$n_{zc} = \frac{2}{\Lambda}\left(1 + \frac{(1/2N)^2}{3} \right)^{1/2} \equiv \frac{2}{\Lambda}\left(1 + \frac{1}{24N^2} \right). \tag{4.50}$$

A plot of the relative average error $n_{zc}\cdot\Lambda/2 - 1 \equiv 1/24N^2$ versus N is shown in Fig. 4.16. The result is an important criteria for the accuracy of displacement measurements and shows that the measured distance d_m systematically over-estimates the distance d by the factor $1/24N^2$. Again, the result is valid under the assumption that no signal fading occurs (§ 4.3.1.1). The use of the quadrature signal for direction sensitive detection of the movement might eliminate this effect of the finite bandwidth of the spatial filter on the displacement measurement. A rigorous analysis remains to be done.

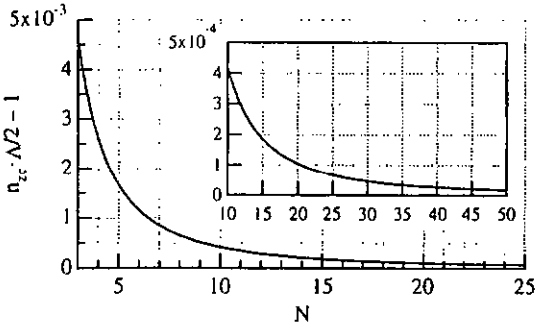

Fig. 4.16 Relative average error of the output signal i versus the number of fingers N.

4.3.1.3 Detection of Two-Dimensional Movement

In the case of two-dimensional displacements, the autocorrelation function C_i in Eq. (4.46) of the output signal i depends on the displacement angle α between the x-axis of the comb photodetector array (Fig. 4.8) and the displacement vector **d** of the speckle pattern. With reference to Fig. 4.17, the value of the correlation factor μ in Eq. (4.47) is proportional to the overlapping area A_c of the detector surface before and after displacement |d| at angle α. The correlation factor μ versus the x-component Δx of the displacement vector **d** and the displacement angle α is readily found by geometrical considerations. The result is

$$\mu(\Delta x,\alpha) = \left(1 - \frac{\Delta x}{l_x}\right)\left(1 - \frac{\Delta x}{l_y}\tan\alpha\right), \tag{4.51}$$

which depends on the overall detector length $l_x = N\Lambda$ and the finger length l_y.

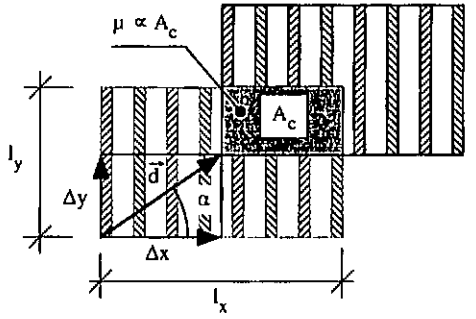

Fig. 4.17 Geometrical representation of the correlation after displacement d.

A plot of the correlation factor in Eq. (4.51) versus Δx for displacement angle $\alpha = 0°$, 45°, 60° and 75° is shown in Fig. 4.18. Note that the correlation length l_c, given by the condition

$\mu(l_c) = 0$, equals the detector length l_x for displacement angles $|\alpha| \le \alpha_d$, where $\alpha_d = \tan^{-1}(l_y/l_x)$ is the angle of the diagonal of the detector, but decreases for $90° \ge |\alpha| > \alpha_d$. Figure 4.19 shows the correlation length l_c versus displacement angle α for comb photodetector arrays with $l_y/l_x = 0.5$, 1 and 2 ($\alpha_d = 26.6°$, 45° and 63°). The maximum displacement angle α_m, where the photodetector array still correctly decodes the x-component Δx of the displacement vector **d**, is limited by the condition $l_c(\alpha_m) = N_{min}\Lambda = 3\Lambda$, which gives for the maximum angle $\tan\alpha_m = l_y/3\Lambda$ for $N > 3$ and $\alpha_m = \alpha_d$ for $N = 3$.

These results show that the output signal i decodes the x-component of the displacement vector **d**. The correlation factor μ, and thus the phase accuracy of the output signal, decreases for increasing displacement angles α. However, high values of correlation between consecutive zero-crossings of the output signal i can be obtained [$\mu(\Delta x = \Lambda/2)$]. Hence zero-crossing detection allows most reliable and accurate displacement measurements for $\alpha < \alpha_m$.

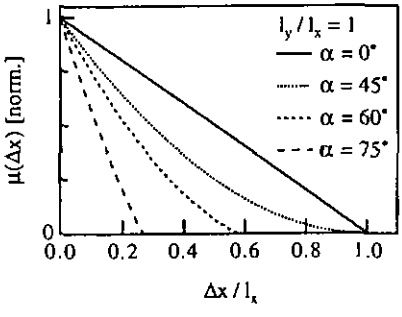

Fig. 4.18 Correlation factor μ versus x-component of the displacement vector d for different displacement angles α.

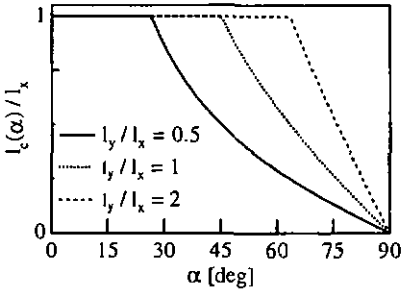

Fig. 4.19 Correlation length l_c versus displacement angle α for different geometries of comb photodetector arrays.

4.3.1.4 Signal Quality

The signal quality is investigated with the help of the ratio $\Gamma^2 = \sigma_i^2 / [E(i_1)+E(i_2)]^2$ between the variance σ_i^2 of the output signal i, which is proportional to the useful rms signal power, and the squared sum of the expectations of the signals i_1 and i_2 of the individual comb photodetector arrays $[E(i_1)+E(i_2)]^2$, which is proportional to the mean power responsible for the detection shot noise. It has been shown (Paper **III**) that the ratio Γ^2 can be analytically approximated by

$$\Gamma^2 = \frac{\sigma_i^2}{4\,E^2(i_1)} \cong \frac{1}{4}\,\frac{\Lambda}{N l_y}\,\mathrm{sinc}^2(w/\Lambda)\,, \qquad (4.52)$$

where $E(i_1)+E(i_2) = 2E(i_1)$ for $E(i_1) = E(i_2)$.

Note that N and the ratio l_y/Λ in Eq. (4.52) are the approximate numbers of uncorrelated speckle cells in the x and y direction, respectively, which are covered by the comb photodetector arrays and contribute to the measurement.

The signal contrast $\Gamma = \sigma_i / [E(i_1)+E(i_2)] = \sigma_i / 2E(i_1)$ is readily found from Eq. (4.52). Figure 4.20 shows a plot of the signal contrast Γ versus the number of fingers N for $l_y/\Lambda = 25$ and $w/\Lambda = 0.25$. The values $\sigma_i / 2E(i_1)$ obtained from the experimentally measured signals i and i_1 (32'000 samples) are shown as dots for N = 3, 5, 7, 11, 25 and 41 fingers. To proof the validity of the analytical approximation in Eq. (4.52), the ratio Γ^2 has been numerically calculated. The square root of the results (Γ) are represented in Fig. 4.20 by the dotted line. Inspection of Fig. 4.20 shows that the simple analytical approximation in Eq. (4.52) can be used as a good estimation of the signal quality Γ^2 and the signal contrast Γ for a given detector geometry.

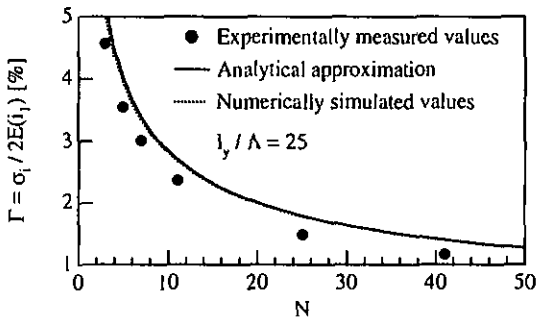

Fig. 4.20 Signal contrast Γ for comb photodetector arrays with N = 3, 5, 7, 11, 25 and 41 fingers ($l_y/\Lambda = 25$, $w/\Lambda = 0.25$, $\Lambda = 100\ \mu m$). The analytically calculated values and the values obtained from numerical calculation are shown as solid and dotted lines, respectively.

4.4 Optical Computer Mouse

A conventional computer mouse has some mechanically moving parts (angular encoders, tracking ball) which are delicate and expensive for the fabrication and susceptible to dust, shock and wear. An optical computer mouse without any mechanically moving parts and working on arbitrary desk surfaces is investigated in this section. Figure 4.21 shows a schematic cross-section of the mouse. The proposed method uses comb photodetector arrays to decode the two-dimensional movement of the speckle pattern, which is produced by imaging the coherently illuminated (rough) desk surface as natural encoding of the movement. (Imaging geometry is proposed, since free space propagation geometry requires an accurate wavefront curvature and spot size of the illuminating beam to obtain a well defined relationship between

the displacement vectors of the surface and the speckle pattern (§ 4.3) and a well defined speckle size (§ 4.1.2.1), which is hardly obtained in large series industrial production). The statistical properties of the output signals, which have been investigated in § 4.3, are used for design considerations of both the geometry of the comb photodetector arrays and the optical imaging system.

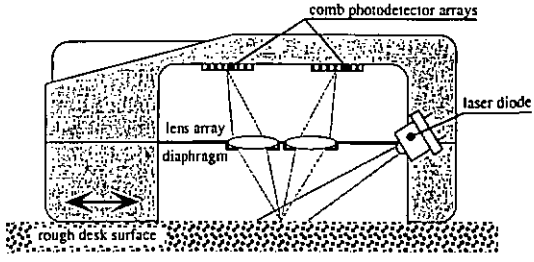

Fig. 4.21 Schematic drawing of an optical computer mouse using comb photodetector arrays to decode the movement of the speckle pattern produced by imaging the coherently illuminated (rough) desk surface.

4.4.1 Design considerations

4.4.1.1 Number of fingers of comb photodetector arrays

From § 4.3.1.2, the phase accuracy of the output signal i of comb photodetector arrays is given by the number of fingers N. Computer mice are displacement sensing devices and do not require high measurement accuracies. Thus a small number of fingers ($N \geq 3$) can be used to maximize the signal modulation Γ (Fig. 4.19) and to minimize the required area on the silicon chip for the sensor.

4.4.1.2 Arrangement of comb photodetector arrays

Two-dimensional movements at any displacement angle α ($0° \leq \alpha < 360°$) must be decoded by a computer mouse. Compact arrangements of three and four square comb photodetector arrays with N = 5 fingers are schematically sketched in Fig. 4.22. (Only one comb array of each detector is represented for the sake of simplicity). The maximum displacement angle α_m, where the individual comb detectors still correctly decode the projection of the displacement vector **d** on the x-axis (Fig. 4.8), is approximately $\alpha_m = \tan^{-1}(l_y/3\Lambda) = \tan^{-1}(5/3) \cong 60°$. It follows that both geometries decode two linearly independent components of **d** at any displacement angle α and thus generate the two-dimensional displacement vector space. The arrangement of four comb photodetector arrays in Fig. 4.22b) is redundant, i.e., at least three comb photodetector arrays decode independently the two components of the displacement vector **d**. Therefore this arrangement has increased reliability, as shown in Fig. 4.11 for two independent detectors.

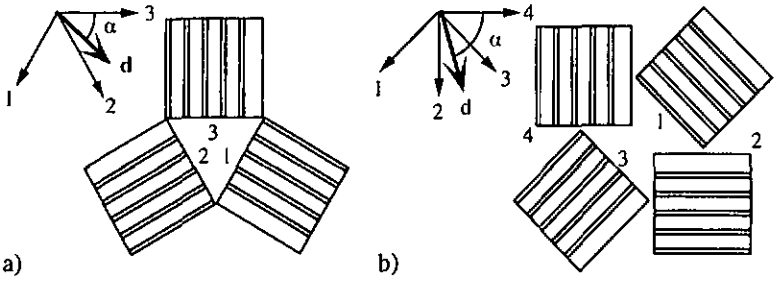

Fig. 4.22 Arrangement of a) 3 and b) 4 comb photodetector arrays for detection of two-dimensional movement. For any displacement angle α, two linearly independent projections of the displacement vector d are decoded. The arrangement of four detectors is redundant and therefore has increased reliability.

4.4.1.3 Power budget and imaging system

Low power consumption is a stringent criteria for the commercial realization of a computer mouse. The rms electric current i_s of the differential output signal i of the comb photodetector arrays is related to the optical power of the light source P_o through

$$i_s = \Gamma\, i_a\,, \tag{4.53}$$

where Γ is the signal contrast, given by Eq. (4.52) [Fig. 4.20], and

$$i_a = S_\lambda\, \eta_s\, \Omega_i\, R_\theta\, P_o\,. \tag{4.54}$$

i_a is the average electric current of the sum of the signals i_1 and i_2 of the individual comb photodetector arrays. S_λ is the spectral sensitivity of the photodetector, η_s is the fillfactor of the photodetector array, Ω_i is the solid angle of the imaging system and $R_\theta = dR/d\Omega$ is the differential scattering reflection coefficient of the desk surface. Assuming optical matching of the speckle size Δx_s and the comb period Λ [$\Delta x_s = 4/\pi \cdot \lambda d_I/D = 2\Lambda/\pi$ (Paper III)], the solid angle of the imaging system, $\Omega_i \equiv \pi(D/2d_O)^2$, is readily expressed by

$$\Omega_i \equiv \pi\left(\frac{m\lambda}{\Lambda}\right)^2, \tag{4.55}$$

where $m = d_I/d_O$ is the magnification factor of the imaging system. The fillfactor η_s in Eq. (4.54), given by the ratio of the (effective) photosensitive area of the comb photodetector arrays and the surface of the imaged illumination spot, is

$$\eta_s = \frac{2Nwl_y}{\pi r_i^2} \tag{4.56}$$

in the case of a circular illumination spot with radius $r_o = r_i/m$. Square comb photodetector arrays are proposed to allow compact arrangements of the detection cells, as shown in Fig. 4.22. Compact arrangements require a minimum spot radius r_i in the detection plane and therefore optimize the power budget, since $i_s \propto (1/r_i)^2$ [Eqs. (4.52) to (4.56)]. Further improvement of the power budget can be achieved using microlens arrays [24,25] for the imaging system, as shown in Fig. 4.21. Each photodetection cell is illuminated by an individual lens, which allows minimum spot radii r_i and maximum fillfactors η_s.

As an example, consider the arrangement of four comb photodetector arrays in Fig. 4.22b), with comb arrays having N = 5 fingers of length l_y = 350 µm and width w = 15 µm and finger spacing Λ = 70 µm. Using a laser diode with output power P_o = 1 mW at λ = 850 nm, and introducing for the spectral sensitivity S_λ = 0.5 A/W and for the differential reflection coefficient $R_\theta \cong 0.1\ sr^{-1}$, the average electric currents i_a of the sum of the signals i_1 and i_2 and the rms electric current i_s of the differential output signal i are calculated from Eqs. (4.52) to (4.56). When a single lens is used for the imaging setup with m = 1, the minimum spot radius is $r_{imin} \cong 700$ µm and the results are $i_a \cong 0.79$ nA and $i_s \cong 73$ pA, respectively. When each detector is illuminated by an individual lens, as shown in Fig. 4.21, the minimum spot radius is $r_{imin} \cong 250$ µm and the results are $i_a \cong 6.3$ nA and $i_s \cong 585$ pA.

4.5 Noise in Photodetection

Photodetectors using light-generated charge carriers are most often employed to measure optical power, e.g., *p-n* junction photodiodes (*PD*), photomultipliers (*PM*), avalanche photodiodes (*APD*), and charge coupled devices (*CCD*). Ideally, they respond to an optical power P_o by generating a proportional electric current i_a. However, any real device generates a random electric current i whose value fluctuates around its mean value $E(i) = i_a$. This random fluctuation, which is referred to as noise, limits the smallest amount of optical power that can be measured. Several sources of noise are inherent in the process of photodetection.

4.5.1 Noise sources

4.5.1.1 Shot Noise

The most fundamental source of noise is associated with the random fluctuations of the arrivals of the (discrete) photons. The mean photon flux for the optical power P_o is $\Phi = P_o/h\nu$, where $h = 6.63 \cdot 10^{-34}$ J·s is Planck's constant and ν is the optical frequency. The number n of photons counted in a time interval Δt is random with mean $E(n) = \Phi\Delta t$. Under the assumption that the photons are statistically independent, the distribution of the number n of photons is described by Poisson statistics [26], for which $\sigma_n^2 = E(n)$ (§2.5). Shot noise is commonly modeled by an equivalent noise current generator with current variance [26]

$$\sigma_{SN}^2 = 2eBi_a, \tag{4.57}$$

where $e = 1.6 \cdot 10^{-19}$ C is the electron charge and B ($\cong$ 1/2RC) is the power equivalent bandwidth of the electric circuit, as shown in Fig. 4.23.

4.5.1.2 Gain Noise

The gain G of some amplifying photodetectors, such as avalanche photodiodes or photomultipliers, has random fluctuations. Each detected photon generates an average number G of carriers but with an uncertainty which depends on the amplification process. The shot noise in amplifying photodetection systems is [26]

$$\sigma_{SN}^2 = 2eGF(G)Bi_a, \tag{4.58}$$

where $F(G) = E(G^2)/E^2(G)$ is the excess noise factor.

4.5.1.3 Dark Current Noise

The electric current which is delivered by the photodetection device in the absence of any optical radiation is referred to as dark current i_d. It is mainly due to random thermal excitation of electrons. Dark current noise is modeled by an equivalent noise current generator with current variance as given in Eq. (4.57) for the shot noise.

4.5.1.4 Thermal (Johnson) Noise

Thermal noise describes the fluctuations of the electric current across a dissipative circuit element. The fluctuations are caused by the thermal motion of the charge carriers. It is commonly modeled by an equivalent noise current generator, with current variance [26]

$$\sigma_{TN}^2 = \frac{4k_B TB}{R}, \tag{4.59}$$

in parallel with the circuit resistor R, as shown in Fig. 4.23. $k_B = 1.3807 \cdot 10^{-23}$ J/K is Boltzmann's constant and T is the absolute temperature. Note that the thermal noise is independent of the signal current i_a.

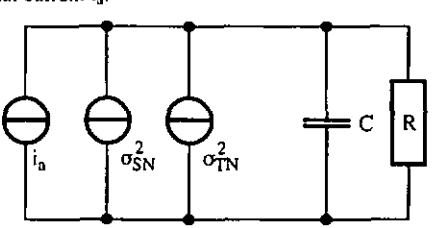

Fig. 4.23 Equivalent electric circuit of a photodetection device. i_a is the signal current, σ_{SN}^2 is the current variance of the equivalent shot-noise current generator, σ_{TN}^2 is the current variance of the equivalent thermal (Johnson) noise current generator.

4.5.2 Signal-to-Noise Ratio

The measurement quality of the detected optical signal is commonly characterized by the signal-to-noise ratio (SNR) of the average electric power of the signal [$P_S = E^2(i)R$] and the noise [$P_N = \sigma_N^2 R$]. Using the results in § 4.5.1, the SNR is

$$SNR = \frac{i_a^2 R}{\left(\sigma_{SN}^2 + \sigma_{TN}^2\right) R} = \frac{i_a^2}{2eBGF(G)(i_a + i_d) + \frac{4k_B TB}{R}}. \tag{4.60}$$

Ideal photodetection systems are shot noise limited, i.e., $\sigma_{SN}^2 >> \sigma_{TN}^2$ and $i_a >> i_d$. The SNR in Eq. (4.60) then reduces to

$$SNR = \frac{i_a}{2eBGF(G)}. \tag{4.61}$$

4.5.2.1 Signal-to-Noise Ratio of the Optical Computer Mouse

As an example, the signal-to-noise ratio of the detection system for the optical computer mouse in § 4.4 is discussed. The signal current i_s and the average current i_a, which is responsible for the shot noise, are given by Eqs. (4.53) and (4.54), respectively. For a photodiode with unity amplification gain and excess noise factor (G = 1, F = 1), the signal-to-noise ratio becomes

$$SNR = \frac{\Gamma^2 i_a^2}{2eB(i_a + i_d) + \frac{4k_B TB}{R}}. \tag{4.62}$$

Consider shot noise limited photodetection ($\sigma_{SN}^2 >> \sigma_{TN}^2$) and $i_a >> i_d$, in which case SNR = $\Gamma^2 i_a / 2eB$. For constant finger width w, inspection of Eqs. (4.52) to (4.56) shows that the SNR is independent of the number N and the length l_y of the fingers but proportional to $1/\Lambda r_i^2$, so that a minimum finger spacing Λ_{min} and spot radius r_{imin} maximizes the SNR.

In the case of thermal noise limited photodetection ($\sigma_{TN}^2 >> \sigma_{SN}^2$), Eq. (4.62) reduces to SNR = $\Gamma^2 i_a^2 / 4k_B T(B/R)$. Introducing Eqs. (4.52) to (4.56) leads to SNR $\propto (N/\Lambda r_i^2)^2$, where square comb photodetector arrays have been assumed ($l_y = N\Lambda$). The SNR increases with the number of fingers N but decreases with increasing finger spacing Λ and spot radius r_i. Note that for both shot noise and thermal noise limited detection the minimum finger spacing Λ_{min} is limited by the silicon technology used for the sensor and the minimum spot radius by the condition $2r_{imin} \geq \sqrt{2} l_y$ (square comb photodetectors).

As an example, the signal-to-noise ratio of the photodetection system in § 4.4.1.2 is calculated. For an equivalent spectral bandwidth $B \cong 2\pi \cdot 10^5$ Hz with resistor $R \approx 1$ MΩ for the electric circuit in Fig. 4.23, the current variance of the equivalent shot noise current generator is $\sigma_{SN}^2 \cong 2.5 \cdot 10^{-23}$ A², when a single lens is used for the imaging system, and $\sigma_{SN}^2 \cong 2 \cdot 10^{-22}$ A²,

when microlens arrays are used to individually illuminate the comb photodetector arrays in Fig. 4.22b). In both cases, the current variance of the equivalent Johnson noise current generator is $\sigma_{TN}^2 \cong 1.7 \cdot 10^{-21}\ A^2$. Thus both configurations are thermal noise limited ($\sigma_{TN}^2 > \sigma_{SN}^2$), and the signal-to-noise ratios are SNR ≅ 5 dB and SNR ≅ 23 dB, respectively.

4.6 Conclusions

Speckle phenomena arise from scattering of coherent light by diffusing objects. The physical origin of the observed granularity in speckle patterns is the roughness of most surfaces on the scale of optical wavelengths. Speckle pattern may be regarded as a random process in space. First and second order statistical properties of speckle patterns have been reviewed, both in free space propagation and in imaging systems. The statistics of integrated and incoherently superposed speckle patterns have also been considered. In general, the Fourier transform of a random process does not exist. However, the statistical properties of the Fourier transform of speckle patterns could be analyzed. It turned out, that the amplitude of the complex Fourier transform of the speckle pattern intensity is Rayleigh distributed and the phase is uniformly distributed, independent of the spatial frequency coordinate, and that the Fourier transform components for different spatial frequencies are uncorrelated.

The dynamic behaviour of speckle patterns, caused by in-plane motion of the diffusing object, has been briefly reviewed. Two different changes in dynamic speckles can be distinguished: boiling and translation. Boiling speckles statistically change their shape when the diffusing object moves, but there is no appreciable displacement of their positions. Translating speckles move as a whole without any significant change in the pattern within the correlation length given by the illuminated surface. Whether dynamic speckles are in the boiling or the translation regime depends on the conditions of illumination and observation. Most dynamic speckle patterns contain both boiling and translating elements.

A method for non-contact detection of in-plane movement of diffusing objects, based on spatial filtering of (translating) speckle patterns, has been presented. Two periodic comb photodetector arrays connected differentially and matching of the speckle size with the period of the photodetector arrays produce a zero offset, quasi-sinusoidal output signal. The movement can then be measured at arbitrarily low speed by zero-crossing detection of this signal. The direction of the movement can be detected with the help of a quadrature signal, which is produced by a second pair of interlaced comb photodetector arrays. First and second order statistical properties of the output signal of these detectors have been investigated theoretically and experimentally to determine reliability and accuracy of the measurement. It turned out, that the amplitude of the signal is Rayleigh distributed, independent of the number and the length of the fingers of the comb arrays, i.e., independent of the number of speckles covered by the

detector. However, correlation length and phase accuracy of the signal are given by the number of fingers. Both, the autocorrelation of the signal and the distribution of the measured phase difference for a given displacement have been calculated for both one and two dimensional displacements of the speckle pattern. The average number of zero-crossings of the signal per unit displacement has been calculated as a function of the number of fingers. In addition, the signal quality (signal-to-noise ratio SNR) has been investigated with respect to the geometry of the comb arrays. The theoretical results have been verified by experimental measurements and by numerical simulations.

The results can be used for optimum design of the geometry of the comb photodetector arrays, the optimization parameters depending on the aimed application. As an example, the application of the technique in an optical computer mouse, which can be operated on arbitrary (rough) desk surfaces, has been discussed. Some design considerations have been detailed.

4.7 References

[1] J. W. Goodman, *Statistical properties of laser speckle patterns*, in *Laser Speckle and Related Phenomena*, 2nd ed., J. C. Dainty, ed. (Springer-Verlag, Berlin, 1984), pp. 9-45.

[2] J. C. Dainty, *The statistics of speckle patterns*, in *Progress in Optics*, Vol. XIV, E. Wolf, ed. (North Holland, 1977), pp. 1-46.

[3] E. Archbold, A.E. Ennos, *Displacement measurement from double-exposure laser photographs*, Opt. Acta **19**, 253-271 (1972).

[4] H. Tiziani, *Application of speckling for in-plane vibration analysis*, Opt. Acta **18**, 891-902 (1971).

[5] J. A. Leendertz, *Interferometric displacement measurement on scattering surfaces utilizing speckle effects*, J. Phys. E: Sci. Instr. **3**, 214-218 (1970).

[6] E. Archbold, J.M. Bruch, A.E. Ennos, *Recording of in-plane surface displacement by double-exposure speckle photography*, Opt. Acta **17**, 883-898 (1970).

[7] R. Jones, C. Wykes, *Holographic and Speckle Interferometry*, Cambridge: Cambridge University Press, 1989, chap. 4.

[8] J.N. Butters, J.A. Leendertz, *Speckle pattern and holographic techniques in engineering metrology*, Opt. Laser Technol. **3**, 26-30 (1971).

[9] A. Macovski, S.D. Ramsey, L.F. Schaefer, *Time-lapse interferometry and contouring using television systems*, Appl. Opt. **10**, 2722-2727 (1971)

[10] J. Ohtsubo, T. Asakura, *Velocity measurement of a diffuse object by using time-varying speckles*, Opt. Quant. Elect. 8 (1976) 523-529.

[11] N. Takai, T. Iwai, T. Asakura, *Real-time velocity measurement for a diffuse object using zero-crossing of laser speckle*, J. Opt. Soc. Am. **70**, 450-455 (1980).

[12] H. Ogiwara, H. Ukita, *A speckle pattern velocimeter using a periodical differential detector*, Jpn. J. App. Phys. Suppl. **14** (1), 307-310 (1975).

[13] B. E. A. Saleh, *Speckle correlation measurement of the velocity of a small rotating rough surface*, Appl. Opt. **14**, 2344-2346 (1975).

[14] J. W. Goodman, *Statistical Optics* (J. Wiley & Sons, New York, 1985), pp. 237-256.

[15] M. Born, E. Wolf, *Principles of Optics*, 6th ed., (Pergamon Press, Oxford, 1980), pp. 370-458.

[16] R. Dändliker, *Heterodyne Holographic Interferometry*, in *Progress in Optics*, Vol. XVII, E. Wolf, ed. (North-Holland, 1980), pp. 1-84.

[17] B. E. A. Saleh, M. C. Teich, *Fundamentals of Photonics*, J. Wiley & Sons, New York, 1991, pp. 918-927.

[18] F. de Coulon, *Théorie et traitement des signaux*, Traité d'Electricité Vol. VI, (Presses Polytechniques Romandes, Lausanne, 1984), pp. 111-144.

[19] J. W. Goodman, *Statistical Optics* (J. Wiley & Sons, New York, 1985), pp. 33-50.

[20] I. Yamaguchi, S. Komatsu, *Theory and applications of dynamic laser speckles due to in-plane object motion*, Opt. Acta. **24**, 705-724 (1977).

[21] T. Asakura, N. Takai, *Dynamic laser speckles and their application to velocity measurements of the diffuse object*, Appl. Phys. **25**, 179-194 (1981).

[22] According to the Levenberg-Marquardt algorithm implemented in the MATLAB function *leastsq*, in *Optimization Toolbox for Use with MATLAB* (MathWorks, Natick, Mass., 1994).

[23] S. O. Rice, *Mathematical analysis of random noise*, Bell System Techn. J. **24**, 46-159, 1945.

[24] Z.D. Popovic, R.A. Sprague, G.A. Neville-Conell, *Techniques for the monolithic fabrication of microlens arrays*, Appl. Opt. **27**, 1281- 1284 (1988).

[25] Ph. Nussbaum, R. Völkel, H.P. Herzig, R. Dändliker, *Micro-optics for sensor applications*, Proc. SPIE **2783**, 55-63 (1996).

[26] B. E. A. Saleh, M. C. Teich, *Fundamentals of Photonics*, J. Wiley & Sons, New York, 1991, pp. 644-695.

5 Final Considerations

The objective of the presented work was to discuss randomness in optical phenomena and the role it plays in optical applications. Some effects of temporal coherence of light, dynamic laser speckles and noise in the process of photon detection have been investigated. The results have been used to design two different types of optical systems, i.e., a dispersive white-light interferometer for absolute distance measurement in the sub-millimeter range and a speckle pattern based displacement sensor for an optical computer mouse working on arbitrary desk surfaces. The validity of both designs have been experimentally demonstrated. Both optical systems are based on physical phenomena which, at first glance, might be regarded as annoying limitations, i.e., the low coherence of white-light sources and the spatial noise (speckles) in scattered light. However, a rigorous analysis and understanding of the physical concepts have led to optimum design and successful demonstration of the systems.

Temporal coherence and speckle theory deal with the statistical properties of two optical phenomena which seem to have no physical relationship. Coherence describes the random fluctuations of light waves due to the superposition of uncorrelated radiations at different optical frequencies and phases, whereas speckle theory describes the random fluctuations of scattered light from diffusing objects under coherent illumination. However, light waves and speckle patterns may be regarded as random processes in time and space, respectively, and the same methods are used to describe mathematically their probabilistic behaviour. The random properties of light waves are usually characterized by statistical averages, namely the optical intensity, the mutual coherence function and the power spectral density. This partial description by some statistical averages is sufficient because commonly used photodetection systems inherently perform time averages due to the optical frequencies which exceed the spectral bandwidth of the detection systems by far. A more complete statistical description of the speckle phenomenon is given by the first and second order probability density functions of the intensity and phase.

Figure 5.1 shows a bloc diagram of an optical measurement system. It is the author's conviction that a system optimization must start with maximizing the optical measurement signal and with minimizing the noise sources in order to obtain the highest value of the (optical) signal-to-noise-ratio (SNR). It follows optimization of the remaining elements in Fig. 5.1 (photon detection, electronic circuits and signal processing). This optimization procedure is justified by the unidirectional signal flux: a bad signal-to-noise ratio at the output of one element cannot be restored by the following elements.

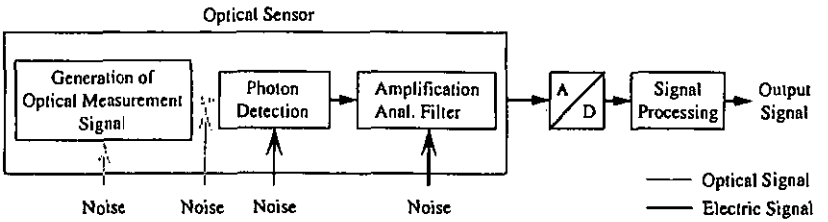

Fig. 5.1 Bloc diagram of an optical measurement system.

As an example, some optimization aspects of the displacement sensor for the optical computer mouse are considered. The optical measurement signal can be maximized by (i) enhancing the speckle contrast with the help of a polarizer [Fig. 4.7 and § 4.1.1.2], (ii) using microlens arrays for maximum power budget [§ 4.4.1.3], and (iii) optimizing the signal contrast with the geometry of the comb photodetector arrays [§ 4.3.1.4]. Imaging geometry eliminates the boiling behaviour in the dynamic speckle pattern [§ 4.3], which may be regarded as noise for the detection of translating speckles.

The progress in digital computer technology over the last years made available powerful tools to numerically simulate models of physical systems. The main advantage of modeling and numerical simulation lies in the fact that the influence of the individual parameters on the system behaviour is distinguishable. A major danger lies in the eventual discrepancy between the behaviour of the real physical system and the generally simplifying model, which might lead to erroneous conclusions. As a result, even best designed, modeled and simulated systems have to be experimentally verified.

Thanks for reading this thesis!

6 Acknowledgements

After five years of pleasant life in Neuchâtel, I would like to take this occasion to thank

- Prof. R. Dändliker for employing me in his research group, for respecting my personality and for everything he taught me during the time that I have been with the *Institut de Microtechnique* (*IMT*).
- the members of the jury, Dr. J. Piot, Prof. F. Pellandini, Prof. J.C. Dainty and Prof. J.W. Goodman for critically reviewing my thesis and for spending some of their precious time in Neuchâtel to discuss it.
- the *Université de Neuchâtel*, the *Commission pour la Technologie et l'Innovation* (*CTI*) and the industrial project partners (Holtronic Technologies SA in Marin and Logitech SA in Romanel), for supporting this research in applied optics.
- the Swiss education system and taxpayers for making my education possible.
- Julien Piot for the lectures on statistics and the fruitful collaboration on the computer mouse project.
- Ken Weible for assisting my practical diploma work in the end of my studies at the *Ecole Polytechnique Fédérale de Lausanne* (*EPFL*), which allowed me to join the *IMT* in 1993.
- Kurt Hug and Philippe Nussbaum for discussing the optical setups and for their valuable suggestions and hints in the laboratory.
- Peter Blattner, Juan Manuel Teijido, Ali Pourzand and Christoph Berger. I was afraid of being on my own with my computer problems when I left the *EPFL*... I was wrong!
- Hans-Peter Herzig for being available to discuss any optical topic at any time.
- Yves Salvadé and Dr. Steen G. Hanson (from RISØ National Laboratory, Denmark), for discussing the speckle displacement sensor.
- Silke Traut and Yves-Alain Peter. The friendly and open environment we had in the office is by far not self-evident.
- Philippe Nussbaum and Marcel Groccia for their friendship and for all our discussions *between men*.
- Wolfgang Singer for his sensitivity he brought into the *IMT*.
- all the other colleagues of the optics group for their daily help.
- all the other members of the *IMT*, the technical and administrative staff for the pleasant atmosphere at the *IMT*.

- Mme and M. Wavre for welcome me in the beautiful *La Mairesse* in Colombier.
- Alain Woodtli and the Tissot family for introducing me into the way of life of the *Littoral de Neuchâtel.*
- my wonderful parents who have always believed in me and supported me during the last thirty-one years of my life, my sister Mitz and my brother Urs for being there whenever help was needed.

and especially

- Liliane for being with me and making me happy.

Thanks to all who helped !

7 Publications

Paper 1

Absolute distance measurement with synchronously sampled white-light channeled spectrum interferometry

U. Schnell, E. Zimmermann, R. Dändliker

We describe a white-light channeled spectrum interferometer for absolute distance measurement in the range of 8 µm to 1.9 mm, using a diffractive element and a linear detector array to scan the interference signal. The local phase of the spectral fringe pattern is obtained from synchronized sampling with four samples per fringe period. The absolute distance is calculated from the slope of the measured phases vs. wavelength. First, the distance is determined to better than λ/8 in order to overcome the phase ambiguity. Then, one of the measured local phases can be used to determine the exact distance with interferometric accuracy. Test results showed an accuracy of better than 2 nm for a distance of 125 µm and better than 12 nm for any position within 50 µm to 150 µm.

Paper 2

Dispersive white-light interferometry for absolute distanee measurement with dielectric multi-layer systems on the target

U. Schnell, R. Dändliker, S. Gray

We have extended a dispersive white-light interferometer for absolute distance measurement to include effects of dielectric multi-layer systems on the target. The phase of the reflected wave changes as a function of wavelength and layer thickness and causes errors in the interferometric distance measurement. With dispersive white-light interferometry these effects can be measured 'in-situ' and the correct mechanical distance can be determined. The effects of thin films deposited on the target have been investigated for one and two layers (photo-resist and SiO_2 on Si). Experimental results show that the thickness of these layers can also be determined with an accuracy of the order of 10 nm.

Paper 3

Detection of movement with laser speckle patterns: Statistical properties

U. Schnell, J. Piot, R. Dändliker

We present an optical method for detection of in-plane movement of a diffusing object. The technique is based on spatial filtering of the laser speckle pattern, which is produced by illumination of the object with coherent light. Two interlaced differential comb photodetector arrays act as periodic filter to the spatial frequency spectrum of the speckle pattern intensity. The detector produces a zero-offset, periodic output signal versus displacement which permits to measure the movement at arbitrarily low speed. The direction of the movement can be detected with the help of the quadrature signal, which is produced by a second pair of interlaced comb photodetector arrays. By matching speckle size and period of the comb photodetector arrays, the output signal versus displacement is quasi sinusoidal with statistical amplitude and phase. First and second order statistics of the signal are investigated. First, the probability density function and the autocorrelation function of the complex Fourier transform of the speckle pattern intensity are determined. Then, the statistical properties of the spectrum of the filtered signal and the signal itself are calculated. It turns out, that the amplitude of the signal is Rayleigh distributed. Both, autocorrelation function of the signal and probability density function of the measured phase difference for a given displacement are calculated. The potential accuracy of displacement measurements is analyzed. In addition, the signal quality is investigated with respect to the geometry of the detector. The theoretical results are experimentally verified.

Paper I

Pure Appl. Opt. 4 (1995) 643–651. Printed in the UK

Absolute distance measurement with synchronously sampled white-light channelled spectrum interferometry

U Schnell, E Zimmermann and R Dändliker

Institute of Microtechnology, University of Neuchâtel, Breguet 2, CH-2000 Neuchâtel, Switzerland

Received 20 February 1995, in final form 9 May 1995

Abstract. We describe a white-light channelled spectrum interferometer for absolute distance measurement in the range of 8 μm to 1.9 mm, using a diffractive element and a linear detector array to scan the interference signal. The local phase of the spectral fringe pattern is obtained from synchronized sampling with four samples per fringe period. The absolute distance is calculated from the slope of the measured phases against wavelength. First, the distance is determined to better than $\lambda/8$ in order to overcome the phase ambiguity. Then, one of the measured local phases can be used to determine the exact distance with interferometric accuracy. Test results showed an accuracy of better than 2 nm for a distance of 125 μm and better than 12 nm for any position within 50 μm to 150 μm.

1. Introduction

Absolute distance measurement with optical interferometry is possible using multiple wavelength [1] or white-light [2] sources. The first method suffers from phase ambiguity when the distance to be measured is larger than the longest synthetic wavelength. The second one requires a receiver interferometer to compensate the pathlength difference. The interferogram is then scanned, either mechanically in the temporal regime or electronically with a photodiode array in the spatial regime. Mechanical scanning suffers from limited speed, whereas spatial electronic scanning is limited to small displacement ranges. To avoid these problems, we present a white-light channelled spectrum interferometer with minimum hardware requirements and simple signal processing. An optical profilometer, which uses a similar approach of white-light interferometry with channelled spectrum detection, has recently been published by Schwider and Zhou [3].

2. White-light channelled spectrum interferometry

The basic set-up of a white-light channelled spectrum interferometer for absolute distance measurement is shown in figure 1. The beam of the white-light source (WLS) is collimated by the lens L_0. The distance L to be measured is the difference between the two arms of the Michelson interferometer formed by a beamsplitter (BS) and two plane mirrors M_1 and M_2. The output light of the interferometer passes through a diffraction grating (DG). The diffracted beam is then focused by the lens L_1 onto a linear photodiode array (PDA). The interference phase $\Phi(\nu)$ is given by

$$\Phi(\nu) = \frac{2\pi}{c} 2L\nu \tag{1}$$

0963-9659/95/050643+09$19.50

where c is the speed of light and ν is the optical frequency. $\Phi(\nu)$ is a linear function of ν and the absolute distance L is directly obtained from the slope $\Phi' = d\Phi/d\nu$ through

$$L = \frac{c}{4\pi}\Phi'. \tag{2}$$

A typical measured channelled spectrum interference signal is shown in figure 2. It can be described as a function of the optical frequency ν by

$$s(\nu) = A(\nu) + B(\nu)\cos\Phi(\nu) \tag{3}$$

where $A(\nu)$ and $B(\nu)$ are slowly varying functions of ν and $\Phi(\nu)$ is given in equation (1).

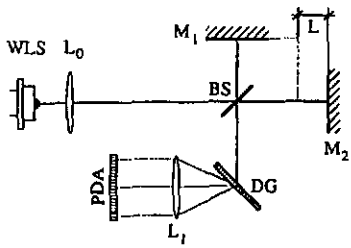

Figure 1. White-light channelled spectrum interferometer for absolute distance measurement using a diffraction grating (DG) and a photodiode array (PDA) for the signal processing.

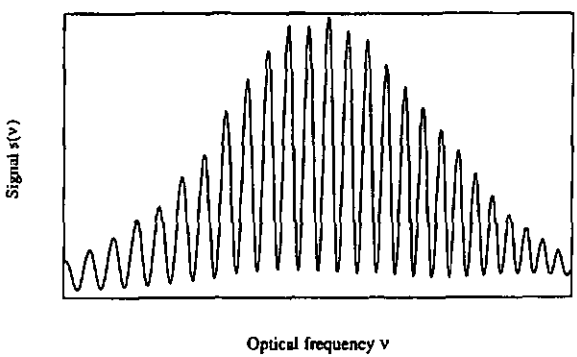

Figure 2. Typical measured white-light channelled spectrum interference signal.

3. Fundamental limitations

The minimum working distance L_{min} is limited by the spectral bandwidth $\Delta\nu_s$ ($\Delta\lambda_s$) of the white-light source. A minimum number of approximately two periods of the interference fringe pattern has to be detected by the photodiode array (PDA) in order to calculate a significant value of the slope Φ' in equation (2). Hence, the minimum working distance L_{min} can be estimated from the total phase variation Φ_t across the spectral fringe pattern by the condition

$$\Phi_t = \frac{4\pi}{c}\Delta\nu_s L = 4\pi\frac{\Delta\lambda_s}{\lambda_0^2}L \geqslant 4\pi \tag{4}$$

which gives for the minimum working distance

$$L_{\min} = \frac{\lambda_0^2}{\Delta\lambda_s} \tag{5}$$

where λ_0 is the centre wavelength of the source.

The maximum working distance $L_{\max}$ is limited by the spectral resolution $\Delta\nu_{sr}$ ($\Delta\lambda_{sr}$) of the diffraction grating. At the limit at least three independent samples per period of the interference signal in equation (3) have to be resolved [4] to determine the phase function $\Phi(\nu)$, because there are three unknowns, $A(\nu)$, $B(\nu)$ and $\Phi(\nu)$. The condition for the distance is

$$\Delta\Phi = \frac{4\pi}{c}\Delta\nu_{sr}L = 4\pi\frac{\Delta\lambda_{sr}}{\lambda_0^2}L \leqslant \tfrac{2}{3}\pi \tag{6}$$

where $\Delta\Phi$ is the phase difference between two spectrally resolved samples, which gives for the maximum working distance

$$L_{\max} = \frac{\lambda_0^2}{6\Delta\lambda_{sr}}. \tag{7}$$

The spectral resolution of the diffraction grating is given by the relation [5]

$$\frac{\lambda_0}{\Delta\lambda_{sr}} = N_L = \frac{D}{g\cos\theta_i} \tag{8}$$

where N_L is the number of illuminated lines on the diffraction grating, g is the grating constant (spatial period), θ_i is the angle of incidence and D is the diameter of the incident beam. Typical values for the set-up shown in figure 1 are $g = 0.5$ μm, $\theta_i = 45°$ and $D = 5$ mm, which gives $N_L \approx 14\,000$ for the grating and $\Delta\lambda_s = 80$ nm at $\lambda_0 = 800$ nm for a LED light source. From equations (5) and (7) we find that this type of white-light channelled spectrum interferometer can be operated in a range of about $L = 8$ μm–1.9 mm.

4. Synchronous sampling

Following the optical arrangement shown in figure 1, the dispersion of the diffraction grating (DG) introduces a frequency spacing $\Delta\nu$ between two adjacent pixels n and $n-1$ of the PDA which results in a phaseshift of

$$\Delta\Phi_s = \Phi_n - \Phi_{n-1} = \frac{4\pi}{c}L\Delta\nu. \tag{9}$$

The local phase Φ_n is then calculated, using five adjacent samples of the interference signal in equation (3) symmetrically centred at the sample s_n, through [6]

$$\begin{aligned} S_n &= s_{n-1} - s_{n+1} = 2B\sin\Delta\Phi_s\sin\Phi_n \\ C_n &= s_n - \frac{s_{n+2}+s_{n-2}}{2} = 2B\sin^2\Delta\Phi_s\cos\Phi_n \\ \Phi_n &= \tan^{-1}\left(\frac{S_n}{C_n}\sin\Delta\Phi_s\right). \end{aligned} \tag{10}$$

For equation (10) to be correct, the $A(\nu)$ and $B(\nu)$ in equation (3) should be constant. In practice, $A(\nu)$ and $B(\nu)$ vary slowly with ν (see figures 1 and 5), but the differences for five adjacent samples are small and equation (10) is still valid. Using equations (3) and (10) it can easily be shown that the corresponding error is given by

$$\delta\Phi_n = -\frac{A_{n+1}-A_{n-1}}{2B_n}\cos\Phi_n \tag{11}$$

which gives a maximum error of about $\delta\Phi_n = 3°$ for a relative slope of the average intensity $(A_{n+1} - A_{n-1})/B_n = 10\%$.

In order to make the phase evaluation simple and to minimize the hardware requirements, we adopted a synchronized sampling of the interference fringe pattern with four samples per fringe period. The optical arrangement of DG, L_1 and PDA in figure 1 is designed so that for the desired working distance L_w the frequency spacing $\Delta\nu$ between two adjacent pixels gives a phaseshift of $\Delta\Phi_s = \frac{1}{2}\pi$. Using equation (2), the measured absolute distance L is then calculated from the slope $\Phi' = d\Phi/d\nu$ of the unwrapped local phases Φ_n. The best value for the slope is obtained by a least squares fit, which averages very efficiently the errors introduced by the non-uniformity (figure 5) of the fringe pattern (equation (11)).

5. Phase evaluation error

When the real distance L differs from the working distance L_w, the phaseshift $\Delta\Phi_s$ becomes

$$\Delta\Phi_s = \tfrac{1}{2}\pi + \varepsilon \tag{12}$$

where the phaseshift error ε is given by

$$\varepsilon = \tfrac{1}{2}\pi\frac{L - L_w}{L_w}. \tag{13}$$

In a first approximation, the local phases are calculated from equation (10) with $\varepsilon = 0$. These values $\Phi_n^{(0)}$ are related to the true phases Φ_n by

$$\Phi_n^{(0)} = \tan^{-1}\left(\frac{1}{\cos\varepsilon}\tan\Phi_n\right). \tag{14}$$

The corresponding phase evaluation error $\delta\Phi^{(0)}$ becomes

$$\begin{aligned}\delta\Phi^{(0)} &= \Phi_n^{(0)} - \Phi_n \\ &= \left[\tan^{-1}\left(1/\sqrt{\cos\varepsilon}\right) - \tan^{-1}\left(\sqrt{\cos\varepsilon}\right)\right]\sin 2\Phi_n \\ &= f_e(\varepsilon)\sin 2\Phi_n \end{aligned} \tag{15}$$

which consists of a periodic part $\sin 2\Phi_n$ and an envelope function $f_e(\varepsilon)$. Introducing equations (1) and (13), the periodic part can be expressed as

$$\sin 2\Phi_n = \sin\left(\frac{16L_w}{\lambda_0}\varepsilon\right). \tag{16}$$

Figure 3 shows the phase evaluation error $\delta\Phi^{(0)}$ as a function of ε for $2L_w/\lambda_0 = 10$. Note that the envelope f_e is only a function of the phaseshift error ε. Numerical simulations show that the phase evaluation error in equation (15) causes an error for the measured distance which can be described by

$$\delta^{(0)}(\varepsilon) = \frac{L^{(0)} - L}{L_w} = \alpha\delta\Phi^{(0)}(\varepsilon) \tag{17}$$

where $L^{(0)}$ is calculated from the $\Phi_n^{(0)}$, obtained in a first approximation with $\varepsilon = 0$. It is seen that the parameter α depends only on the number N of local phases Φ_n used for the least squares fit to calculate the slope Φ'. Figure 4 shows the calculated values of the parameter α as a function of N. The values for $N = 20$ and $N = 50$ are $\alpha = 2 \times 10^{-2}$ rad^{-1} and $\alpha = 4.5 \times 10^{-3}$ rad^{-1}, respectively. Following equation (15), or figure 4, the maximum relative error for the measured distance is $\delta_{max}^{(0)} = \alpha f_e(\varepsilon)$. For $\varepsilon = 45°$ we get $\delta_{max}^{(0)} = 3.4 \times 10^{-3}$ ($N = 20$), or $\delta_{max}^{(0)} = 0.8 \times 10^{-3}$ ($N = 50$).

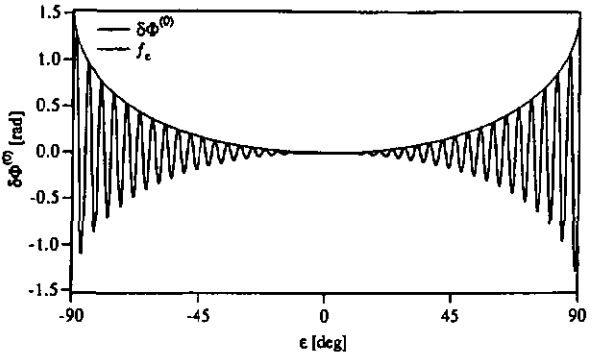

Figure 3. Phase evaluation error $\delta\Phi^{(0)}$ as a function of the phaseshift error ε for $2L_w/\lambda_0 = 10$.

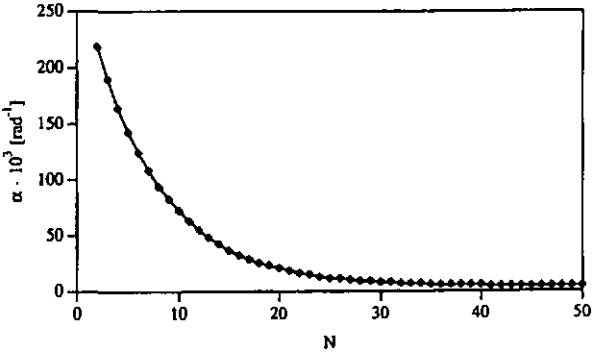

Figure 4. Parameter α as a function of the number N of local phases Φ_n.

Using the first approximation $L^{(0)}$ of the measured distance L, the phaseshift error ε can be calculated through equation (13). Improved values $\Phi_n^{(1)}$ of the local phases can then be calculated from equation (14) by

$$\Phi_n^{(1)} = \tan^{-1}(\cos\varepsilon \tan\Phi_n^{(0)}) \tag{18}$$

which can be used to calculate a better value $L^{(1)}$ of the measured distance L. This iterative phase correction method allows elimination of the phase evaluation error in equation (15) and the error for the measured distance in equation (17).

Unwrapping of the local phases Φ_n is only possible if the phase difference between two adjacent samples

$$\Delta\Phi_n = \Delta\Phi_s + (\delta\Phi_n^{(0)} - \delta\Phi_{n-1}^{(0)}) \approx \Delta\Phi_s \pm \delta\Phi^{(0)} \tag{19}$$

is smaller than π. Using equations (11) and (14), the condition for the phaseshift error is

$$\Delta\Phi_n(\varepsilon) = \tfrac{1}{2}\pi + \varepsilon \pm \delta\Phi^{(0)} \leqslant \tfrac{1}{2}\pi + \varepsilon + 2f_\epsilon(\varepsilon) < \pi \tag{20}$$

which gives for the maximum allowed phaseshift error $\varepsilon_{max} = 56.4°$, which corresponds, following equation (12), to a phaseshift of $\Delta\Phi_s = 146.4°$ instead of 90°.

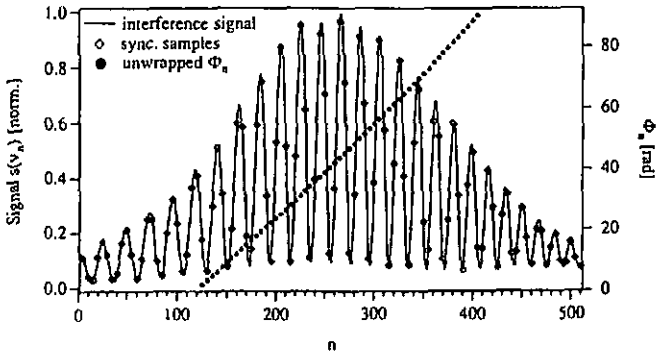

Figure 5. Processing of the channelled spectrum: the observed interference fringes in the spectrum are synchronously detected with four samples per fringe period to calculate the fringe phases. Every fourth sample is graphically emphasized to demonstrate that the sampling is (nearly) synchronous with the fringe pattern.

6. Experimental results

The synchronously sampled white-light channelled spectrum interferometer has been investigated with the help of the optical set-up shown in figure 1. The white-light source was a light emitting diode (LED ABB 1A225) working at $\lambda_0 \cong 890$ nm with a spectral bandwidth of approximately $\Delta\lambda_s = 50$ nm. After the lens L_0 the beam was collimated with a diameter of approximately $D = 4$ mm. The mirror M_2 of the Michelson interferometer was mounted on a piezo translator (PZT) in series with a stepper motor (SM). In order to equalize the two interferometer arms ($L = 0$), the PZT was first used to scan a temporal white-light interferogram [2], detected in the zero order of the diffraction grating. Then, the centre of gravity of the interferogram was calculated [6] and the PZT set so that $L = 0$. A well controlled working distance L_w was then introduced by means of the stepper motor. The diffraction grating had a spatial period $g = 577.36$ nm, and the angle of incidence was $\theta_i = 50.4°$. From equation (8) we get then, with $D = 4$ mm, a spectral resolution for the diffraction grating of $\Delta\lambda_{sr} = 0.08$ nm ($\Delta\nu_{sr} = 30$ GHz). The focal length of the lens L_1 was 60 mm and the linear photodiode array had 512 pixels with a centre-to-centre spacing of $\Delta x = 25$ μm. In this case we get a spectral resolution of the channelled spectrum of 0.16 nm/pixel (60 GHz/pixel). The line scan time was 26.5 ms.

According to equations (5) and (7), this set-up can be operated in a range of $L \cong 16$ μm–830 μm. For a working distance of $L_w = 125$ μm we get a channelled spectrum as shown in figure 5. The fringe spacing is 20 pixels, as expected from the calculated spectral resolution. The synchronized samples s_n have been obtained by adding the measured intensities of five adjacent pixels on the PDA. The synchronized samples s_n and the unwrapped local phases Φ_n are also shown in figure 5. The slope Φ' was calculated by a least squares fit and the absolute distance L was obtained from equation (2).

A statistical analysis of the maximum variation δL of the distance from 50 independent measurements was performed for different numbers N of local phases Φ_n. The results for $N = 17, 37, 57$ and 77 are shown in figure 6 by dots. The expected maximum variation δL_t of the measured distance can also be estimated by using the maximum observed variation $\delta\Phi_n$ of an individual local phase Φ_n and by calculating the variation of the slope Φ' by

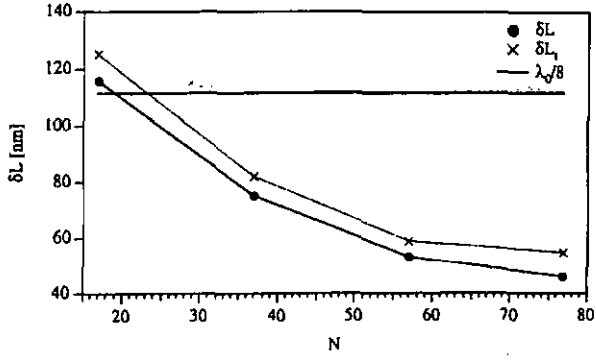

Figure 6. Statistical analysis of the maximum variation δL of the distance from 50 independent measurements compared with the expected maximum variation δL_t as a function of the number N of local phases Φ_n.

considering only the two extreme phase values ($\Delta n = N$). From equation (2) we then get

$$\delta L_t = \frac{c}{4\pi}\delta\Phi' = \frac{c}{4\pi}\frac{\delta\Phi_n}{N\Delta\nu} \tag{21}$$

where $\Delta\nu$ is the frequency step between two samples. The maximum measured variation of an individual local phase Φ_n was $\delta\Phi_n = 25$ mrad and the standard deviation was $\sigma_\Phi = 6$ mrad. The maximum variation δL_t as a function of N, calculated from equation (21), is also shown in figure 6.

If the reproducibility of the measured distance is better than $\lambda_0/8$, the phase ambiguity is overcome and one of the measured local phases Φ_n, preferably at the centre of the fringe pattern can be used to determine the exact distance with interferometric accuracy. The results show that the reproducibility was always better than $\lambda_0/8$ when the number N of the considered local phases was larger than 40 (figure 6). Using the measured maximum value of $\delta\Phi_n = 25$ mrad for the phase variation, the accuracy of the measured distance is $\delta L = 1.8$ nm ($\sigma_L = 0.4$ nm) and the relative accuracy $\delta L/L$ is better than 1.4×10^{-5}. In order to demonstrate the phase evaluation with synchronized sampling, the distance L was scanned with the PZT. The distance was in an approximate range of $L = 125 \pm 25$ μm ($\varepsilon = \pm 18°$). The PZT had 11 bit resolution and $N = 57$ local phases Φ_n were considered. The measured distance L is reported in figure 7 as a function of the voltage U_{pzt} applied to the PZT for increasing and decreasing U_{pzt}. The maximum difference $\delta L = L - L_s$ between the measured distance L in figure 7 and the binomial smoothed† value L_s was $\delta L = 190$ nm, and the standard deviation was $\sigma_{\delta L} = 35$ nm. The relative accuracy is $\delta L/L_w = 1.6 \times 10^{-3}$. The maximum difference $\delta\Phi = \Phi - \Phi_s$ between the measured phase Φ and the binomial smoothed value Φ_s of an individual local phase Φ_n was $\delta\Phi = 174$ mrad ($\sigma_\Phi = 30$ mrad) leading to an accuracy of $\delta L = 12$ nm ($\sigma_{\delta L} = 2$ nm) for the measured distance L_m.

The phase evaluation error and its correction for non-ideal phaseshift $\Delta\Phi_s \neq \pi/2$ is illustrated in figure 8. The uncorrected local phase variation $\delta\Phi^{(0)}$ is depicted as a function of the distance L in a range of $L = 54 \pm 1.5$ μm ($\varepsilon = -51.1° \pm 1.1°$). The theoretical value of the maximum phase error $\delta\Phi^{(0)}$, given by equation (15), is $f_e(\varepsilon = -51.1°) = \pm 230$ mrad. The observed value was $\delta\Phi^{(0)} = \pm 290$ mrad ($\sigma_\Phi = 170$ mrad), leading to an error for the

† According to a smoothing algorithm derived from [7].

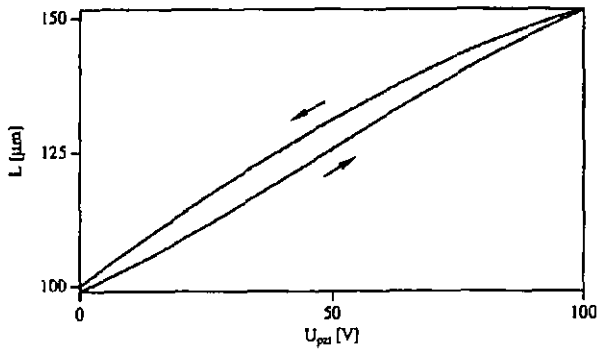

Figure 7. Absolute distance measurement in a range of $L = 125 \pm 25$ µm. $N = 57$ local phases Φ_n have been used to calculate the least squares fitted slope Φ' to calculate L.

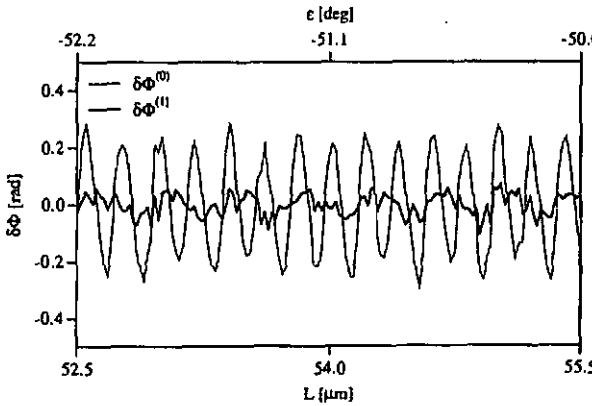

Figure 8. Phase evaluation error $\delta\Phi^{(0)}$ and corrected value $\delta\Phi^{(1)}$ after one iteration for a non-ideal phaseshift of $\Delta\Phi_x \approx 40°$, instead of 90°.

distance of $\delta L = \pm 20$ nm ($\sigma_L = 12$ nm). After one iteration for the phase correction, these errors were reduced to $\delta\Phi^{(1)} = \pm 90$ mrad ($\sigma_\Phi = 38$ mrad) and $\delta L = \pm 6$ nm ($\sigma_L = 3$ nm), respectively, which is an improvement by a factor 3.

7. Conclusions

White-light interferometry with spectral fringe detection is a simple and powerful method for absolute distance measurement in the millimetre range. The maximum operating distance is limited by the spectral resolution and the minimum distance by the spectral width of the source. Using an LED source ($\Delta\lambda \approx 80$ nm) and a simple diffraction grating (14 000 lines), the range of operation is from 8 µm to 1.9 mm. It has been shown that a minimum sampling concept for the fringe evaluation, based on four samples per period, leads to a simple and fast algorithm, which works for 2.5 to 10 samples per period with a phase accuracy of better than $\Delta\Phi = 0.1°$. The method has been experimentally demonstrated

for a working distance of 125 μm with an erating range from 50 μm to 150 μm. The resolution was found to be better than 3 nr The absence of any mechanical movement, minimum hardware requirement, minimum npling concept, and simple phase evaluation algorithm make this method particularly suit for fast distance control systems, for absolute distance measurement devices and for profil ietry.

References

[1] Tilford C R 1977 *Appl. Opt.* 16 1857

[2] Koch A and Ulrich R 1991 *Sensors Actuators* A 27 201

[3] Schwider J and Zhou L 1994 *Opt. Lett.* 19 995–7

[4] Creath K 1993 Temporal phase measurement thods *Interferogram Analysis, Digital Fringe Pattern Measurement Techniques* ed D W Robinson I G T Reid (Bristol: Institute of Physics Publishing) pp 94–140

[5] Born M and Wolf E 1993 *Principles of Optics* 6th In (Oxford: Pergamon) pp 401–13

[6] Dändliker R, Zimmermann E and Frosio G 1992 *t. Lett.* 17 679–81

[7] Marchand P and Marmet L 1983 *Rev. Sci. Instrur* 54 1034

Paper II

Dispersive white-light interferometry for absolute distance measurement with dielectric multilayer systems on the target

U. Schnell and R. Dändliker

Institute of Microtechnology, University of Neuchâtel, Breguet 2, CH-2000 Neuchâtel, Switzerland

S. Gray

Haltronic Technologies SA, Champs-Montants 12b, CH-2074 Marin, Switzerland

Received September 20, 1995

We have extended the use of a dispersive white-light interferometer for absolute distance measurement to include effects of dielectric multilayer systems on the target. The phase of the reflected wave changes as a function of wavelength and layer thickness and causes errors in the interferometric distance measurement. With dispersive white-light interferometry these effects can be measured *in situ*, and the correct mechanical distance can be determined. The effects of thin films deposited upon the target have been investigated for one and two layers (photoresist and SiO_2 upon Si). Experimental results show that the thicknesses of these layers can also be determined with an accuracy of the order of 10 nm. © 1996 Optical Society of America

Absolute distance measurement by optical interferometry is possible with either a multiple-wavelength[1] or a white-light[2–4] source. In any case, a measurement error occurs when interference effects of dielectric thin-film multilayer systems on the target object are not taken into account. This measurement error can be avoided when the parameters (e.g., layer thickness and index of refraction of each layer) of the multilayer stack are known. One can use different optical methods, based on ellipsometric,[5] photometric,[6–9] or interferometric[10] measurements, to determine the parameters of multilayer systems. We have used a dispersive white-light interferometer[4] first to characterize *in situ* the multilayer system on the target and then to determine the correct mechanical distance.

A schematic drawing of a dispersive white-light interferometer for absolute distance measurement between two surfaces is shown in Fig. 1. The beam of the white-light source is collimated by lens L_0. Lens L_1 focuses the beam onto the surface of the target object of the Fizeau interferometer. The interferometer is formed by one surface of prism P and the multilayer system. The distance L to be measured is the air gap between the reference surface of the prism and the top surface of the multilayer system. The output light of the interferometer passes through a diffraction grating (DG). The diffracted beam is then focused by lens L_2 onto a linear photodetector array (PDA). The interference phase $\Phi(\nu)$ as a function of optical frequency ν can be written as

$$\Phi(\nu) = (2\pi/c)2L\nu + \delta_r(\nu;\ d_m,\ n_m), \qquad (1)$$

where c is the speed of light and δ_r is the phase contribution on reflection on the multilayer system. To calculate δ_r it is assumed that the multilayer system is formed by M isotropic stratified planar layers. Each layer m is characterized by its thickness d_m and its complex index of refraction $n_m = n_{rm} - ik_m$, where n_{rm} is the real index of refraction, k_m is the extinction coefficient of medium m, and i is an imaginary unit. The complex amplitude reflection coefficient R of the multilayer system can be calculated by a 2×2 scattering matrix method.[5] The result is of the form

$$R = S_{21}/S_{11} = |R|\exp(i\delta_r), \qquad (2)$$

where S_{21} and S_{11} are two elements of the scattering matrix and δ_r is the observed phase shift on reflection to be introduced into Eq. (1). δ_r can be written as

$$\delta_r(\nu) = \frac{2\pi}{c}\left(\sum_{m=1}^{M} 2d_m n_m\right)\nu + f_{nl}(\nu;\ d_m,\ n_m), \qquad (3)$$

where the linear term on the right-hand side of Eq. (3) is due to the optical thickness of the multilayer stack and f_{nl} is a nonlinear function that describes the effects of multiple reflections within the stack. The basic idea of the method is to measure a sufficiently large number of interference phase values $\Phi_n(\nu)$ and then to determine the best values of the parameters L, d_m, and n_m in Eq. (1) by numerically fitting the calculated phase function $\Phi(\nu)$ from Eqs. (1)–(3) to the measured values $\Phi_n(\nu)$.

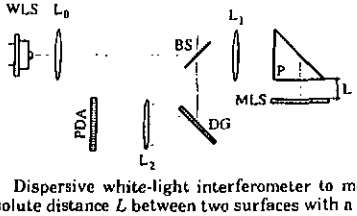

Fig. 1. Dispersive white-light interferometer to measure the absolute distance L between two surfaces with a dielectric multilayer system (MLS) on the object target: WLS, white-light source; BS, beam splitter.

0146-9592/96/070528-03$6.00/0

A dispersive white-light interference fringe pattern can be described as a function of optical frequency ν by

$$s(\nu) = A(\nu) + B(\nu)\cos\,\Phi(\nu), \tag{4}$$

where $A(\nu)$ and $B(\nu)$ are slowly varying functions of ν and $\Phi(\nu)$ is given by Eq. (1).

Following the optical arrangement shown in Fig. 1, dispersion of the DG introduces a frequency spacing $\Delta\nu$ between two adjacent pixels n and $n-1$ of the PDA, which results in a phase shift of

$$\Delta\Phi_s = \Phi_n - \Phi_{n-1} \approx \frac{4\pi}{c} L\Delta\nu. \tag{5}$$

where the phase contribution $\delta_s(\nu)$ of the multilayer system in Eq. (3) has been omitted. We then calculate the local phase Φ_n, using five adjacent samples of the interference signal symmetrically centered at sample s_n, through

$$S_n = s_{n-1} - s_{n+2} = 2B \sin\Delta\Phi_s \sin\Phi_n,$$

$$C_n = s_n - \frac{s_{n+2} + s_{n-1}}{2} = 2B \sin^2\Delta\Phi_s \cos\Phi_n,$$

$$\Phi_n = \tan^{-1}[S_n/C_n \sin\Delta\Phi_s], \tag{6}$$

where $1 \le n \le N$ and N is the number of measured local phases Φ_n. $A(\nu)$ and $B(\nu)$ are assumed locally constant. It has been shown that synchronized sampling with four samples per fringe period is an efficient and error-tolerant way to evaluate the phases from the interference pattern.[4] The optical arrangement of the DG, L_2, and the PDA in Fig. 1 is designed so that for the desired working distance L the frequency spacing $\Delta\nu$ between two adjacent pixels gives a phase shift of $\Delta\Phi_s \cong \pi/2$. We obtain the measured phase function $\Phi_n(\nu)$ by unwrapping the measured phase values Φ_n calculated from Eq. (6). When the number N of measured phase values Φ_n is larger than the number of parameters used for the calculated phase function $\Phi(\nu)$ in Eq. (1), the best values of the parameters L, d_m, and n_m are obtained by an appropriate least-squares algorithm to fit the calculated phase function $\Phi(\nu)$ to the measured phase values $\Phi_n(\nu)$.

The dispersive white-light interferometer for absolute distance measurement with dielectric multilayer systems on the target has been experimentally investigated with the help of the optical setup shown in Fig. 1. The light source was a halogen lamp (6 V, 20 W). The center wavelength of the spectrum detected by the PDA was $\lambda_0 = 632.8$ nm. After lens L_0 the beam was collimated with a diameter of approximately $D = 5$ mm. Uncoated optical fibers between the prism and the multilayer system introduced an approximate working distance of $L = 125$ μm. The DG had a spatial period of $g = 577.26$ nm, and the angle of incidence was $\theta_i = 33.2°$. The focal length of lens L_2 was 60 mm, and the linear PDA had 512 pixels with a center-to-center spacing of $\Delta x = 25$ μm. The line scan time was 26.5 ms. In this case we get a spectral resolution of the channeled spectrum of 0.2 nm/pixel (150 GHz/pixel), and a total spectral bandwidth of approximately 100 nm is detected by the PDA. For the working distance $L = 125$ μm we get a fringe spacing of 8 pixels. We obtained the synchronized samples s_n by adding the measured intensities of three adjacent pixels on the PDA, giving a phase step of $\Delta\Phi_s \cong \pi/2$. The number of considered local phases Φ_n was $N = 237$, calculated from the synchronized samples s_n through Eq. (6). Unwrapping of the local phases Φ_n delivered the measured phase function $\Phi_n(\nu)$.

A series of experiments for Si substrates with one layer (photoresist) or two layers (photoresist upon SiO_2) was performed. It was assumed that the refractive indices of the Si substrate ($n_{Si} = 3.85 - 0.02i$), the photoresist ($n_r = 1.644$), and silica ($n_{SiO_2} = 1.46$)

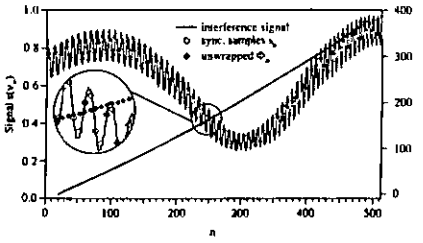

Fig. 2. Processing of the channeled spectrum: the observed interference signal $s(\nu)$ in the spectrum is synchronously detected with four samples per fringe period to calculate the fringe phases Φ_n. The variation of the average level of $s(\nu)$ is due to the change of $|R|$ in Eq. (2) as a function of ν.

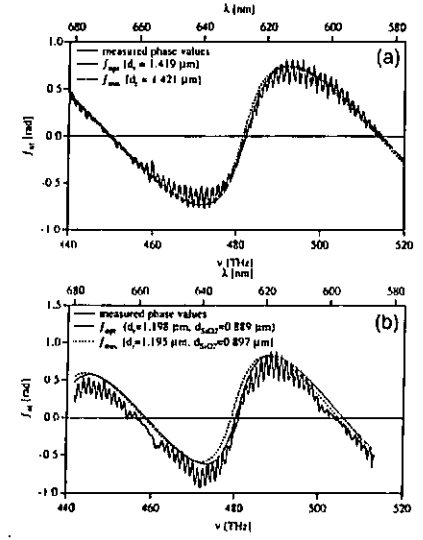

Fig. 3. (a) Comparison of measured and calculated nonlinear phase contribution f_{nl} versus optical frequency ν (wavelength λ) for photoresist (d_r) upon a Si substrate. (b) Comparison of measured and calculated nonlinear phase contribution f_{nl} versus optical frequency ν (wavelength λ) for photoresist (d_r) upon SiO_2 (d_{SiO_2}) upon a Si substrate.

Table 1. Comparison of Mechanical and Optical Measurements of Layer Thickness (d_r, Photoresist; d_{SiO_2}, SiO_2) and Measured Distance L without (L_{uc}) and with Correction (L_c) for Effects of the Thin Layers ($\Delta L = L_{uc} - L_c$)[a]

Photoresist upon Si Substrate					Photoresist upon SiO_2 upon Si Substrate			
d_r (μm)		L (μm)			d_r (μm)		d_{SiO_2} (μm)	
Mech.	Opt.	L_{uc}	L_c	ΔL	Mech.	Opt.	Mech.	Opt.
1.145	1.142	126.37	123.74	2.63	1.295	1.289	0.298	0.299
1.198	1.202	125.27	123.53	1.74	1.490	1.483	0.298	0.303
1.266	1.259	125.14	122.68	2.46	1.195	1.198	0.897	0.889
1.338	1.342	126.63	124.48	2.15	1.290	1.295	0.897	0.890
1.421	1.419	124.09	122.80	1.29	1.455	1.463	0.897	0.884

[a]Mech., mechanically determined; Opt., optically determined.

are known and independent of the optical frequency. Figure 2 shows a measured channeled spectrum interference signal $s(\nu)$, the synchronized samples s_n, and the unwrapped local phases Φ_n for one layer of photoresist of thickness $d_r \approx 1.42$ μm. Figure 3 shows experimental results obtained by fitting the theoretical phase function $\Phi(\nu)$ in Eqs. (1)–(3) to the measured phase function $\Phi_n(\nu)$ with a Levenberg–Marquardt least-squares algorithm.[11] This iterative method determines the maximum-likelihood estimate of parameters L and d_m that minimizes the figure-of-merit function χ^2, defined by

$$\chi^2 = \sum_{n=1}^{N} [\Phi_n(\nu) - \Phi(\nu;\ L,\ d_m)]^2 . \qquad (7)$$

The results of the fit, f_{opt}, after deduction of the linear parts of $\Phi(\nu)$ in Eqs. (1) and (3), are compared with the measured phase values. To verify the method we measured the thicknesses d_r of the photoresist and d_{SiO_2} of the silica with a mechanical profilometer with vertical resolution of $\Delta z \approx 5$ nm. The corresponding theoretical phase function $\Phi(\nu)$ was also calculated, and its nonlinear part is represented in Fig. 3 as f_{mec}. The differences between the measured values for the layer thicknesses were $\Delta d_r = 2$ nm for one layer (photoresist) and $\Delta d_r = 3$ nm and $\Delta d_{SiO_2} = 8$ nm for two layers (photoresist upon SiO_2).

More experimental results are listed in Table 1. A comparison of the optically and mechanically determined thicknesses shows for most samples an agreement of better than 10 nm. The effect of the photoresist layer on the absolute distance measurement is also shown in Table 1. We obtained the uncorrected value for the measured distance L_{uc}, neglecting the effects of the multilayer system, by fitting the theoretical phase function in Eq. (1) with $\delta_r = 0$ to the measured phase values $\Phi_n(\nu)$ with a linear least-squares algorithm. We obtained the corrected value for the measured distance L_c by fitting the theoretical phase function $\Phi(\nu)$ in Eqs. (1) and (3) to the measured phase function $\Phi_n(\nu)$ with the Levenberg–Marquardt least-squares algorithm, as described above. The difference $\Delta L = L_{uc} - L_c$ between uncorrected and corrected values is of the order of 1–3 μm. In addition, the results in Table 1 indicate that the error ΔL does not increase either linearly or monotonically with layer thickness d_r. This behavior can be explained by interference of the multiple reflections within the layer system.

In conclusion, we have demonstrated that dispersive white-light interferometry can be used efficiently to measure *in situ* the effects of thin films on a target object and to determine the correct mechanical distance to the top surface of the target. Experimental results for one and two layers (photoresist and SiO_2 upon Si) show that the thicknesses of these layers can be determined with an accuracy of the order of 10 nm (assuming that the refractive indices are known). Extension of the method to more than two layers with unknown refractive indices seems possible. Introduction of a more general model of the phase contribution of the multilayer system[12] could be used to measure multilayer structures with rough surfaces, interfaces, and finite substrates. The method presented can be readily integrated into profilometers and autofocusing systems based on white-light interferometry.

This research was supported by the Commission pour l'Encouragement de la Recherche Scientifique.

References

1. C. Polhemus, Appl. Opt. 12, 2071 (1973).
2. M. Davidson, K. Kaufman, K. Mazor, and F. Cohen, Proc. SPIE 775, 233–247 (1987).
3. J. Schwider and L. Zhou, Opt. Lett. 19, 995 (1994).
4. U. Schnell, E. Zimmermann, and R. Dändliker, Pure Appl. Opt. 4, 643 (1995).
5. R. M. A. Azzam and N. M. Bashara, *Ellipsometry and Polarized Light* (North-Holland, Amsterdam, 1987), pp. 153–416.
6. J. A. Dobrowolski, F. C. Ho, and A. Waldorf, Appl. Opt. 22, 3191 (1983).
7. K.-P. Koch, M. Maechler, and F. Glueck, Rev. Sci. Instrum. 56, 2243 (1985).
8. J. Mannhardt, T. Fuchs, and M. Mächler, Feinwerktechnik & Messtechnik 97, 269 (1989).
9. T. M. Merklein, Appl. Opt. 29, 505 (1990).
10. J. Schwider, Appl. Opt. 31, 6107 (1992).
11. Levenberg–Marquardt algorithm implemented in the MATLAB function *leastsq*, in *Optimization Toolbox for Use with MATLAB* (MathWorks, Natick, Mass., 1994).
12. C. L. Mitsas and D. I. Siapkas, Appl. Opt. 34, 1678 (1995).

Paper III

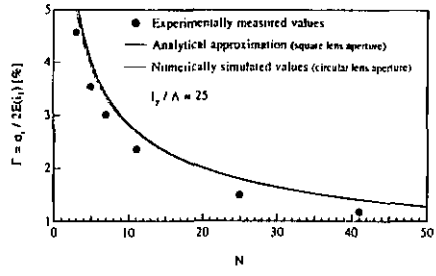

Fig. 11. Experimental investigation of the signal contrast Γ for comb photodetector arrays with $N = 3, 5, 7, 11, 25$, and 41 fingers ($l_y/\Lambda = 25$, $w/\Lambda = 0.25$, $\Lambda = 100\ \mu$m). The analytically calculated values and the values obtained from numerical integration are shown as solid and dotted curves, respectively.

$$\sigma_i^2 \approx E^2(I)Nl_y w^2 \Lambda\ \mathrm{sinc}^2(w/\Lambda). \tag{32}$$

An analytical approximation for the ratio Γ^2 is obtained by using the results in Eqs. (30) and (32),

$$\Gamma^2 = \frac{\sigma_i^2}{4E^2(i_1)} \approx \frac{1}{4}\frac{\Lambda}{Nl_y}\mathrm{sinc}^2(w/\Lambda), \tag{33}$$

where $E(i_1) + E(i_2) \approx 2E(i_1)$ is used. Note that N and the ratio l_y/Λ in Eq. (33) are the approximate numbers of uncorrelated speckle cells in the x and y directions, respectively, which are covered by the comb photodetector arrays and contribute to the measurement.

The signal contrast $\Gamma = \sigma_i/[E(i_1) + E(i_2)] = \sigma_i/2E(i_1)$ is readily found from Eq. (33). Figure 11 shows a plot of the signal contrast Γ versus the number of fingers N for $\Lambda = 100\ \mu$m, $l_y = 2500\ \mu$m, and $w = 25\ \mu$m. The values $\sigma_i/2E(i_1)$ obtained from the experimentally measured signals i and i_1 (32,000 samples) are shown as large solid dots for $N = 3, 5, 7, 11, 25$, and 41 fingers. To prove the validity of the analytical approximation in Eq. (33), we have numerically calculated the ratio Γ^2 according to Eqs. (29) and (31), using the power spectral density $\mathcal{P}_i$ in Eq. (9). The square root of the results (Γ) is represented in Fig. 11 by the dotted curve. Inspection of Fig. 11 shows that the simple analytical approximation in Eq. (33) can be used as a good estimation of the signal quality Γ^2 and the signal contrast Γ for a given detector geometry.

5. CONCLUSIONS

We have presented an optical method for noncontact detection of in-plane movement of a diffusing object based on spatial filtering of laser speckle patterns. Two periodic comb photodetector arrays connected differentially and matching of the speckle size with the period of the photodetector arrays produce a zero-offset, quasi-sinusoidal output signal. The movement can then be measured at arbitrarily low speed by zero-crossing detection of this signal. The direction of the movement can be detected with the help of a quadrature signal, which is produced by a second pair of interlaced comb photodetector arrays. First- and second-order statistical properties of the output signal have been investigated to determine the reliability and accuracy of the measurement. It turned out that the amplitude of the output signal is Rayleigh distributed, independent of the number and the length of the fingers of the comb photodetector arrays. However, the correlation length and phase accuracy of the signal are given by the number of fingers. Both the autocorrelation of the signal and the distribution of the measured phase difference for a given displacement have been calculated. The potential accuracy of displacement measurements has been analyzed. The result shows that the measured distance systematically overestimates the displacement and that the accuracy increases with the number of fingers. In addition, the signal quality has been investigated with respect to the geometry of the comb photodetector arrays. The experimental measurements are in good agreement with the theoretical results.

APPENDIX A

We start by introducing Eq. (13) into Eq. (14) and integrating over the spatial coordinate vector $\mathbf{x} = (x, y)$, which leads to

$$\hat{I}(\mathbf{p}) = \int \mathrm{d}^2x'\mathrm{d}^2x''\rho(\mathbf{x}')\rho^*(\mathbf{x}'')[\hat{h}(\mathbf{p})\exp(-j2\pi\mathbf{p}\mathbf{x}') \otimes \hat{h}^*(-\mathbf{p})\exp(-j2\pi\mathbf{p}\mathbf{x}'')]. \tag{A1}$$

Evaluating the convolution in Eq. (A1) yields

$$\hat{I}(\mathbf{p}) = \int \mathrm{d}^2p'\hat{h}(\mathbf{p}')\hat{h}^*(\mathbf{p}' - \mathbf{p})\hat{I}(\mathbf{p}) \times \int \mathrm{d}^2x'\mathrm{d}^2x''\rho(\mathbf{x}')\rho^*(\mathbf{x}'') \times \exp[-j2\pi\mathbf{p}'(\mathbf{x}' - \mathbf{x}'')]\exp(-j2\pi\mathbf{p}\mathbf{x}''). \tag{A2}$$

Equation (A2) is then rewritten as

$$\hat{I}(\mathbf{p}) = \int \mathrm{d}^2p'\hat{h}(\mathbf{p}')\hat{h}^*(\mathbf{p}' - \mathbf{p})\Gamma(\mathbf{p}', \mathbf{p}). \tag{A3}$$

Interest is turned to $\Gamma(\mathbf{p}', \mathbf{p})$ in Eq. (A3), which we express by the discrete sum

$$\Gamma(\mathbf{p}', \mathbf{p}) = \sum_{n_1,n} \exp[j(\varphi_{n_1} - \varphi_n)]\exp[-j2\pi\mathbf{p}'(\mathbf{x}_{n_1} - \mathbf{x}_n)] \times \exp(-j2\pi\mathbf{p}\mathbf{x}_n), \tag{A4}$$

where $a_k \exp(j\varphi_k)$ ($k = 1, 2, \ldots K$) are elementary phasor contributions from K different scattering regions of the diffusing object.[9] Equation (A4) can be separated in two sums, which gives

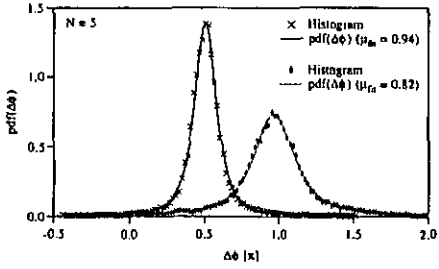

Fig. 8. Histogram of the phase difference $\Delta\phi$ for displacement $\Delta x = \Lambda/4$ and $\Lambda/2$ of the output signal i, obtained from 32,000 measured samples for $N = 5$. The best fitting probability density functions are shown as solid and dotted curves.

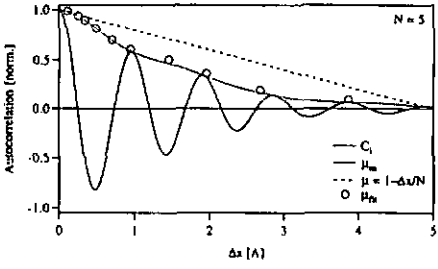

Fig. 9. Autocorrelation function C_i and correlation factor μ_m of the measured output signal i. The theoretical correlation factor μ is shown as dashed curve. Fitting the probability density function to the histograms of the phase difference $\Delta\phi$ yields the values μ_{fit} indicated by circles.

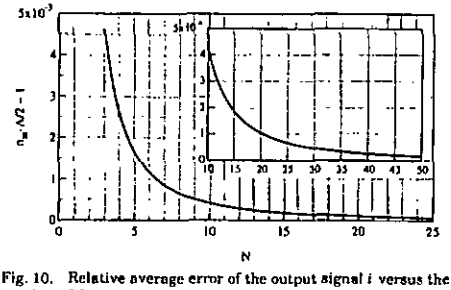

Fig. 10. Relative average error of the output signal i versus the number of fingers N.

lation factors μ and μ_m in Fig. 9 is due to spatial-frequency noise in the power spectral density of the measured output signal i, as can be seen by comparing the power spectral densities in Figs. 4(c) and 5. The histogram of the phase difference $\Delta\phi$ of the output signal i for various displacements Δx were calculated from 32,000 measured samples. The probability density function $pdf(\Delta\phi)$ in Eq. (26) was then fitted to the histograms. The values of the fit parameter μ_{fit} are indicated in Fig. 9 by circles. Note the good agreement between the values μ_{fit} and the measured correlation factor μ_m.

An ideally bandpass filtered signal whose spatial-frequency band extends from p_{min} to p_{max} has an average number of zeros per spatial coordinate unit given by[16]

$$n_{zc} = 2\left(\frac{1}{3}\,\frac{p_{max}^3 - p_{min}^3}{p_{max} - p_{min}}\right)^{1/2}. \tag{27}$$

If we introduce $p_{max} = p_0 + \delta p_x/2$ and $p_{min} = p_0 - \delta p_x/2$ in Eq. (27), where $p_0 = 1/\Lambda$ is the carrier spatial frequency and $\delta p_x = 1/l_x$ is the power equivalent width of the spectral bands [Fig. 4(c)], the average number of zero crossings n_{zc} per spatial period Λ of the output signal i is related to the number of fingers N through

$$n_{zc} = \frac{2}{\Lambda}\left[1 + \frac{(1/2N)^2}{3}\right]^{1/2} \cong \frac{2}{\Lambda}\left(1 + \frac{1}{24N^2}\right), \tag{28}$$

where $l_x = N\Lambda$ is used. A plot of the relative average error $n_{zc} \cdot \Lambda/2 - 1 \cong 1/24N^2$ versus N is shown in Fig. 10. The result is an important criterion for the accuracy of displacement measurements and shows that the measured distance d_m systematically overestimates the distance d by a factor of $1/24N^2$. Again, the result is valid under the assumption that no signal fading occurs. The use of the quadrature signal for direction-sensitive detection of the movement might eliminate this effect of the finite bandwidth of the spatial filter on the displacement measurement. A rigorous analysis remains to be done.

4. SIGNAL QUALITY

The signal quality is investigated with the help of the ratio $\Gamma^2 = \sigma_i^2/[E(i_1) + E(i_2)]^2$ of the variance σ_i^2 of the output signal i, which is proportional to the useful rms signal power, to the squared sum of the expectations of the signals i_1 and i_2 of the individual comb photodetector arrays $[E(i_1) + E(i_2)]^2$, which is proportional to the mean power responsible for the detection shot noise. $E^2(i_1)$ can be calculated by means of the power spectral density $\mathcal{G}_{i1}$ of the signal i_1 through

$$E^2(i_1) = \int_{-\infty}^{+\infty}\int_{-\infty}^{+\infty} dp_x dp_y \mathcal{G}_{i1}(p_x, p_y)\delta(p_x, p_y). \tag{29}$$

If we introduce into Eq. (29) for $\mathcal{G}_{i1}$ the result of multiplying Eqs. (4) and (9), the squared expectation of the signal i_1 becomes

$$E^2(i_1) = E^2(I)(Nwl_y)^2, \tag{30}$$

where $p_0 = 1/\Lambda$ and $l_x = N\Lambda$ are used. The variance of the output signal i is obtained from

$$\sigma_i^2 = \int_{-\infty}^{+\infty}\int_{-\infty}^{+\infty} dp_x dp_y \mathcal{G}_i(p_x, p_y)[1 - \delta(p_x, p_y)]. \tag{31}$$

For an analytical evaluation of Eq. (31), the circular diaphragm with diameter D of the imaging lens L in Fig. 1 is replaced by a square diaphragm with side length D. It can be shown (see Appendix C) that Eq. (31) then becomes approximately

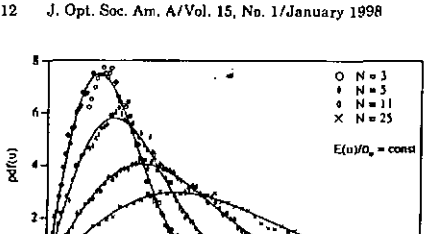

Fig. 7. Histogram of the amplitude u of the output signal i, obtained from 32,000 measured samples for $N = 3$, 5, 11, and 25 fingers. The best-fitting Rayleigh distributions are shown as solid curves.

C. Second-Order Statistics of the Output Signal

Important second-order statistical properties of the output signal i in Eq. (12) are the autocorrelation function and the probability density function of the phase difference $\Delta\phi$ for a displacement Δx. The latter can be used to characterize the accuracy of the measurement and to calculate the probability of an erroneous detection of reversed movement, when the quadrature signal i_q is used to determine the direction of the movement.

1. *Autocorrelation Function of the Output Signal*

The autocorrelation function C_i of the output signal i can be calculated with the help of the Wiener–Khinchin theorem,[11] which relates the autocorrelation function C_i to the power spectral density $\mathcal{S}_i$ through the Fourier transform $C_i(\Delta x, \Delta y) = FT^{-1}\{\mathcal{S}_i(p_x, p_y)\}$. With Eq. (11), the autocorrelation function in the x direction is found to be

$$C_i(\Delta x) = \mu(\Delta x)\cos(2\pi p_0 \Delta x), \tag{24}$$

where

$$\mu(\Delta x) = FT^{-1}\{\mathrm{sinc}^2(l_x p_x)\} = \begin{cases} 1 - \dfrac{|\Delta x|}{l_x} & |\Delta x| \le l_x \\ 0 & \text{otherwise} \end{cases} \tag{25}$$

is the (normalized) correlation factor of the output signal i. The correlation length l_c of output signal i is defined by the condition $\mu(l_c) = 0$. Using Eq. (25), this condition gives for the correlation length $l_c = l_x$.

2. *Probability Density Function of the Phase Difference*

The second-order joint probability density function of the phase of a speckle pattern intensity has been briefly discussed by Goodman.[9] The function can be adopted to describe the probability density function of the phase difference $\Delta\phi$ for a displacement Δx of the output signal i. The result is

$$pdf(\Delta\phi) = \frac{1-\mu^2}{2\pi(1-\beta^2)^{3/2}}\left(\beta \sin^{-1}\beta + \frac{\pi}{2}\beta + \sqrt{1-\beta^2}\right), \tag{26}$$

where $\beta = \mu\cos(\Delta\phi - \Delta\bar{\phi})$ and μ is the correlation factor given by Eq. (25). For the probability density function in Eq. (26) to be valid, the phase difference $\Delta\phi$ must be in the interval $\Delta\bar{\phi} \pm \pi$, where $\Delta\bar{\phi} = 2\pi/\Lambda \cdot \Delta x$ is the expected phase difference for a displacement Δx. As the correlation factor μ increases, the probability density function becomes more and more concentrated about $\Delta\bar{\phi}$, indicating that the output signal becomes more and more accurate.

As an example, the probability P_ϵ that the phase error of consecutive zero crossings for the displacement $\Delta x = \Lambda/2$ of the output signal i is smaller than $\epsilon\,(\epsilon < \pi)$ can be calculated by integrating Eq. (26) over the interval $\Delta\phi = \Delta\bar{\phi} \pm \epsilon$, with the correlation factor $\mu = 1 - 1/2N$ [Eq. (25)] and the expected phase difference $\Delta\bar{\phi} = \pi$. The result shows that the phase accuracy of the measurement is determined by the number of fingers N of the comb photodetector arrays. For example, the values of the probability that the phase difference $\Delta\phi$ is within the error interval $\epsilon = 0.1 \cdot \Delta\bar{\phi} = 18°$ are $P_\epsilon = 0.43$, 0.55, 0.71, 0.83, and 0.89 for $N = 3$, 5, 11, 25, and 41 fingers, respectively. For an error interval $\epsilon = 0.2 \cdot \Delta\bar{\phi} = 36°$, the values are $P_\epsilon = 0.69$, 0.79, 0.89, 0.95, and 0.97, respectively. When the quadrature signal i_q is used to determine the direction of the movement, the phase difference error of the output signal i for the displacement $\Delta x = \Lambda/4$ must be smaller than $|\epsilon| \le \pi/2$ if erroneous detection of reversed movement is to be avoided. Thus the reliability R_d of the detected direction can be calculated by integrating Eq. (26) over the interval $\Delta\phi = \Delta\bar{\phi} \pm \pi/2$, with the correlation factor $\mu = 1 - 1/4N$ [Eq. (25)] and the expected phase difference $\Delta\bar{\phi} = \pi/2$. For $N = 3$, 5, 11, 25, and 41 fingers, the values of the reliability are $R_d = 0.958$, 0.975, 0.989, 0.995, and 0.997, respectively. Note that the results of the above considerations are valid under the assumption that no signal fading occurs.

The second-order statistical properties of the output signal i was experimentally investigated. Figure 8 shows the histogram of phase difference $\Delta\phi$ for a displacement $\Delta x = \Lambda/4$ and $\Delta x = \Lambda/2$, obtained from 32,000 measured samples for $N = 5$ fingers. The expected phase differences are $\Delta\bar{\phi} = \pi/2$ and $\Delta\bar{\phi} = \pi$, respectively. The theoretical values of the correlation factor μ, obtained from Eq. (25), are $\mu(\Lambda/4) = 0.95$ and $\mu(\Lambda/2) = 0.90$. The best-fitting probability density functions $pdf(\Delta\phi)$ from Eq. (26) are also shown in Fig. 8. The values of the fit parameter are $\mu_{fit}(\Delta x = \Lambda/4) = 0.94$ and $\mu_{fit}(\Delta x = \Lambda/2) = 0.82$. The autocorrelation function C_i of the measured output signal i for $N = 5$ fingers is shown in Fig. 9 as solid curve. The correlation factor μ_m, which is the envelope function of C_i, is represented by the dotted curve. For comparison, the theoretical correlation factor μ from Eq. (25) is plotted as a dashed curve. The difference between the theoretical and the experimental corre-

can be investigated. $|\tilde{I}|$ and φ are the amplitude and the phase respectively of the complex Fourier transform $\tilde{I}$ at spatial frequency coordinate $\mathbf{p}$. j is the imaginary unit. Assuming that the complex amplitude of the speckle pattern obeys circular Gaussian statistics,[9,14] it can be shown (see Appendix A) that for any spatial frequency $\mathbf{p}$ the amplitude $|\tilde{I}|$ in Eq. (14) is Rayleigh distributed, namely,

$$pdf(|\tilde{I}(\mathbf{p})|) = \begin{cases} \dfrac{|\tilde{I}(\mathbf{p})|}{\kappa^2(\mathbf{p})} \exp\left[-\dfrac{|\tilde{I}(\mathbf{p})|^2}{2\kappa^2(\mathbf{p})}\right] & |\tilde{I}(\mathbf{p})| \geq 0 \\ 0 & \text{otherwise} \end{cases}, \tag{15}$$

and that the phase φ obeys the uniform distribution

$$pdf(\varphi) = \begin{cases} \dfrac{1}{2\pi} & -\pi \leq \varphi < \pi \\ 0 & \text{otherwise} \end{cases}. \tag{16}$$

The parameter κ of the Rayleigh distribution in Eq. (15) is a function of the spatial frequency $\mathbf{p}$ and depends on the autocorrelation function $C_{\hat{h}}$ of the Fourier transform $\hat{h}$ of the point-spread function h of the imaging system [Eq. (13)] through $\kappa(\mathbf{p}) = |C_{\hat{h}}(\mathbf{p})| \cdot \sigma$, where $2\sigma^2 = E(I)$. Mean η and variance χ^2 of the amplitude $|\tilde{I}|$ are then given by[14]

$$\eta(\mathbf{p}) = \sqrt{\pi/2}|C_{\hat{h}}(\mathbf{p})|\sigma, \tag{17}$$

$$\chi^2(\mathbf{p}) = (2 - \pi/2)|C_{\hat{h}}(\mathbf{p})|^2\sigma^2. \tag{18}$$

2. Autocorrelation Function of the Fourier Transform of the Speckle Pattern Intensity

The autocorrelation function $C_{\tilde{I}}$ of the Fourier transform $\tilde{I}$ of the speckle pattern intensity I is calculated through

$$C_{\tilde{I}}(\Delta\mathbf{p}) = E[\tilde{I}(\mathbf{p})\tilde{I}^*(\mathbf{p} - \Delta\mathbf{p})]. \tag{19}$$

Again, assuming that the complex amplitude of the speckle pattern obeys circular Gaussian statistics, it can be shown (see Appendix B) that Eq. (19) becomes

$$C_{\tilde{I}}(\Delta\mathbf{p}) = C_{\hat{h}}(\mathbf{p})C_{\hat{h}}(\Delta\mathbf{p} - \mathbf{p})\delta(\mathbf{p})\delta(\Delta\mathbf{p} - \mathbf{p}) + C_{|\hat{h}|^2}(\mathbf{p})\delta(\Delta\mathbf{p}). \tag{20}$$

The Dirac δ functions in Eq. (20) show that different spatial-frequency components of the Fourier transform of the speckle pattern intensity are uncorrelated; i.e., $C_{\tilde{I}}(\Delta\mathbf{p}) = 0, \forall \Delta\mathbf{p} \neq 0$.

In conclusion, it is stated that the amplitude $|\tilde{I}|$ of the complex Fourier transform $\tilde{I}$ of speckle pattern intensity I is Rayleigh distributed and the phase φ is uniformly distributed, independent of the spatial frequency coordinate $\mathbf{p}$, and that the Fourier transform components $\tilde{I}$ for different $\mathbf{p}$ are uncorrelated. To the best of our knowledge, this statement has not yet been published in the open literature.

B. First-Order Statistics of the Output Signal: Probability Density Function of the Amplitude

An important first-order statistical property of the output signal i in Eq. (12) is the probability density function of the amplitude u. It can be used to calculate the probability of signal fading, that is, the probability that the amplitude u is smaller than the minimum value $u_{\lim}$ for which zero-crossing can be reliably detected. The results in Eqs. (15) and (20) are used to determine the statistical properties of amplitude u and phase ϕ of the output signal i, which can be expressed by the Fourier transform

$$i(x) = FT^{-1}\{\tilde{I}(p_x)\tilde{s}(p_x)\}. \tag{21}$$

It has been stated that the Fourier transform $\tilde{I}$ of speckle pattern intensity I does *not* exist. Therefore, the output signal i cannot be calculated from Eq. (21). However, using Eqs. (5), (12), and (14), the Fourier transform in Eq. (21) can be written as

$$\begin{aligned} u(x)\cos(2\pi p_0 x + \phi(x)) &= FT^{-1}\{|\tilde{I}(p_x)|\exp[j\varphi(p_x)] \\ &\quad \times [\delta(p_x - p_0) + \delta(p_x + p_0)] \otimes \operatorname{sinc}(l_x p_x)\}, \end{aligned} \tag{22}$$

where the terms $(2p_0 l_x \omega)^2$, $\operatorname{sinc}^2(\omega p_x)$, and $l_y{}^2\operatorname{sinc}^2(l_y p_y)$ in Eq. (5) have been omitted for the sake of simplicity. We assume that the output signal i is a distribution-ergodic random process,[11] which means that space and ensemble averages are equal and interchangeable. Then, for the special case of an infinite width of the spatial filter s in the p_x direction [$\operatorname{sinc}(l_x p_x) = \delta(p_x)$ in Eq. (22)], Eq. (22) clearly reveals that amplitude u and phase ϕ of the output signal i obey the same statistics as amplitude $|\tilde{I}|$ and phase φ of the Fourier transform $\tilde{I}$ of the speckle pattern intensity I at spatial frequency $p_x = p_0$, i.e., the amplitude u is Rayleigh distributed, namely,

$$pdf(u) = \begin{cases} \dfrac{u}{\tau^2} \exp\left[-\dfrac{u^2}{2\tau^2}\right] & u \geq 0 \\ 0 & \text{otherwise} \end{cases}. \tag{23}$$

Mean $E(u)$ and variance $\sigma_u{}^2$ of the amplitude u are related to the parameter τ in Eq. (23) through $E(u) = \sqrt{\pi/2} \cdot \tau$ and $\sigma_u{}^2 = (2 - \pi/2) \cdot \tau^2$. In the general case of a finite width of the spatial filter s in the p_x direction [finite spectral bandwidth Δp_x in Eq. (5) and in Fig. 4(a)], averaging of sums of uncorrelated pairs of inverse Fourier transform components at spatial frequencies $p_x = p_0 \pm \partial p_x$ (∂p_x within the bandwidth Δp_x) shows that the result in Eq. (23) is still valid.

This result has been experimentally demonstrated. The histograms of amplitude u of output signal i, obtained from 32,000 measured samples for $N = 3$, 5, 11, and 25 fingers, are shown in Fig. 7. The best-fitting Rayleigh distributions, according to Eq. (23), are also shown in Fig. 7 by solid curves. The mean value $E(u)$ of amplitude u is proportional to $\sqrt{N}$ and $\sqrt{I_y}$, whereas the ratio $\sigma_u/E(u)$ of the standard deviation σ_u to $E(u)$ is invariant with respect to N and I_y.

The Rayleigh distribution of amplitude u in Eq. (23) implies that signal fading cannot be excluded, because the probability for amplitudes smaller than any arbitrary low amplitude $u_{\lim}$ never reaches zero [$P(u < u_{\lim}) \neq 0$, $\forall u_{\lim}$]. These findings give significant criteria for the reliability of the measurement.

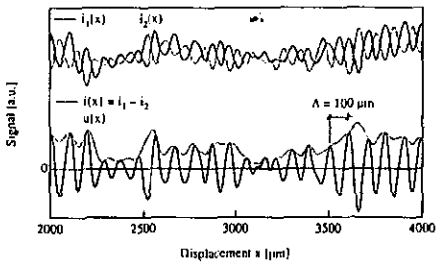

Fig. 5. Typical measured signals $i_1(x)$ and $i_2(x)$ in phase opposition for $N = 5$ fingers. The zero-offset, quasi-sinusoidal output signal $i(x)$ is calculated through $i = i_1 - i_2$. The amplitude $u(x)$ is the envelope function of the output signal $i(x)$.

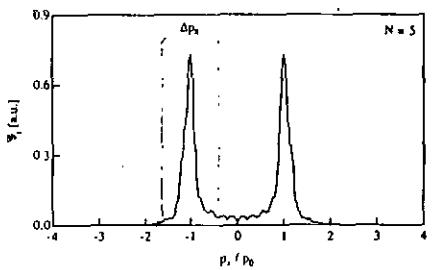

Fig. 6. Power spectral density $\mathcal{S}_i(p_x, 0)$ of the experimentally measured output signal $i(x)$ in Fig. 5. The spectral bandwidth Δp_x is indicated for comparison with Fig. 4(a).

$$\mathcal{S}_i(p_x, p_y) = \mathcal{S}_i(p_x, p_y)(2p_0 l_x w)^2 \times [\delta(p_x - p_0) + \delta(p_x + p_0)] \times \mathrm{sinc}^2(wp_x) \otimes \mathrm{sinc}^2(l_x p_x) \times l_y^2 \mathrm{sinc}^2(l_y p_y), \quad (11)$$

as shown in Fig. 4(c) for $p_y = 0$. A typical zero-offset, quasi-sinusoidal output signal i, with the power spectral density described in Eq. (11), is shown in Fig. 3. The signal can be described by

$$i(x) = u(x)\cos[2\pi p_0 x + \phi(x)], \quad (12)$$

where $u(x)$ and $\phi(x)$ are the statistical amplitude and phase, respectively.

E. Experimental Investigation of Spatial Filtering

The concept of spatial filtering of laser speckle patterns for detection of movement was experimentally investigated with the help of the setup shown in Fig. 1. The light source was a He–Ne laser working at $\lambda = 633$ nm. The diffusing object was a Marata plate (Spindler & Hoyer) mounted on a stepper motor with a linear step increment of $\Delta x_{step} = 2.5\ \mu$m. The imaging lens L had a focal length $f = 50$ mm. The aperture was limited by a circular diaphragm with diameter $D = 1.267$ mm. The distance between lens L and the image (object) plane was $d_I(d_O) = 100$ mm. The magnification factor of the imaging system was $m = d_I/d_O = 1$. From Eq. (8), the average speckle size is $\Delta x_s = 63.6\ \mu$m, which gives a cut-off spatial frequency of $p_m = 0.02\ \mu\mathrm{m}^{-1}$ in Eq. (10). A linear photodiode array of 512 pixels with center-to-center spacing of $\Delta x_c = 25\ \mu$m was used to detect the movement of the speckle pattern. The pixel width and length were $w = 25\ \mu$m and $l_y = 2.5$ mm, respectively. The signal i_1 was obtained by adding the measured intensities of N pixels on the photodiode array, spaced by $\Lambda = 100\ \mu$m (4 pixels), to emulate a comb photodetector array with spatial frequency $p_0 = 1/\Lambda = 0.01\ \mu\mathrm{m}^{-1}$. Addition of the intensities of N pixels shifted by $\Lambda/2 = 50\ \mu$m (2 pixels) delivered the signal i_2 in phase opposition with respect to i_1. The differential output signal i was then obtained from $i = i_1 - i_2$. Typical measured signals i_1, i_2, and i versus displacement x are shown in Fig. 5 for $N = 5$ fingers. The amplitude u of the output signal i in Eq. (12) was calculated from $u = \{i^2 + \mathcal{H}^2(i)\}^{1/2}$, where $\mathcal{H}(i)$ is the Hilbert transform[12] of i. The power spectral density $\mathcal{S}_i$ of the signal i was obtained through $\mathcal{S}_i(p_x) = |FT\{i(x)\}|^2$, where $FT\{\cdot\}$ stands for the Fourier transform of $(\cdot)$. The result is shown in Fig. 6. The spectral bandwidth $\Delta p_x = 6/l_y$ is also indicated in Fig. 6 for comparison with Fig. 4(a).

3. STATISTICAL PROPERTIES OF THE OUTPUT SIGNAL

The statistical properties of amplitude u and phase ϕ of output signal i in Eq. (12) and Fig. 5 are investigated to characterize reliability and accuracy of the measurement. First the probability density function and the autocorrelation function of the complex Fourier transform of the speckle pattern intensity are determined. Then the statistical properties of the Fourier transform of the filtered output signal i and of the signal itself are calculated.

A. Statistical Properties of the Fourier Transform of the Speckle Pattern Intensity

1. Probability Density Function of the Fourier Transform of the Speckle Pattern Intensity

The speckle pattern intensity I in the image plane in Fig. 1 can be described by the two-dimensional convolution integral

$$I(\mathbf{x}) = \int \mathrm{d}^2x'\,\mathrm{d}^2x''\rho(\mathbf{x}')\rho^*(\mathbf{x}'')h(\mathbf{x} - \mathbf{x}')h^*(\mathbf{x} - \mathbf{x}''), \quad (13)$$

where ρ describes the roughness of the diffusing object, h is the impulse response (point-spread function) of the imaging system,[9] and $\mathbf{x}'$, $\mathbf{x}''$ are spatial coordinate vectors in the object plane. $\langle\cdot\rangle^*$ stands for the complex conjugate of $\langle\cdot\rangle$. In general, the Fourier transform of a random process, as the speckle pattern intensity I in Eq. (13), does *not* exist.[13] Nevertheless, the statistical properties of the Fourier transform of the speckle pattern intensity

$$\hat{I}(\mathbf{p}) = |\hat{I}(\mathbf{p})|\exp[j\varphi(\mathbf{p})] = \int \mathrm{d}^2x I(\mathbf{x})\exp(-j2\pi\mathbf{px}), \quad (14)$$

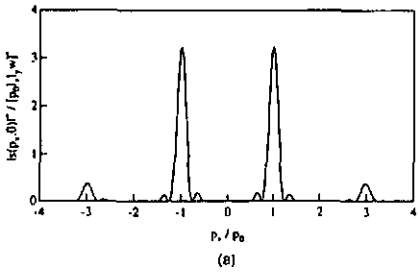

(a)

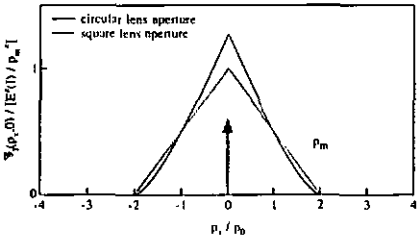

(b)

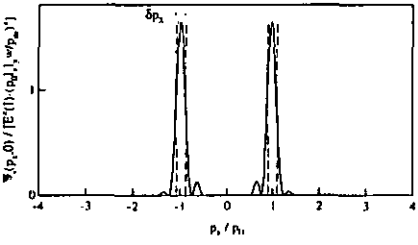

(c)

g. 4. (a) Transfer function $|\tilde{s}(p_x, 0)|^2$ of the photodetector, hich is shown in Fig. 3, for the case of $w = \Lambda/4$ and $l_x = 5\Lambda$.) Power spectral density $\mathcal{S}_I(p_x, 0)$ of the speckle pattern intenty in the image plane in the case of a circular (solid curve) and square (dashed curve) lens aperture. The cut-off spatial freiency p_m is related to the speckle size Δx_s through $p_m = 4/\pi\Delta x_s$ (circular lens aperture). (c) Power spectral density $(p_x, 0)$ of the zero-offset, quasi-sinusoidal output signal.

$$|\tilde{s}(p_x, p_y)|^2 = |\tilde{s}_1 - \tilde{s}_2|^2$$

$$= (2p_0 l_x w)^2 \left\{ \sum_{k=-\infty}^{+\infty} \delta[p_x - (2k+1)p_0] \times \operatorname{sinc}^2(w p_x) \right\} \otimes \operatorname{sinc}^2(l_x p_x) \times l_y^2 \operatorname{sinc}^2(l_y p_y). \quad (5)$$

plot of the transfer function $|\tilde{s}(p_x, 0)|^2$ is shown in Fig. a) for $w = \Lambda/4$ and $l_x = 5\Lambda$. A second interlaced pair differentially connected comb photodetector arrays s_{1q} nd s_{2q}, shifted by $\Delta x = \Lambda/4$ with respect to s_1 and s_2 (Fig. 3), produces a signal i_q in quadrature to the signal i. The signals i and i_q then permit measurement of the movement and its direction without ambiguity and at arbitrarily low speed.

C. Minimum Number of Fingers

The width of the spatial filter in the p_x direction is given by overall length l_x of the comb photodetector arrays. A minimum number of fingers $N_{\min}$ is required to avoid overlapping of adjacent spectral bands in the transfer function $|\tilde{s}|^2$ of Eq. (5). This condition can be written as

$$(2k+1)p_0 + \tfrac{1}{2}\Delta p_x \le [2(k+1)+1]p_0 - \tfrac{1}{2}\Delta p_x, \quad (6)$$

where Δp_x is the width of the spectral bands [Fig. 4(a)]. If we assume a bandwidth of $\Delta p_x = 6/l_x$, neglecting the sidelobes beyond Δp_x, we cover 96.7% of the spectral content of the bands. If we introduce $p_0 = 1/\Lambda$ and $l_x = N\Lambda$ in Eq. (6), the minimum number of fingers $N_{\min}$ of the individual comb photodetector arrays is then

$$N_{\min} = 3. \quad (7)$$

D. Power Spectral Density of the Input Signal

In the case of a circular lens aperture with diameter D, the average speckle size Δx_s in the image plane is related to the parameters of the optical systems through

$$\Delta x_s = \frac{4}{\pi}\frac{\lambda d_I}{D}. \quad (8)$$

The power spectral density $\mathcal{S}_I$ of the speckle pattern intensity I has circular symmetry and is given by[9]

$$\mathcal{S}_I(p_x, p_y) = E^2(I)\left\{ \delta(p_x, p_y) + \frac{8}{p_m^2 \pi^2} \times \left\{ \cos^{-1}\left(\frac{\rho}{p_m}\right) - \frac{\rho}{p_m}\sqrt{1 - \left(\frac{\rho}{p_m}\right)^2} \right\} \right\}, \quad (9)$$

where $\rho = (p_x^2 + p_y^2)^{1/2}$ and $E(\cdot)$ is the statistical expectation of $(\cdot)$. p_m is the cut-off spatial frequency, which is related to the speckle size Δx_s in Eq. (8) through

$$p_m = D/\lambda d_I = 4/\pi\Delta x_s. \quad (10)$$

A plot of the power spectral density $\mathcal{S}_I(p_x, 0)$ in Eq. (9) is shown in Fig. 4(b).

E. Power Spectral Density of the Output Signal

By appropriate choice of the speckle size Δx_s in Eq. (8) and the spatial period Λ of the comb photodetector arrays, all spectral bands except those centered at spatial frequencies $p_x = \pm p_0$ can be eliminated in the power spectral density $\mathcal{S}_i$ of the output signal i. An appropriate choice is $\Delta x_s = 2\Lambda/\pi$, which gives $p_m = 2p_0$ for the cut-off spatial frequency in Eq. (10), as shown in Fig. 4(b). The power spectral density of the output signal i can then be written as

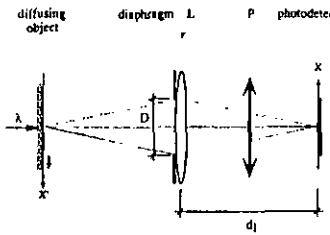

Fig. 1. Optical setup for detection of in-plane movement of a diffusing object with laser speckle patterns.

$$\mathcal{S}_i(p_x, p_y) = \mathcal{S}_I(p_x, p_y)|\hat{s}(p_x, p_y)|^2, \tag{2}$$

where $\mathcal{S}_I$ is the power spectral density of the speckle pattern intensity I; $|\hat{s}|^2$ is the squared modulus of the transfer function (called transfer function in the following) of the spatial filter s; and p_x and p_y are spatial-frequency coordinates according to spatial coordinates x and y, respectively. $\hat{(\cdot)}$ stands for the Fourier transform of $(\cdot)$. Thus the power spectral density of the output random process (output signal i) is simply the product of the transfer function of the spatial filter (photodetector s) and the power spectral density of the input random process (speckle pattern intensity I).

A. One-Dimensional Detection of Movement

Interest is turned to the detection of one-dimensional in-plane movement, when the object is moving along the x axis. If the transfer function $|\hat{s}|^2$ of the spatial filter in Eq. (2) has sharp peaks at spatial frequencies $p_x = \pm p_0$, the power spectral density $\mathcal{S}_i$ of output signal i also has sharp peaks at the same spatial frequencies. Output signal i versus displacement x is then zero-offset, quasi-sinusoidal with spatial period $\Lambda = 1/p_0$. A typical output signal i versus displacement x is shown in Fig. 2. Movement at arbitrarily low speed can be measured by zero-crossing detection of this signal.

B. Comb Array Detector for Spatial Filtering

A photodetector geometry for spatial filtering with sharp peaks at spatial frequencies $p_x = \pm p_0$ in the transfer function is shown in Fig. 3. The detector is composed of two interlaced comb photodetector arrays connected differentially. Each array has N fingers of width w and length l_y. The finger spacing is Λ, and the overall detector length is $l_x = N\Lambda$. The aperture functions s_1 and s_2 of the comb photodetector arrays, which are shifted by $\Delta x = \Lambda/2$, can be written as

$$s_1(x, y) = \left\{\sum_{k=-\infty}^{+\infty} \delta(x - k\Lambda) \otimes \mathrm{rect}(x/w)\right\} \times \mathrm{rect}(x/l_x) \times \mathrm{rect}(y/l_y), \quad k \in \mathbb{Z}$$

$$s_2(x, y) = s_1(x - \Lambda/2, y). \tag{3}$$

$\delta(x)$ is a one-dimensional Dirac delta function, and $\mathrm{rect}(x/a) = 1$ for $|x/a| \le 1/2$, zero otherwise. The transfer function of the comb photodetector array s_1 is then

$$|\hat{s}_1(p_x, p_y)|^2 = (p_0 l_x w)^2 \times \left[\sum_{k=-\infty}^{+\infty} \delta(p_x - kp_0)\,\mathrm{sinc}^2(wp_x)\right] \otimes \mathrm{sinc}^2(l_x p_x) \times l_y^2 \mathrm{sinc}^2(l_y p_y), \tag{4}$$

with $p_0 = 1/\Lambda$ and $\mathrm{sinc}(x) = \sin(\pi x)/(\pi x)$. Differential connection of comb photodetector arrays s_1 and s_2 eliminates the spatial-frequency components, centered at $p_x = 2kp_0$, in the transfer function of the individual comb photodetector arrays in Eq. (4). The transfer function of the spatial filter can then be written as

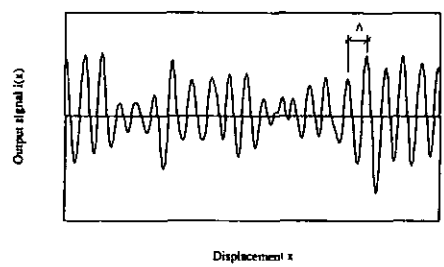

Fig. 2. Typical zero-offset, quasi-sinusoidal output signal with spatial period $\Lambda = 1/p_0$.

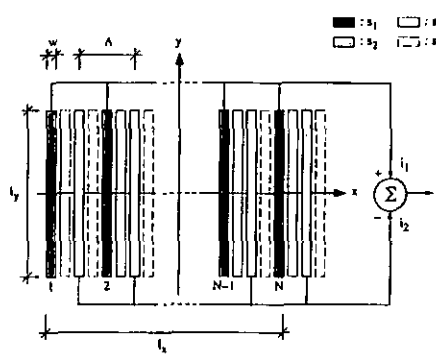

Fig. 3. Possible photodetector geometry for spatial filtering with sharp peaks at spatial frequencies $p_x = \pm 1/\Lambda$ in the transfer function. The photodetector is composed of two comb photodetector arrays s_1 and s_2 connected differentially. Each array has N fingers of width w and length l_y. The overall detector length is $l_x = N\Lambda$. A second pair of comb photodetector arrays s_{1q} and s_{2q} can be interlaced to detect the direction of the movement.

Detection of movement with laser speckle patterns: statistical properties

U. Schnell, J. Piot, and R. Dändliker

Institute of Microtechnology, University of Neuchâtel, Breguet 2, CH-2000 Neuchâtel, Switzerland

Received May 5, 1997; revised manuscript received August 11, 1997; accepted September 2, 1997

We present an optical method for detection of in-plane movement of a diffusing object. The technique is based on spatial filtering of the laser speckle pattern, which is produced by illumination of the object with coherent light. Two interlaced differential comb photodetector arrays act as a periodic filter to the spatial-frequency spectrum of the speckle pattern intensity. The detector produces a zero-offset, periodic output signal versus displacement that permits measurement of the movement at arbitrarily low speed. The direction of the movement can be detected with the help of the quadrature signal, which is produced by a second pair of interlaced comb photodetector arrays. When speckle size and period of the comb photodetector arrays are matched, the output signal versus displacement is quasi-sinusoidal with statistical amplitude and phase. First- and second-order statistics of the signal are investigated. First the probability density function and the autocorrelation function of the complex Fourier transform of the speckle pattern intensity are determined. Then the statistical properties of the spectrum of the filtered signal and of the signal itself are calculated. It turns out that the amplitude of the signal is Rayleigh distributed. Both the autocorrelation function of the signal and the probability density function of the measured phase difference for a given displacement are calculated. The potential accuracy of displacement measurements is analyzed. In addition, the signal quality is investigated with respect to the geometry of the detector. The theoretical results are experimentally verified.
 [S0740-3232(98)02801-4]
OCIS codes: 030.6140, 030.6600, 330.4150.

. INTRODUCTION

'he dynamic behavior of laser speckle patterns, caused by ı-plane motion of a diffusing object under illumination ·ith coherent light, has been used in many applications › measure the displacement and velocity of moving ob- ·ects. The relation between speckle pattern variation nd object movement has been investigated in detail.[1,2] everal techniques for detection of movement with laser peckle patterns have been reported. The methods are nsed on speckle pattern correlation measurement,[3] first- rder-statistics measurement of speckle pattern intensity ariation,[4] zero-crossing measurement for the intensity uctuation of spatially integrated laser speckle patterns,[5] r spatial filtering of laser speckle patterns.[6,7] A laser peckle pattern velocimeter using a periodic differential tector has been published by Ogiwara *et al.*[8]

In this paper we present a method for detection of ıovement (displacement) rather than velocity of the ob- ·ct, based on spatial filtering of the laser speckle pattern. wo interlaced differential comb photodetector arrays nd optical matching between the speckle size and the ımb detector period produce a zero-offset, quasi- nusoidal output signal versus displacement. The sta- stical properties of amplitude and phase of the signal ·e investigated to characterize reliability and accuracy of ıe measurement. The signal quality is characterized by ıe ratio between the rms power of the output signal and ıe mean power detected by the individual comb photode- ·tor arrays. This ratio is investigated with respect to ıe geometry of the detector.

2. SPATIAL FILTERING

The basic setup for detection of in-plane movement, based on spatial filtering of laser speckle patterns, is shown in Fig. 1. The collimated coherent light beam at optical wavelength λ illuminates the diffusing object moving in a plane perpendicular to the optical axis. Lens L images the object in the image plane at distance d_I. The aperture of the lens is limited by a diaphragm with diameter D. A linearly polarized speckle pattern is obtained with the help of polarizer P. The static and dynamic properties of the speckle pattern in the image plane are well established.[1,2,9,10] The photodetector in the image plane produces an output signal i (measured optical power), which can be described by the two-dimensional convolution integral

$$i(x, y) = \int_{-\infty}^{+\infty}\int_{-\infty}^{+\infty} d\xi d\eta I(\xi, \eta)s(\xi - x, \eta - y)$$

$$= I(x, y) \otimes s(x, y), \qquad (1)$$

where $I(x, y)$ is the speckle pattern intensity in the image plane, $s(x, y)$ is the aperture function of the photodetector, and (x, y) and (ξ, η) are spatial coordinates in the detection plane. The convolution integral in Eq. (1) reveals that the photodetector performs a linear (spatial) filtering of the speckle pattern intensity I. Linear filtering of a random process—the speckle pattern intensity—can best be investigated with the concept of power spectral density.[11] The power spectral density $\mathcal{G}_i$ of output signal i in Eq. (1) can be written as

$$\Gamma(\mathbf{p}', \mathbf{p}) = \sum_{m=n} a_n^2 \exp(-j2\pi\mathbf{p}\mathbf{x}_n) + \sum_{m\neq n} a_m a_n \exp[j(\varphi_m - \varphi_n)] \times \exp[-j2\pi\mathbf{p}'(\mathbf{x}_m - \mathbf{x}_n)] \times \exp(-j2\pi\mathbf{p}\mathbf{x}_n) \quad \text{(A5a)}$$

$$= K\alpha^2\delta(\mathbf{p}) + \alpha(\mathbf{p}', \mathbf{p}). \quad \text{(A5b)}$$

We assume that the pure phase contributions $\exp[-j2\pi\mathbf{p}'(\mathbf{x}_m - \mathbf{x}_n)]$ and $\exp(-j2\pi\mathbf{p}\mathbf{x}_n)$ in Eq. (A5a) do not change the statistical properties of the random variable $\alpha = |\alpha| \cdot \exp(j\varphi_\alpha)$ in Eq. (A5b). Invoking the central limit theorem[16] shows that the random variable $|\alpha|^2$ obeys a negative exponential distribution, which is

$$\mathrm{pdf}(|\alpha|^2) = \begin{cases} \dfrac{1}{2\sigma^2}\exp\left(-\dfrac{|\alpha|^2}{2\sigma^2}\right) & |\alpha|^2 \geq 0 \\ 0 & \text{otherwise} \end{cases}, \quad \text{(A6)}$$

and that the phase φ_α obeys a uniform distribution. Equations (A3) and (A5b) reveal that the Fourier transform $\hat{I}$ of the speckle pattern intensity I depends linearly on the random variable α. Therefore the squared modulus $|\hat{I}|^2$ and the phase φ of $\hat{I}$ still obey negative exponential and uniform statistics, respectively.[17] A change of variable finally shows that amplitude $|\hat{I}|$ and phase φ in Eq. (14) obey Rayleigh and uniform distributions, leading to the results in Eqs. (15) and (16).

APPENDIX B

With introduction of Eq. (A2), Eq. (19) becomes

$$C_{\hat{I}}(\Delta\mathbf{p}) = E\Big\{\int \mathrm{d}^2p'\mathrm{d}^2x'\mathrm{d}^2x'' \times \hat{h}(\mathbf{p}')\hat{h}^*(\mathbf{p}' - \mathbf{p})\rho(\mathbf{x}')\rho^*(\mathbf{x}'') \times \exp[-j2\pi\mathbf{p}'(\mathbf{x}' - \mathbf{x}'')] \times \exp(-j2\pi\mathbf{p}\mathbf{x}'')\int \mathrm{d}^2p''\mathrm{d}^2x'''\mathrm{d}^2x'''' \times \hat{h}^*(\mathbf{p}'')\hat{h}(\mathbf{p}'' - \mathbf{p} + \Delta\mathbf{p})\rho^*(\mathbf{x}''')\rho(\mathbf{x}'''') \times \exp[j2\pi\mathbf{p}''(\mathbf{x}''' - \mathbf{x}'''')] \times \exp[j2\pi(\mathbf{p} - \Delta\mathbf{p})\mathbf{x}'''']\Big\}. \quad \text{(B1)}$$

Changing the order of spatial averaging and integration in Eq. (B1) gives

$$C_{\hat{I}}(\Delta\mathbf{p}) = \int \mathrm{d}^2p'\mathrm{d}^2p''\mathrm{d}^2x'\mathrm{d}^2x''\mathrm{d}^2x'''\mathrm{d}^2x'''' \times \hat{H}(\mathbf{p}, \mathbf{p}', \mathbf{p}'', \Delta\mathbf{p})E[\rho(\mathbf{x}')\rho^*(\mathbf{x}'') \times \rho^*(\mathbf{x}''')\rho(\mathbf{x}'''')]\exp(-j\psi), \quad \text{(B2)}$$

where

$$\hat{H}(\mathbf{p}, \mathbf{p}', \mathbf{p}'', \Delta\mathbf{p}) = \hat{h}(\mathbf{p}')\hat{h}^*(\mathbf{p}' - \mathbf{p})\hat{h}^*(\mathbf{p}'') \times \hat{h}(\mathbf{p}'' - \mathbf{p} + \Delta\mathbf{p}) \quad \text{(B3)}$$

and the phase term in Eq. (B2) is

$$\Psi = 2\pi[\mathbf{p}\mathbf{x}'' + \mathbf{p}'(\mathbf{x}' - \mathbf{x}'') - (\mathbf{p} - \Delta\mathbf{p})\mathbf{x}'''' - \mathbf{p}''(\mathbf{x}'''' - \mathbf{x}''')]. \quad \text{(B4)}$$

Assuming that the elementary phasor contributions $a_k \exp(j\varphi_k)$ of the diffusing object are statistically independent of each other, the spatial averaging in Eq. (B2) reduces to[18,19]

$$E[\rho(\mathbf{x}')\rho^*(\mathbf{x}'')\rho^*(\mathbf{x}'''')\rho(\mathbf{x}''')] = \delta(\mathbf{x}' - \mathbf{x}'')\delta(\mathbf{x}''' - \mathbf{x}'''') + \delta(\mathbf{x}' - \mathbf{x}''')\delta(\mathbf{x}'' - \mathbf{x}''''). \quad \text{(B5)}$$

Introducing Eq. (B5) into Eq. (B2) yields

$$C_{\hat{I}}(\Delta\mathbf{p}) = \int \mathrm{d}^2p'\mathrm{d}^2p''\mathrm{d}^2x'\mathrm{d}^2x'''\hat{H}(\mathbf{p}, \mathbf{p}', \mathbf{p}'', \Delta\mathbf{p}) \times \exp(-j2\pi\mathbf{p}\mathbf{x}')\exp[j2\pi(\mathbf{p} - \Delta\mathbf{p})\mathbf{x}'''] + \int \mathrm{d}^2p'\mathrm{d}^2p''\mathrm{d}^2x'\mathrm{d}^2x''\tilde{H}(\mathbf{p}, \mathbf{p}', \mathbf{p}'', \Delta\mathbf{p}) \times \exp(-j2\pi\Delta\mathbf{p}\mathbf{x}'') \times \exp[-j2\pi(\mathbf{p}' - \mathbf{p}'')(\mathbf{x}' - \mathbf{x}'')]. \quad \text{(B6)}$$

Integrating Eq. (B6) over the spatial coordinates (x', y'), (x'', y''), and (x''', y''') yields

$$C_{\hat{I}}(\Delta\mathbf{p}) = \int \mathrm{d}^2p'\mathrm{d}^2p''\hat{H}(\mathbf{p}, \mathbf{p}', \mathbf{p}'', \Delta\mathbf{p})\delta(\mathbf{p})\delta(\Delta\mathbf{p} - \mathbf{p}) + \int \mathrm{d}^2p'\mathrm{d}^2p''\tilde{H}(\mathbf{p}, \mathbf{p}', \mathbf{p}'', \Delta\mathbf{p})\delta(\Delta\mathbf{p}) \times \delta(\mathbf{p}' - \mathbf{p}''). \quad \text{(B7)}$$

Finally, introducing Eq. (B3) and integrating Eq. (B7) over the spatial frequency coordinates (p_x', p_y') and (p_x'', p_y'') leads to the result in Eq. (20).

APPENDIX C

For a square lens diaphragm with side length D, the power spectral density $\mathcal{S}_I$ of the speckle pattern intensity I has Cartesian symmetry and is given in the $p_{x(y)}$ direction by[9]

$$\mathcal{S}_I(p_{x(y)}) = E^2[I_{x(y)}]\left\{\delta[p_{x(y)}] + \frac{1}{p_m}T\left[\frac{p_{x(y)}}{p_m}\right]\right\}, \quad \text{(C1)}$$

where $T(x/a) = 1 - |x/a|$ for $|x/a| \leq 1$, zero otherwise, and $E^2(I) = E^2(I_x)E^2(I_y)$. A plot of $\mathcal{S}_I(p_x, 0)$ is shown in Fig. 4(b) as a dotted curve. Separation of spatial-frequency coordinates p_x and p_y in Eq. (29) then leads to

$$\sigma_i^2 = \sigma_{ix}^2 \times \sigma_{iy}^2 = \int_{-\infty}^{+\infty}\mathrm{d}p_x\mathcal{S}_i(p_x)[1 - \delta(p_x)] \times \int_{-\infty}^{+\infty}\mathrm{d}p_y\mathcal{S}_i(p_y)[1 - \delta(p_y)]. \quad \text{(C2)}$$

With Eq. (11), the first integration on the right-hand side of Eq. (C2) is approximately

$$\sigma_{i_x}^2 \cong 2\mathcal{S}_i(p_0)\delta p_x$$

$$\cong 2\mathcal{S}_i(p_0)(2p_0 l_x w)^2 \operatorname{sinc}^2(wp_0)\frac{1}{l_x}, \quad \text{(C3)}$$

where the approximation $\operatorname{sinc}^2(l_x p_x) \cong \operatorname{rect}(l_x p_x)$ was made in Eq. (11) and $\delta p_x = 1/l_x$ is the integration bandwidth [see Fig. 4(c)]. When Eq. (C1) is introduced into Eq. (C3), one obtains

$$\sigma_{i_x}^2 \cong 2E^2(l_x)Nw^2 \operatorname{sinc}^2(w/\Lambda), \quad \text{(C4)}$$

where $p_m = 2p_0$, $p_0 = 1/\Lambda$, and $l_x = N\Lambda$ are used. The second integration on the right-hand side of Eq. (C2) can be estimated by

$$\sigma_{i_y}^2 \cong \mathcal{S}_i(0)[1 - \delta(p_y)]\delta p_y$$

$$\cong \frac{1}{2}E^2(l_y)l_y\Lambda, \quad \text{(C5)}$$

where the approximation $\operatorname{sinc}^2(l_y p_y) \cong \operatorname{rect}(l_y p_y)$ was made in Eq. (11), $\delta p_y = 1/l_y$ is the integration bandwidth, and $p_m = 2p_0 = 2/\Lambda$. Finally, introducing Eqs. (C4) and (C5) into Eq. (C2) leads to the result in Eq. (30).

ACKNOWLEDGMENT

This research was supported by the Commission pour la Technologie et l'Innovation.

REFERENCES

1. I. Yamaguchi and S. Komatsu, "Theory and applications of dynamic laser speckles due to in-plane object motion," Opt. Acta 24, 705–724 (1977).
2. T. Asakura and N. Takai, "Dynamic laser speckles and their application to velocity measurements of the diffuse object," Appl. Phys. 25, 179–194 (1981).
3. B. E. A. Saleh, "Speckle correlation measurement of the velocity of a small rotating rough surface," Appl. Opt. 14, 2344–2346 (1975).
4. J. Ohtsubo and T. Asakura, "Velocity measurement of a diffuse object by using time-varying speckles," Opt. Quantum Electron. 8, 523–529 (1976).
5. N. Takai, T. Iwai, and T. Asakura, "Real-time velocity measurement for a diffuse object using zero-crossing of laser speckle," J. Opt. Soc. Am. 70, 450–455 (1980).
6. M. Naito, M. Ishigami, and A. Kobayashi, "Spatial filter and its application to industrial measurement," presented at IMEKO-V, Versailles, May 25–30, 1970.
7. A. Kobayashi, "Measurement and sensors," Sens. Actuators 13, 29–41 (1988).
8. H. Ogiwara and H. Ukita, "A speckle pattern velocimeter using a periodical differential detector," Jpn. J. Appl. Phys. Suppl. 14, 307–310 (1975).
9. J. W. Goodman, "Statistical properties of laser speckle patterns," in *Laser Speckle and Related Phenomena*, 2nd ed., J. C. Dainty, ed. (Springer-Verlag, Berlin, 1984), pp. 9–75.
10. J. C. Dainty, "The statistics of speckle patterns," in *Progress in Optics*, E. Wolf, ed. (North-Holland, Amsterdam, 1977), Vol. XIV, pp. 1–46.
11. J. W. Goodman, *Statistical Optics* (Wiley, New York, 1985), pp. 60–79.
12. Hilbert transformation algorithm implemented in the MATLAB function *hilbert*, in *Signal Processing Toolbox for Use with* MATLAB (MathWorks, Natick, Mass., 1994).
13. F. de Coulon, "Théorie et traitement des signaux," *Traité d'Electricité* (Presses Polytechniques Romandes, Lausanne, 1984), Vol. VI, pp. 111–144.
14. J. W. Goodman, *Statistical Optics* (Wiley, New York, 1985), pp. 33–50.
15. S. O. Rice, "Mathematical analysis of random noise," Bell Syst. Tech. J. 24, 46–159 (1945).
16. A. W. Drake, *Fundamentals of Applied Probability Theory* (McGraw-Hill, New York, 1967), pp. 203–221.
17. A. Papoulis, *Probability, Random Variables, and Stochastic Processes* (McGraw-Hill, New York, 1991), pp. 86–102.
18. S. Lowenthal and H. Arsenault, "Image formation for coherent diffuse objects: statistical properties," J. Opt. Soc. Am. 60, 1478–1483 (1970).
19. R. Dändliker and F. M. Mottier, "Determination of coherence length from speckle contrast on a rough surface," J. Appl. Math. Phys. 22, 369–380 (1971).